MANCHESTER 1824
The University of Manchester

An investigation of the radio emission mechanism in strongly lensed radio quiet quasars

A thesis submitted to The University of Manchester for the degree of

Master of Physics and Astronomy

in the Faculty of Science and Engineering

YEAR OF SUBMISSION

2022

Thomas Dugdale

ID 10784808

Word count

∼15,000

THE SCHOOL OF NATURAL SCIENCES

Contents

List of Tables

List of Figures

Abstract

This thesis is part of an ongoing discussion as to the emission mechanisms of radio quiet quasars. Current models describe the possible emission mechanisms as either jetted or non-jetted (Padovani, 2017) but recent studies have indicated that there is room for a mixture of physical processes that drive the radio emission (Hartley et al., 2021). Gravitational lensing is a tool which allows us to study faint radio quiet quasars at resolutions that would otherwise be impossible allowing compact structure around quasar cores to be resolved using VLBI. This thesis contains the analysis of 12 strongly lensed radio quiet quasars with significant radio detections from the VLA interferometer where the detection rate was 12 sources of 22 detected with a detection limit of $\sim 10\mu$Jy ($\sim 2.5\sigma$). Of these sources; the radio emission of eight of them is likely to be dominated by star formation, one source is likely AGN dominated in the radio, and three sources are a possible mix of star formation and compact AGN activity. From the sample of 12, only three sources have FIR detections available therefore the other nine sources have FIR flux upper limits and thus upper limits on the Q_{IR} which determines if a galaxy is star forming or not. Two of the RQQs, SDSSJ0820+0812 and SDSSJ1128+2402, have radio spectral indexes of -1.020± 0.392 and -0.726 ± 0.200 respectively which is consistent with synchrotron radiation which is likely to originate in small scale AGN jets. One source, SDSSJ0941+0518, has a spectral index of -0.113 ± 0.158 which in indicative of thermal free-free emission (Bremsstrahlung radiation) which could be due to a thermally heated torus about the SMBH. SDSSJ0820+0812, SDSSJ0941+0518, and SDSSJ1128+2402 have inferred dominant radio emission mechanisms of star formation from the FIRC but their spectral indexes imply otherwise giving rise to a discrepancy between the RQQ emission mechanisms inferred from the radio spectral index and their position on the FIRC.

Lay Abstract

This thesis aims to join, and hopefully help, the ongoing investigation of what causes the radio emission in RQQs and whether the FIR correlation is a reliable tool for such an investigation or whether we need to use a collection of techniques. This thesis aims to help by using radio data from the VLA, and any available MIR/FIR data, to calculate radio and FIR luminosities as well as star formation rates and radio spectral indexes which together can be designated to different physical processes within a galaxy which helps to pinpoint the main producers of both FIR and radio radiation. Although this thesis presents a lot of data, some areas of astrophysics aren't discussed such as whether a RQQ has undergone a major or minor merger or whether corrections need to be made due to dust and gas and redshift, some of the data to investigate these phenomenon are however available within this thesis but lay outside the main aims of the project. Lensed RQQs were chosen as the sample for this thesis due to their faint radio signatures requiring a lens to detect and also the lack of analysis of the RQQs in this sample meaning many haven't been discussed in the depth that this thesis aims to present.

To begin the discussion of the RQQs in this sample, both radio and MIR/FIR (and more specifically **any** IR data available) was collected such that a modified black body radiation equation could be used to plot a model in Python for an accurate FIR flux density to be derived for the galaxies as well as spectral indexes and dust temperatures. Dust temperatures were important more to ensure the model fit was physically accurate for the IR radiation as temperatures lying outside a range of 20-100 Kelvin would indicate something wrong with the code or some new physics (no new physics was found), see Stacey et al. (2018) for a range of RQQ temperatures that were used to spot bugs in the code when the models would give non-physical temperatures. Spectral index was the other important parameter which was more relevant for the radio data where analysis could be done on both the QIR of a galaxy and its radio spectral index which would either; show agreement between the position on the FIRC (Far-infrared correlation) which would be what is expected, or a disagreement between the spectral index and position on the FIRC. Disagreements led the discussion of this thesis towards analysis done by Hartley et al. (2021) and raised some questions to the currently accepted models around RQQs in Chapter 5.

This thesis is organised such that the first three chapters offer introduction to the topic area where the first chapter discusses what is being observed with descriptions around the processes important to this thesis, although the specific processes for each RQQ cannot be fully investigated due to the lack of FIR data. The second chapter tries to explain how gravitational lensing works and how the action of a lens helps the study of faint RQQs for the purposes laid out previously in this introduction piece. The third introduction chapter is interferometry and is very complicated to fully understand so

best efforts have been made to both understand and explain this section as best as possible such that all aspects from observation to data reduction is understandable.

Chapter 4 offers the full process undergone to derive all data used in the results section with information about the data collected, the software used, the pipeline to CLEAN the data, and a section dedicated to how the logic of the model was carried through. This section is arguably the most important as a mistake in the code could yield false information making the entire results section wrong. The data and code was discussed with my collaborator, Dr Shruti Badole, giving great confidence that the process is accurate.

The data in this thesis and any missing discussion will be in a soon to be published paper that will contain the full sample from this thesis and collaborator resulting in the analysis of the largest collection of RQQs ever with the hope that the data and discussion will guide the, currently vague, origin of radio emission in RQQs and try to expand on the sometimes misleading FIRC.

Declaration

No portion of the work referred to in the thesis has been submitted in support of an application for another degree or qualification of this or any other university or other institute of learning. The work of the author in this thesis is part of a larger effort to investigate the radio emission mechanism of strongly lensed radio-quiet quasars. The author is responsible for analysis and interpretation of VLA observations.

Copyright

1. The author of this thesis (including any appendices and/or schedules to this thesis) owns certain copyright or related rights in it (the “Copyright”) and s/he has given The University of Manchester certain rights to use such Copyright, including for administrative purposes.

2. Copies of this thesis, either in full or in extracts and whether in hard or electronic copy, may be made only in accordance with the Copyright, Designs and Patents Act 1988 (as amended) and regulations issued under it or, where appropriate, in accordance with licensing agreements which the University has from time to time. This page must form part of any such copies made.

3. The ownership of certain Copyright, patents, designs, trademarks and other intellectual property (the “Intellectual Property”) and any reproductions of copyright works in the thesis, for example graphs and tables (“Reproductions”), which may be described in this thesis, may not be owned by the author and may be owned by third parties. Such Intellectual Property and Reproductions cannot and must not be made available for use without the prior written permission of the owner(s) of the relevant Intellectual Property and/or Reproductions.

4. Further information on the conditions under which disclosure, publication and commercialisation of this thesis, the Copyright and any Intellectual Property and/or Reproductions described in it may take place is available in the University IP Policy (see documents.manchester.ac.uk), in any relevant Thesis restriction declarations deposited in the University Library, The University Library’s regulations (see www.library.manchester.ac.uk/about/regulations/) and in The University’s policy on Presentation of Theses.

Acknowledgements

My supervisor, Dr Neal Jackson, has been the most amazing fountain of knowledge and support through this project and although I'm yet to meet him in person I'm glad that he has always been there when I needed him. Dr Shruti Badole, I would be so lost if we didn't talk virtually every day and you didn't help guide me through this project with the many discussions we had about the RQQ sample. I would also like to thank Dr Philippa Hartley for encouraging words throughout and early access to her 2021 RQQ paper. Anthony Holloway and Sotirios Sanidas have been an amazing help for anything IT/CASA/AIPS related and have continually kept wll packages up to date. Thank you to Nathan Steer for being the person I needed when code would break or LaTeX wouldn't format correctly. Much thanks goes out to all of JBCA for being such an sweet and friendly community.

1 Radio Quiet Quasars

1.1 Brief introduction to Quasars

Quasars, also known as quasi-stellar objects (QSOs), are the most optically luminous non-transient objects in the universe and appear as point-like objects within the centre of a host galaxy with optical luminosities thousands of times greater than ordinary galaxies (Kellermann, 2013; Yang et al., 2016). Approximately 90% of quasars are Radio Quiet whereas the other 10% are Radio Loud. It is still unknown whether RQQ and RLQ are two distinct modes of Quasar or whether they are identical modes (Kellermann et al., 2016). Quasars are variable objects (Lynden-Bell, 1969; Fan et al., 2009) that were first discovered in 1963 by Maarten Schmidt (Schmidt, 1963) though the nature of quasars was discussed in early 1960 by John Bolton (Kellermann, 2013). Quasars are inherently luminous due to the efficiency factor associated with the central engine known as supermassive black holes (SMBH) with mass $\sim 10^{6-10} M_{\odot}$ (Begelman et al., 2006; Bandara et al., 2009) with energy conversion a efficiency of 10% (Rees, 1978; Panessa et al., 2019). To separate quasars from bright Seyfert galaxies (Seyfert, 1935), we need a definition for absolute magnitude which is defined as $M_B \leq -23$ (Kellermann et al., 1989). Quasars typically have bolometric luminosities of $L_{bol} > 10^{45}$ergs^{-1} where the radio luminosity $L_{1.4\text{GHz}} < 10^{41}$ergs^{-}1 (Zakamska et al., 2015). Broad line emission is an early indicator of AGN activity due to the UV radiation from SMBH accretion ionising surrounding gas clouds which causes a velocity dispersion of several thousand kms^{-1} (Peterson, 1997; Heckman & Best, 2014). Figure 1.1 shows a model of broad line emission near the accretion disk and SMBH as evidence for quasars whilst the quasar AGN is in radiative-mode. Radio Loud Quasars are defined as having an "R-value" > 10 where R is the ratio of the radio flux density at 5GHz to the optical flux density at 440nm (Kellermann et al., 1989). This indicates an order of magnitude greater

flux density when observing in the Radio as compared to the optical. RQQ on the other hand have R-values < 10; see equation 1.1

$$R = \frac{S_{\nu,5\text{GHz}}}{S_{\nu,440\text{nm}}}, \tag{1.1}$$

where S_ν is the flux density. The flux density, S_ν, is a measure of energy per unit area per unit frequency; in the case of Janskies, Jy, this is W/m^2/Hz (Kalfountzou et al., 2012).

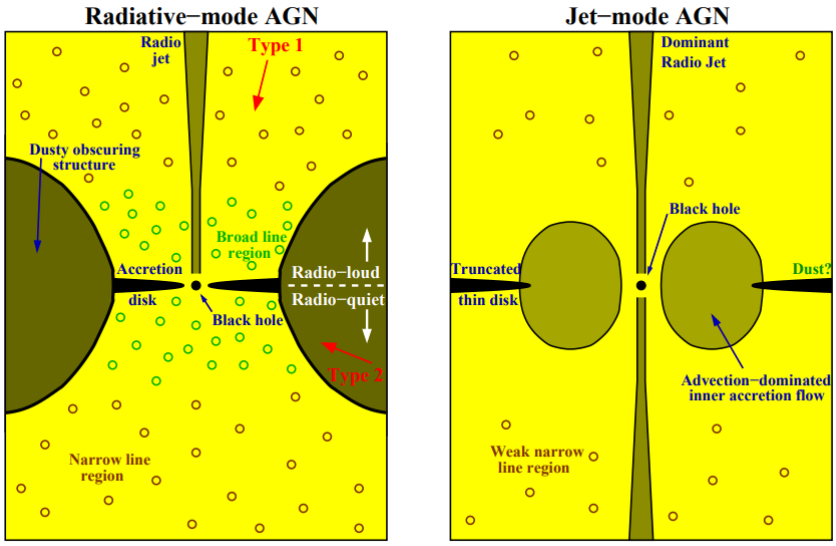

Figure 1.1: Model of both radiative and jet mode quasars with broad and narrow line emission corresponding to the gas velocity dispersion after being photo-ionised by the accretion disk UV radiation. (Heckman & Best, 2014).

QSOs can be used as probes into the early universe due to their high flux density providing observation of high redshift galaxies which allows us to study the AGN feedback mechanisms in galaxies from the early universe (Kellermann, 2013) which will be discussed in section 1.3. With the observation of younger galaxies we are able to build accurate models of AGN driven evolution in star formation rates to present day low redshift galaxies which allows us to have a more complete understanding of the process of galaxy formation and evolution from the early universe to present (Yang et al., 2016).

SMBHs are the heart of quasars and the source of copious amounts of synchrotron and optical radiation present in Radio Loud Quasars

(RLQ) from the accretion of material from surrounding gas such that the AGN outshines the host galaxy completely in the optical (Burbidge et al., 1963; Begelman, Blandford & Rees, Begelman et al.; Rees, 1984). The relativistic velocities obtained from angular rotation of the SMBH results in the particles of gas reaching energy equivalent to their rest mass producing optical/UV emission (Zakamska et al., 2015). RQQs on the other hand, although still bright in the optical, are theorised to be a separate type of quasar in a bimodal model whereby the radio emission can be due to the formation of stars initiated from an AGN causing feedback into the host galaxy or via gas rich galaxy mergers which introduce more gas and kinetic energy into a galaxy to start star formation. The investigation of quasars is therefore important for understanding the evolution and formation of galaxies.

AGN modes

Equations for the black hole accretion rates and energy can be found in Croton et al. (2006); Combes (2017) and are based on empirical models.

Quasar mode

Models of AGN evolution state the mass growth of SMBHs via major galaxy mergers is the dominant source of cold gas mass accretion and that the accretion regulates star formation via the quenching of gas. There are two possible ways AGN may quench star formation; black holes and stars gain mass from the same reserve of gas and so a SMBH effectively hoards the gas reserve (Heckman & Kauffmann, 2006). However, it could also be possible that this same mechanism may accelerate star formation by compressing gas from the feedback of the accretion disk (Silk, 2005). Another explanation for quenching could come from the AGN expelling gas from the host galaxy reserve (Fabian et al., 2006) therefore removing gas for both black hole growth and star formation (Di Matteo et al., 2005) backed up by observation evidence by Tremonti et al. (2007) using only 5% of the AGN power (Moe et al., 2009). This mode of AGN is called ”quasar mode” where the mass accretion rate is described by

$$\Delta m_{BH,Q} = \frac{f'_{BH} m_{cold}}{1 + (280 \text{kms}^{-1}/\text{V}_{\text{vir}})^2}, \tag{1.2}$$

where m_{cold} is the mass of the accreting cold gas, V_{vir} is the halo virial velocity, and $f'_{BH} m_{cold} = f_{BH}(m_{sat}/m_{central})$ is the fraction of massive dark objects (MDOs aka dark matter, m_{sat}) and the mass of the galaxy hot stellar galactic bulge ($m_{central}$) where the fraction is often taken as ~ 0.03 (Magorrian et al., 1998) where the gas flow, $\Delta m_{BH,Q}$, is most efficient in the scenario of a major merger (Croton et al., 2006).

Radio mode

The radio mode of a quasar describes low energy radio activity from the accretion of hot gas onto the SMBH (Nagamine et al., 2012; Li2, Li2) whereby the feedback infuses energy into the surrounding gas and dust to slow or stop the cooling flow. The cooling flow is described as the accretion of hot gas onto a cold gas disc whereby gravitational instability may lead to momentary star formation. Thus the feedback ensures that the gas has a longer time to cooling by contributing energy $L_{BH} = \eta \dot{m}_{BH} c^2$, where

$$\dot{m}_{\text{BH}} = k_{\text{AGN}} \left(\frac{m_{BH}}{10^8 M\odot} \right) \left(\frac{f_{hot}}{0.1} \right) \left(\frac{V_{vir}}{200 \text{kms}^{-1}} \right)^3, \tag{1.3}$$

whereby, $k_{AGN}(\text{M} \odot \text{yr}^{-1})$, is a constant to be found, f_{hot} is the fraction of hot gas mass in the halo (Croton et al., 2006).

1.2 Radio Quasar Properties

Only about 10% of all quasars are radio loud (RL) with the other 90 percent being radio quiet (Strittmatter et al., 1980; Kellermann et al., 1989; Miller et al., 1990) and as their name implies have little to no radio emission often 2-3 orders of magnitudes less radio emission than RLQ (Kellermann et al., 2016).

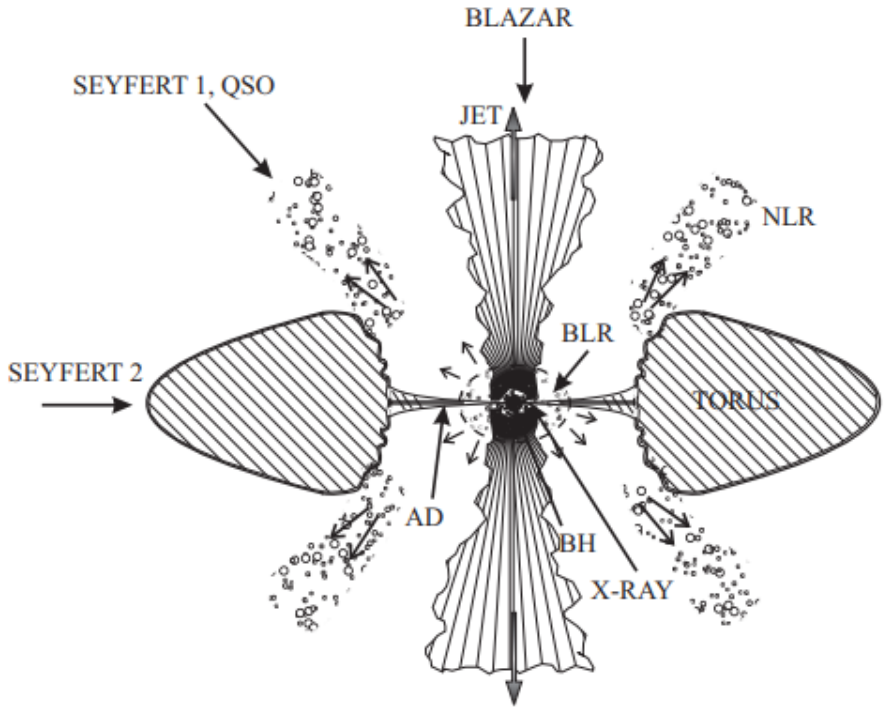

Figure 1.2: A unified model for AGN shows the type of AGN assigned is dependent on the observation angle when taking measurements (Jovanović & Popović, 2009).

The split of 90-10 can be explained by a bimodal model which was first proposed by Strittmatter et al. (1980). Kellermann et al. (1989) reaffirmed this bimodality by observing 114 objects with the VLA at 5GHz with the main finding being 92 of the quasars were found to be RQ. The fraction of the 114 Palomar Bright Quasar Survey (BQS) quasars found to be RQ is approximately 80% although this contradicts the earlier statement of a 90-10 split between RQQ and RLQ. The presence of RLQs at high redshifts has been demonstrated to decrease exponentially by Goldschmidt et al. (1999) and Jiang et al. (2007) who both record a lower population at high redshifts where the RQQ population begins to dominate.

The quasars in the study by Kellermann et al. (1989) have a median redshift of 0.2 which is rather low compared to more recent studies by Retana-Montenegro, E. & Röttgering, H. J. A. (2017). Lyke et al. (2020) have detected over 750,000 quasars from the Sloan Digital Sky Survey (SDSS) and found 480,459 quasars with redshifts in the range of $0.8 < z < 2.2$. Further evidence for the RLQ:RQQ population split is further supported by (Miller et al., 1990) who observed 105 quasars with

redshifts 1.8 < z < 2.5 and found strong evidence for a bimodal model for two distinct populations of quasars, that being RLQ and RQQ. Out of the 105 quasars, where 99 were new and 6 were RLQ from the previous work of (Smith & Wright, 1980), 9 were found to be RL (including the 6 from Smith and Wright) and 96 RQ which gives us approximately 8.5% RL and 91.5% RQ. Padovani (2017) argues we should refer to quasars as either jetted or unjetted rather than RL or RQ. However, a recent studies by Hartley et al. (2019, 2021) has proved this is not always the case with the identification of small scale jets producing synchrotron radio emission in RQQs.

The general luminosities of the two modes of quasars observed by Miller et al. (1990) was found to be $L_{5\text{GHz}} > 10^{25}\text{WHz}^{-1}\text{sr}^{-1}$ for RLQ, $L_{5\text{GHz}} < 10^{24}\text{WHz}^{-1}\text{sr}^{-1}$ for RQQ, and no quasars in the sample were found to have intermediate radio flux density. This follow up study by Miller et al. (1990) operated at greater sensitivity than Smith & Wright (1980) with an RMS (root mean square) noise of 0.2mJy/beam as compared to Smith and Wright's 2.5mJy/beam which allowed for the detection of 96 RQQ. However, debates arose that RLQ and RQQ, from studies by (Blundell & Beasley, 1998; Leipski et al., 2006), have shown that intermediate flux density quasars can exist, which unlike what Miller et al. (1990) reinforced, suggests that quasars do not exist as bimodally discrete.

The optical line emission within quasars is produced by broad,$\sim 10,000\text{kms}^{-1}$, and narrow, <1000kms^{-1} (Peterson, 1997; Heckman & Best, 2014) line regions near the centre of the AGN, this is caused by the ultraviolet (UV) and X-ray radiation from the accretion disk exciting the surrounding gas clouds thus producing optical wavelengths of light (Antonucci, 1993).

As shown in Figure 1.2 unified models have been used to theorise that all AGN types located in the central regions of a galaxy are the same. The only dependency that varies the type of AGN we observe is the

angle of orientation between the accretion disc producing jets and the line of sight of observation which changes how we observe the central regions of the AGN thus leading us to classify the same AGNs differently (Jovanović & Popović, 2009). For example, we would observe a blazar if the jets are angled towards the observer or if the AGN jets have an angled offset towards the observer, we would observe a Seyfert 1. The first evidence for this unified model came from Antonucci & Miller (1985) in which highly polarised broadened FeII Balmer lines in NGC 1068 displayed properties similar to that of Seyfert 1 galaxies despite NGC 1068 first appearing as a Seyfert 2 galaxy. The broad line emission observed in NGC 1068 was found to be hidden behind a geometrically and optically thick disk which is brought into an observing line of sight due to free electrons scattering the radiation above and below the disk which provides a line of sight that would otherwise not be possible from Earth. The scattering of broad emission lines in NGC 1068 gives us a second point of view of the AGN providing strong evidence towards the unified model of AGNs.

1.3 Radio Emission Mechanisms in RQQs

There are many possible mechanisms that can produce radio emission, for example star formation or accretion around a central SMBH (Panessa et al., 2019; Laor & Behar, 2008).

1.3.1 Radio emission by star formation

It is found that at $z \sim 1.5$ and ν=1.4GHz most submillijansky radio emission from star formation is seen as extended structure in the RQQ host galaxy rather than the AGN although this does not always indicate the absence of the role of the AGN in driving this star formation (Di Matteo et al., 2005; Fabian et al., 2006; Heckman & Kauffmann, 2006; Panessa et al., 2019). The radio from star formation comes from the relativistic acceleration of electrons from the strong magnetic field during

star formation (McKee & Ostriker, 2007).

AGN outflow induced star formation

We assume AGNs provide an outflowing wind determined by a luminosity L_{AGN} produced by the accretion disk around the SMBH (Wandel, 1999). The AGN outflow wind can excite the ISM depending on both the kinetic energy of the wind and the density of the gas. The shock reaches a reverse shock radius from the AGN indicated by R_{SW} after travelling through the medium before being separated into its two components. The first component of the wind is a kinetic energy that drives the shock through the ISM before the wind separates at a discontinuity radius R_c into the shocked ambient medium (SAM). The SAM region is determined to exist between radii $R_c < SAM < R_s$ where the shock will radiate through synchrotron, inverse compton and free-free radiation (Nims et al., 2015).

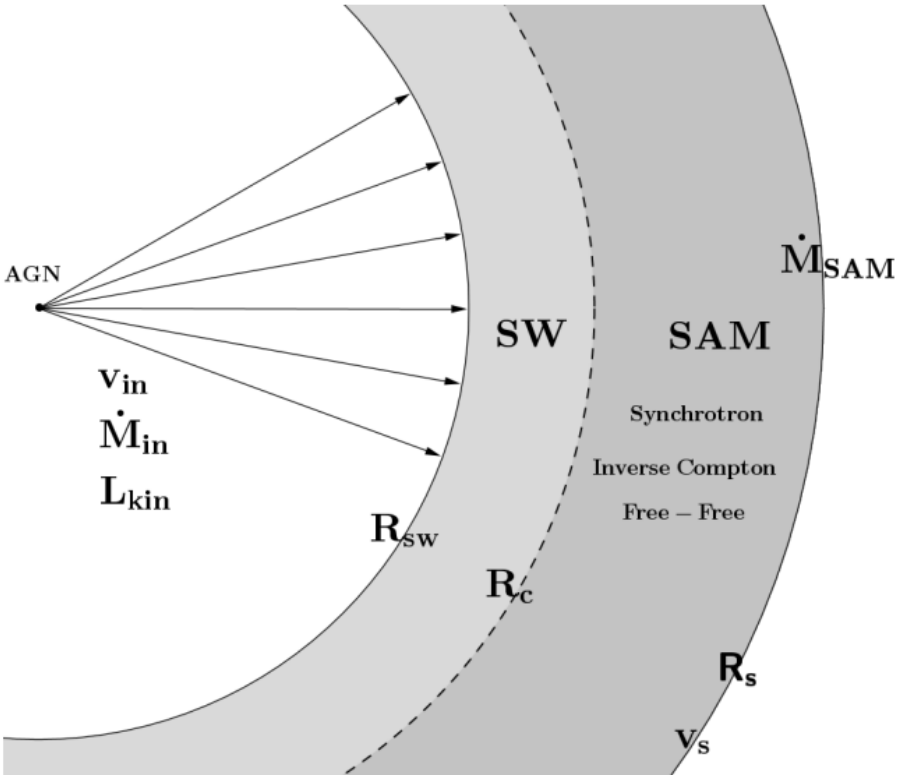

Figure 1.3: Resultant regions as a result of the AGN outflow winds where an outer SAM ring is responsible for radio emission due to the compression. Figure 1 from (Nims et al., 2015)

AGN wind with $L_{\text{AGN}} \sim 10^{46}\text{ergs}^{-1}$ generally corresponds to a star formation rate of $\sim 300\text{M}_{\odot}\text{yr}^{-1}$ due to the compression of gas in the

ISM from the outflow wind transferring energy causing wind velocity deceleration to $v \sim 1000$kms^{-}1. Star formation is driven by this outflow compression of gas which, when forming into a proto-star, relativistically accelerates electrons via strong magnetic fields to produce synchrotron radiation where star formation is indicated by an x-ray luminosity of $L_X \sim 10^{42}$ergs^{-1} (Nims et al., 2015).

Galaxy Merger induced star formation

Simulations by Springel et al. (2005); Hopkins et al. (2008); Somerville et al. (2008) have shown that gas-rich galaxy mergers can induce the main phase of AGN with starburst activity. Mergers with mass ratios $>> 3:1$ will not produce significant starburst or AGN activity thus the most eventful mergers are those where the mass ratios are $\sim 1:1$ where we expect significant star formation and AGN activity. The star formation rate density is described by

$$\dot{\Sigma}_{\text{SFR}} = A_{\text{kenn}} \Sigma_{\text{gas}}^{N_{\text{k}},} \quad (1.4)$$

where, $A_{\text{kenn}} = 1.67 \times 10^{-4}$, is the normalisation constant and is unitless, $N_K = 1.4$, Σ_{gas} is cold gas surface density in the disk M$_\odot$pc^{-2}, and Σ_{SFR} has units M$_\odot$yr^{-1}kpc^{-2} (Somerville et al., 2008). As described, star formation rate density will be at a maximum during minor galaxy mergers where black hole accretion will also see no change or a decrease in mass accretion therefore providing more non-accreting cold gas for further star formation (Armitage & Natarajan, 2002).

1.3.2 Compact core radio emission

RQQ are strongly accreting about their SMBHs but lack a jet feature that extends upwards of 100kpc into the ISM (Intersteller medium) (Greenstein & Schmidt, 1964). The cores of RQQ and radio intermediate

quasars (RIQ) have been imaged many times with the introduction of VLBI (Very Long Baseline Interferometry) allowing structures on mas (milli-arcsecond) scales to be revealed, see Figure 1.4 (Blundell & Beasley, 1998; Ulvestad et al., 2005). Gallimore et al. (2004) observed NGC 1068 using the VLBA (Very Long Baseline Array (Kellermann & Thompson, 1988)) at sub-arcsecond resolutions and measured temperatures 10^5K which was concluded to not be sufficient for synchrotron self absorption unless magnetic fields exceeding 10^9G are present to bring the brightness temperature to a comparable level of the synchrotron electron kinetic temperature (Gallimore et al., 1996). Instead, in the case of NGC 1068, Gallimore et al. (1996) suggests thermal radio emission based on emissivity index measurements of $\nu^{0.3}$ as the simplest explanation with the least parameters involved (number of electrons, n_e, temperature of electrons, T_e, and source size), an ideal brightness temperature less than or comparable to that which would be expected from X-ray excited gas from a central engine, and the regions of emission S_1 and S_2 are of an expected size with estimated parameters to produce flux density via free-free emission. For compact core emission, Blundell & Kuncic (2007) later proposed a thermal source of radio emission under the assumption that the emitting region is optically thin and is sufficiently hot. At temperatures of $T \sim 10^7$K gas is fully ionised and so if the gas is dense and sub-relativistic then free-free emission dominates Compton emission (Blundell & Kuncic, 2007).

Free-free emission cannot dominate unless temperatures exceeds $\approx 10^7 K$ which is not possible in optical thick regions due to gas temperature limiting the maximum possible temperature. The temperature of an optically thin thermal source is defined as

$$T_b \approx c^2 j_\nu R/(2k\nu^2), \tag{1.5}$$

where T_b is the brightness temperature, j_ν is volume emissivity at frequency ν, R is the size of the thermal source, c and k are the speed of

light and Boltzmann constant (Blundell & Kuncic, 2007). This process of accretion therefore gives us small scale radio structure about the SMBH with radii in the vicinity of a couple parsecs caused by jets similar to those in RLQ although 2-3 orders of magnitudes weaker (Laor & Behar, 2008; Blundell & Beasley, 1998).

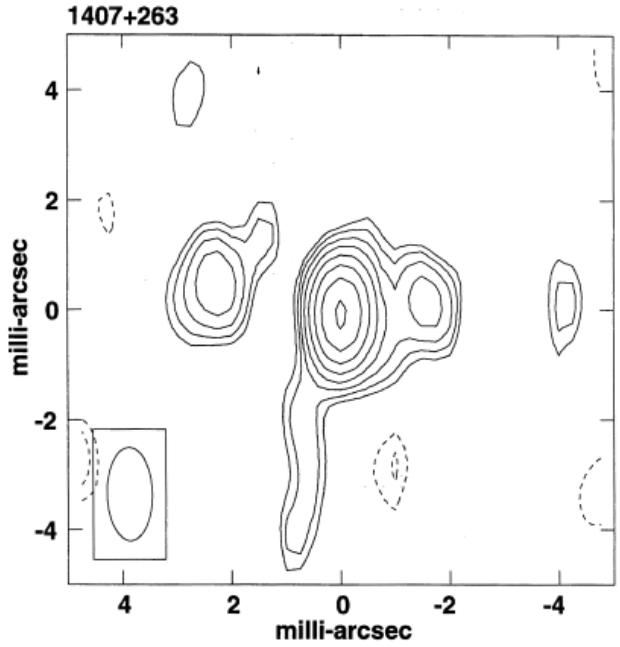

Figure 1.4: mas observation of RQQ J1407+263 with flux density of 0.20mJy/beam at 8.4GHz shows clear evidence of thermal free-free structure. Figure from (Blundell & Beasley, 1998)

Non-thermal Synchrotron radiation can also be present near the SMBH where electrons are relativistically accelerated producing radiation in a cone with a half angle $\phi \sim E/mc^2$ where each electron radiates energy according to

$$\frac{\mathrm{d}E}{\mathrm{d}t} = 6.08 \times 10^{-9} B^2 E_{GeV}^2 ergs/sec, \tag{1.6}$$

where B is the magnetic field and E_{GeV} is the energy of each electron (Kellermann & Owen, 1988).

1.3.3 Exotic forms of radio emission

Star formation is often observed to extend over the full scale of the host galaxy with clear indicators of thermal and non-thermal low-frequency radio emission due to the presence of strong magnetic fields and supernova remnants (Laor & Behar, 2008). Radio emission can however originate from coronally active stars where a ratio of X-ray and Radio flux density is stated to be $L_R/L_X \simeq 10^{-5}$ which is known as the Gudel-Benz relation (Guedel & Benz, 1993; Laor & Behar, 2008). Synchrotron radiation in this scenario is induced by electrons accelerating to relativistic velocities in magnetic field reconstructions which is then followed by a typical X-ray flare. This was first observed in our own Sun by Neupert (1968) who found that solar radio flares are followed by rising X-ray activity before resulting in an X-ray flare. Figure 1.5 shows the radio emission for both RQQ and RLQ as a function of x-ray emission which shows that RLQ have a radio luminosity ∼1,000 times larger than RQQ most obviously due to the fact that RLQ are not star formation dominated and are instead driven by AGN activity.

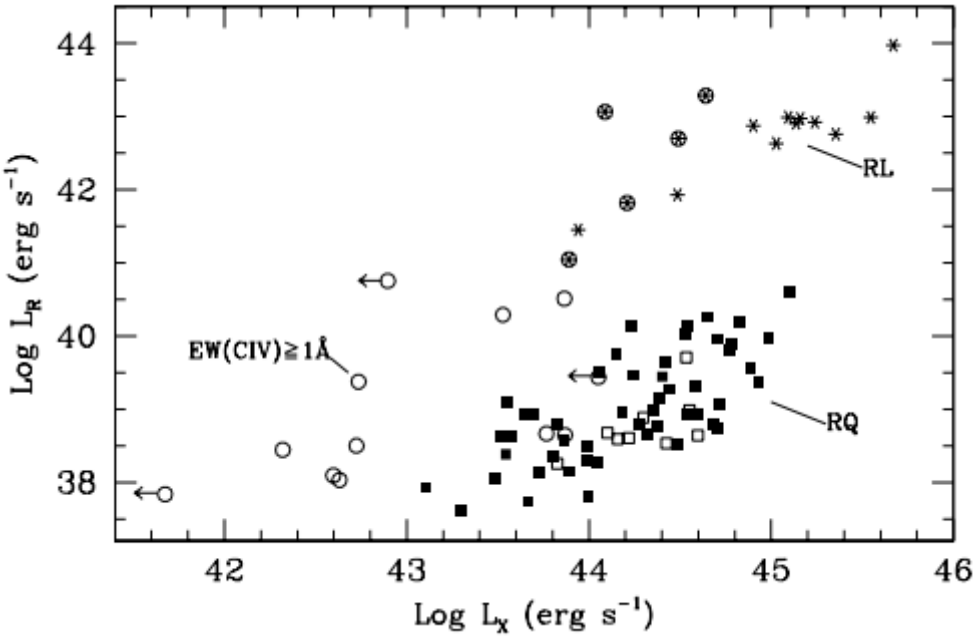

Figure 1.5: A distribution that shows RLQs have similar X-ray radiation emission but have radio emission in excess at $\sim 10^3$ times larger than RQQs (Laor & Behar, 2008).

2 Gravitational Lensing

Gravitational lensing (GL) arises from the deflection of light of a background object by a massive foreground galaxy or cluster of galaxies which magnify sources by a general factor of 10-20 (Atek et al., 2015; Yuan et al., 2012). Gravitational lensing allows us to observe faint background objects as well as the mass distribution and by extension mass content of the foreground lens (Schneider et al., 1992). From the theory of general relativity (GR) it was hypothesised that two different scenarios could occur, the first would be an Einstein ring, first anticipated by Chwolson (1924), where a massive foreground object lay directly in front of the background source though this is virtually impossible as a lens will always have uneven mass distributions and the background object will always have a minor offset. The second scenario would be when the background source is offset hence producing multiple images (Zwicky, 1937; Refsdal, 1964)

2.1 Strong Gravitational lensing

GR describes how mass distorts space-time around it (Einstein, 1919). GR revolutionised the understanding of how mass interacted with space-time in ways that classical physics could not explain such as the realisation of space-time as a 4-dimensional manifold that all particles must geometrically conform to (Zhao & Blair, 2017) and hence gives correct predictions for light deflections based on mass distributions which is the core mechanism of GL. As a result of strong gravitational lensing (SGL) background sources are multiply imaged giving us tangentially distorted imaged of the background source. With knowledge of SGL and GR we are able to create models of the gravitational lens with knowledge of the mass and mass distribution hence allowing the multiple images to be reconstructed into an image of the background galaxy with lensing effects removed. However, in practice the lens mass distribution must

be reconstructed where there we also create a zero lens mass model to see just the lensed image (Chen et al., 2015; Jackson, 2015; Badole et al., 2020).

2.2 0957+561

The first gravitationally lensed quasar, Q0957+561, was discovered in 1979 by Walsh et al. (1979). The lensing galaxy has redshift $z = 0.39$ and was discovered in the Palomar Observatory Sky Survey (POSS) (Young et al., 1980). The lensed QSO 0957+561 is double image lens with images A and B having near identical spectra separated by approximately 6 arcseconds with magnitude 17 brightness in V band and redshift z=1.405. In a followup study by (Rhee, 1991) the velocity dispersion of the lensing galaxy was measured as well as the time delay variations between the two images which was used to estimate the Hubble constant to about 50kms^{-1}Mpc^{-1} using equation 2.1.The velocity dispersion was measured to be approximately 303kms^{-1} using a cross-correlation technique (Tonry & Davis, 1979) with the star HD207229. The time delays between image A and B are 415 $\pm$ 20 days (Roberts et al., 1991) and 404 $\pm$ 10 days (Schild & Thomson, 1997) respectively giving an average of about 410 days. Both studies also suggest possible microlensing which applies a quasi-random variation to the individual light curves making measurement of the delays more difficult.

$$H_0 = (90 \pm 10)\left(\sigma_\nu/390\text{kms}^{-1}\right)^2 \left(\Delta_{\tau_{BA}}/1\text{yr}\right)^{-1} \text{kms}^{-1}\text{Mpc}^{-1} \qquad (2.1)$$

.

Equation 2.1 is a rough estimation for the Hubble constant, H_0, which has units MPc^{-1}kms^{-1} where σ_ν is the velocity dispersion and $\Delta_{\tau_{BA}}$ is the time delay between images B and A where a positive $\Delta_{\tau_{BA}}$ indicates image A varies first.

Jones et al. (1993) found a new component of 0957+561 in the xray which appeared as an arc with approximate outer diameter of 3 arcseconds, see figure 2.1.

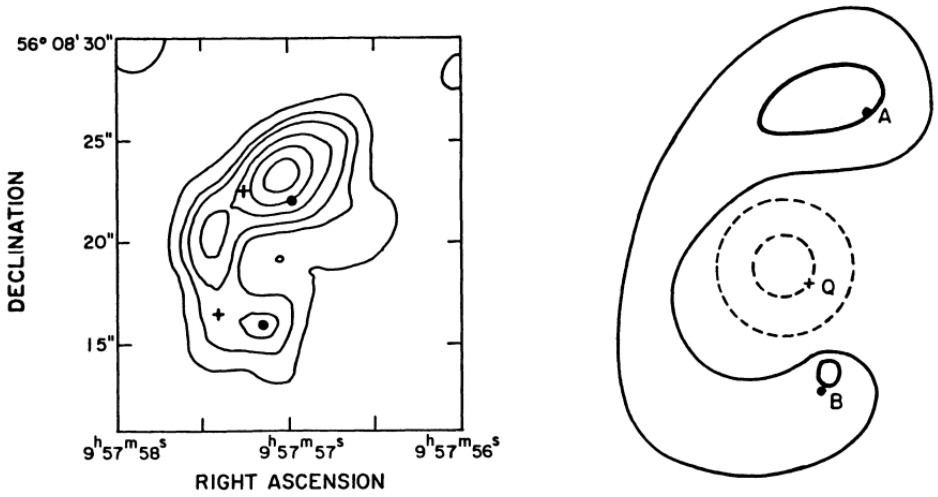

Figure 2.1: Left image shows the smoothed deconvolution of xray emission with the solid black dots being images A and B with an arc like structure connecting the two. The right image shows a model of the xray arc with image A and B located at the top and bottom of the arc respectively.

Explanations for the X-ray component in 0957+561 ranged from bright X-ray knots in the radio jets and different types of cooling from Compton heating, Thomson scattering and photo-ionisation. It was concluded however that the most likely source for the emission was from a cluster cooling flow assuming 0957 lay within a group or cluster of galaxies (Jones et al., 1993).

2.3 History of Lensing

This section highlights how initial thoughts of light deflection from Newton and Soldner led to modern lensing from Einstein, Alsing, and Werner.

2.3.1 Initial ideas and derivation for lensing

The deflection of light was hypothesised as far back as Newton (1704) and was later derived by Soldner (Jaki, 1978) though his calculation of the deflection angle was a factor of 2 lower than the correct equation (Sauer, 2021) which the theory of general relativity (GR) correctly accounts for. Equation 2.3 is a factor of 2 smaller than that derived by Alsing (1998); Werner (2012) who both used GR which gives us equation 2.6.

Soldner derived early calculations for light ray deflections from a horizontal path to a lensing star at closest approach thus leading to a maximum deflection angle (Jaki, 1978), see figure 2.2.

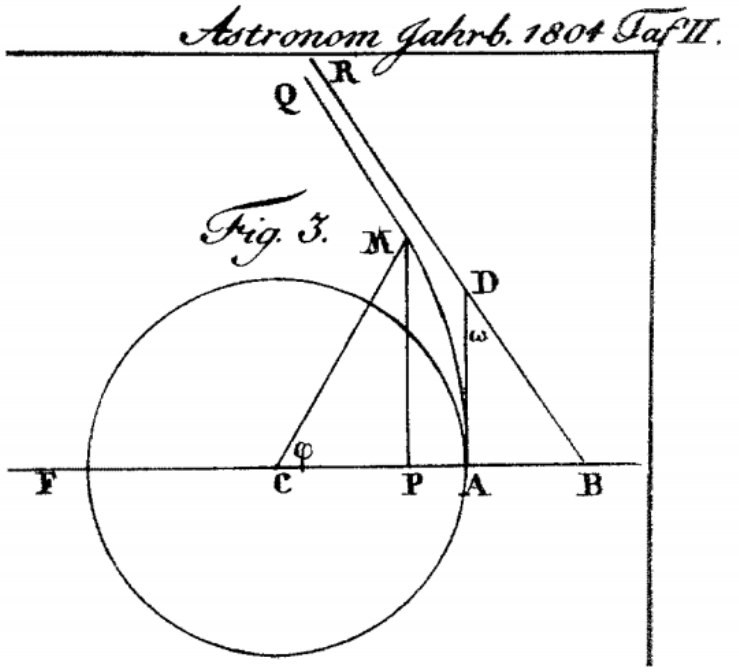

Figure 2.2: Sphere of radius CA with a light ray travelling along AD if not gravitationally influenced, instead the light ray travels along AMQ due to the gravitational influence of the sphere (Jaki, 1978)

Soldner described the path a light ray would travel as

$$y^2 = px + \frac{p}{2a}x^2, \tag{2.2}$$

which is the general equation for all conic sections where p is the parameter and a is the half main axis if measured from the abscissa.

When x is 0; the path is described as a parabola; if equation 2.2 is positive, the path is a hyperbola; if negative, the path is an ellipse. See Jaki (1978) for a full breakdown of the derivation and calculation of the parameter p.

Soldner expressed the deflection angle as

$$\tan\omega = \frac{KM}{\Delta^2\nu^2}\frac{1}{\sqrt{1-\frac{2KM}{\Delta^2\nu^2}}}, \tag{2.3}$$

where K is the gravitational constant, M is the gravitating mass, and Δ is the unit length from the gravitating body in units of radii often taken to be $\Delta = 1$ (Jaki, 1978; Sauer, 2021).

2.3.2 Einstein lensing

In 1936, Einstein published a column article at the request of R.W.Mandl describing the gravitational deflection of light from background star A caused by the gravity of foreground star B (Einstein, 1936). Einstein explained how if within a few light seconds on the vector $\vec{AB}$, we will not observe a point-like object but will instead observe a luminous circle with angular radius

$$\beta = \sqrt{a_0\frac{R_0}{D}}, \tag{2.4}$$

where β is the angular separation of images, a_0 is the deviation angle of the light from star A passing star B, R_0 is the distance of the light ray from the centre of the star B, and D is the distance of the observer from the star B, see figure 2.3. Einstein then described how a small distance x away from the vector $\vec{AB}$ in arcseconds, two point like objects in the form of two lensed images are observed where images have a magnified brightness represented by

$$q = \frac{l}{x} \cdot \frac{1 + \frac{x^2}{2l^2}}{\sqrt{1 + \frac{x^2}{4l^2}}}, \tag{2.5}$$

where q is the ratio of the apparent and intrinsic image brightness of the star A, and $l = \sqrt{a_0 D R_0}$ in light seconds. A ring will only manifest when the distance x is much smaller than l which in itself is only a few light seconds in size.

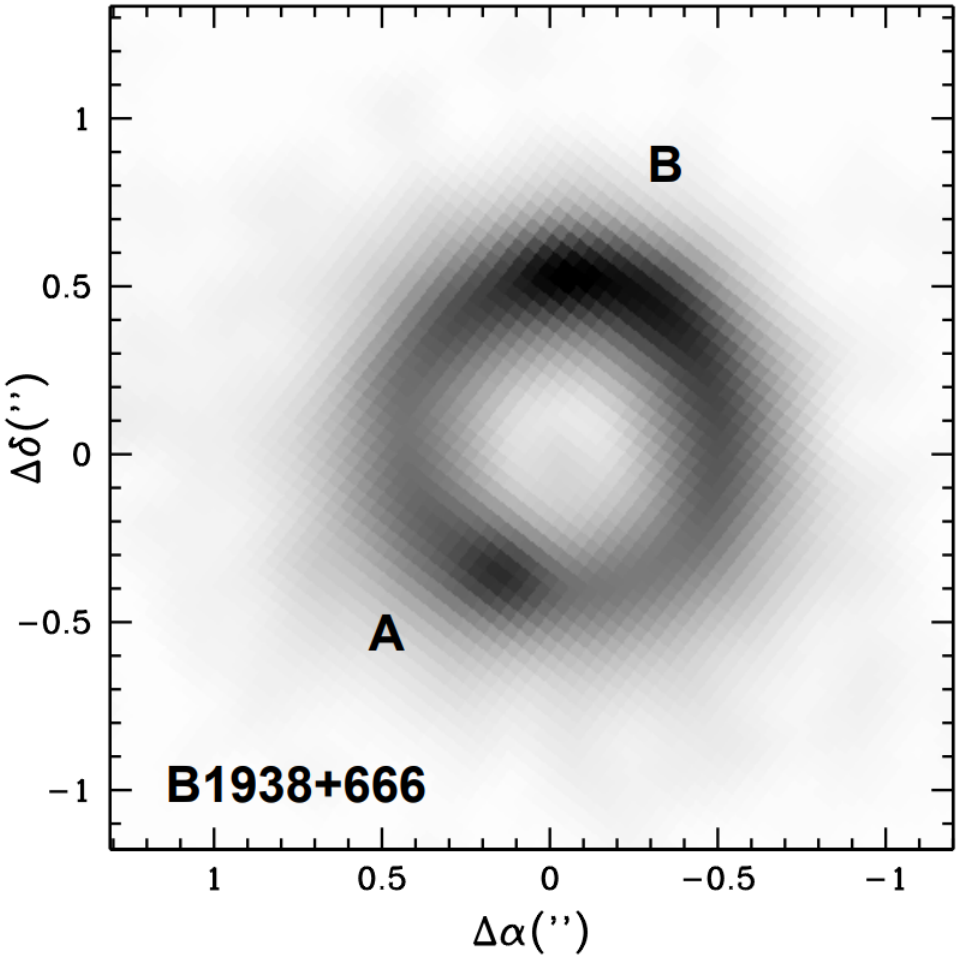

Figure 2.3: Einstein ring of quasar B1938+666 with the lensing galaxy completely removed from the image. Approximate diameter of the ring is 1 arcsecond which is composed of two lensed images due to the lensing galaxy lying almost directly in line of sight of the quasar source (Kochanek et al., 2001).

2.4 Modern lensing

The purpose of this subsection is to derive lensing equations and to explain what they mean before moving onto practical uses of

gravitational lensing with detail about benefits for high redshift observations. This subsection is based on Schneider et al. (1992); Wambsganss (1998); Kochanek (2004).

2.4.1 The Schwarzschild Lens

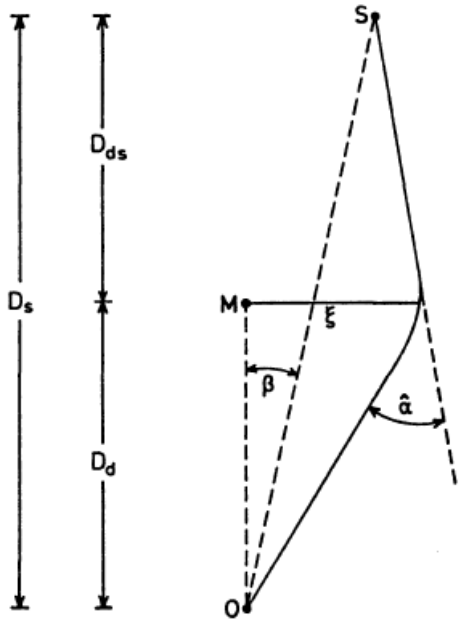

Figure 2.4: D_d is the distance to the lens, D_s is the distance to the background source, D_{ds} is the distance of the background source to the lens. At a distance of D_s from the observer, O, has angular separation of β, a ray of light from source S at a distance of ζ will be deflected by angle α. The observer sees an an image of the source at theta = ζ/D_d, figure from Schneider et al. (1992)

The correct lensing bend angle, $\alpha(\theta)$, is

$$\alpha(\theta) = \frac{4GM(<\xi)}{c^2\xi}\frac{D_{ds}}{D_s}, \tag{2.6}$$

as noted in (Kochanek, 2004) and derived by (Alsing, 1998; Werner, 2012)) where G is the gravitational constant, M is the mass of the lens, ξ is the impact parameter of the lens, c is the speed of light, D_{ds} is the distance of the source to the lens, and D_s is the distance to the source.

The condition for a light ray, from a background source, to reach the observer is

$$\beta D_s = \frac{D_s}{D_d}\xi - \frac{2R_s}{\xi}D_{ds}, \tag{2.7}$$

where R_s is the Schwarzschild radius, ξ is the impact parameter, and β is the angular separation of images.

We can switch to using angular diameter distance

$$D_A = \frac{D_M}{1+z}, \tag{2.8}$$

which is the ratio of an object's transverse size to its angular size (in radians) where D_M is the comoving distance or proper distance (Weedman, 1986). The angular diameter distance is preferred for translating telescope image angular separations into proper angular separations at the observed source (Peebles, 1993; Hogg, 1999).

We can define θ as the angular position of an image from the lens which is taken as the small angle approximation where $\tan(\theta) \sim \theta$

$$\theta = \xi / D_d, \tag{2.9}$$

and inserting into equation 2.7 we get the lens equation

$$\beta = \theta - 2R_s \frac{D_{ds}}{D_d D_s}\frac{1}{\theta}. \tag{2.10}$$

We can then simplify this equation by defining a characteristic angle α_0 and also a characteristic length ξ_0 (also called the proper distance to the lens (Kochanek, 2004))

$$\alpha_0 = \sqrt{2R_s \frac{D_{ds}}{D_d D_s}}, \tag{2.11}$$

and

$$\xi_0 = \sqrt{2R_s \frac{D_d D_{ds}}{D_s}} = \alpha_0 D_d, \tag{2.12}$$

and inserting Equation 2.11 and Equation 2.12 into Equation 2.10 we get

$$\beta = \theta - \frac{\alpha_0^2}{\theta}. \tag{2.13}$$

Multiplying Equation 2.13 by θ and rearranging we get

$$\theta^2 - \beta\theta - \alpha_0^2 = 0. \tag{2.14}$$

Applying the quadratic formula we can get solutions for θ which defines the angular position of the images from the lens

$$\theta_{1,2} = \frac{1}{2}\left(\beta \pm \sqrt{\beta^2 + 4a_0^2}\right). \tag{2.15}$$

From equation 2.15 we can calculate the difference between θ_1 and θ_2 which is the angular separation of the two lensed images,

$$\Delta\theta = |\theta_1 - \theta_2| = \sqrt{\beta^2 + 4\alpha_0^2} \geq 2\alpha_0. \tag{2.16}$$

The lens equation 2.10 can be further simplified with the knowledge that equation 2.6 is simply twice the Schwarzschild radius, divided by the impact parameter ξ (see equation 2.9), then scaled by a distance ratio $\frac{D_{ds}}{d_s}$,

$$\alpha(\theta) = \frac{4GM(<\xi)}{c^2\xi}\frac{D_{ds}}{D_s} = 2R_s\frac{D_{ds}}{D_d D_s}\frac{1}{\theta}. \tag{2.17}$$

Hence we can substitute equation 2.17 into equation 2.10 to get

$$\beta = \theta - \alpha(\theta), \tag{2.18}$$

where

$$\alpha(\theta) = \theta \left\langle \kappa(\theta) \right\rangle . \tag{2.19}$$

$\kappa(\theta)$ is the convergence in units of critical surface density

$$\kappa(\theta) = \frac{\Sigma(\theta)}{\Sigma_{cr}}, \tag{2.20}$$

where

$$\Sigma_{cr} = \frac{c^2}{4\pi G} \frac{D_s}{D_d D_{ds}}. \tag{2.21}$$

Images only have comparable brightness if β, and therefore $|\theta|$, are approximately a_0 meaning we usually see angular separations very close to the minimum value of $2a_0$ with impact parameter ξ_0 in all observations of lensed images. This also means that so long as a spherically symmetric mass distribution is within bounds of $\xi/3$, we can treat it as a point mass because the Schwarzschild metric always describes the exterior of a spherically symmetric mass distribution (Schneider et al., 1992).

2.5 Magnification

Magnification is how we describe the apparent increase of flux density of an image however the surface brightness of a lensed image is conserved (Barkana & Loeb, 2000). The flux density magnification of a source under the effect of gravitational lensing is described by

$$\mu = \frac{1}{\det \mathcal{A}}, \tag{2.22}$$

where μ is the magnification factor and $\mathcal{A}$ is the Jacobian matrix

$$\mathcal{A} = \begin{pmatrix} 1-\kappa-\gamma_1 & -\gamma_2 \\ -\gamma_2 & 1-\kappa+\gamma_1 \end{pmatrix} = (1-\kappa)\begin{pmatrix} 1 & 0 \\ 0 & 1 \end{pmatrix} - \gamma \begin{pmatrix} \cos 2\varphi & \sin 2\varphi \\ \sin 2\varphi & -\cos 2\varphi \end{pmatrix}, \tag{2.23}$$

where φ is the reflecting angle of shear relative to the coordinate system, shear is $\gamma = \sqrt{\gamma_1^2 + \gamma_2^2}$, and κ is the convergence.

Shear γ is the angular perturbation of a lensed image with γ_1 and γ_2 being the real and complex component respectively (Narayan & Bartelmann, 1996). Shear is the result of galaxy structure and surrounding clusters of gas exerting a gravitational effect on the light path resulting in the external (or tidal) shear of images. Shear is derived from taking the second partial derivative of the potential ψ such that

$$\gamma_1 = \frac{1}{2}(\psi_1^1 - \psi_2^2), \gamma_2 = \psi_2^1 = \psi_1^2, \tag{2.24}$$

where ψ_i^j is the gravitational potential (Bartelmann, 2010).

We can then rewrite equation 2.22 as

$$\mu = \frac{1}{\det \mathcal{A}} = \frac{1}{(1-\kappa)^2 - \gamma^2}, \tag{2.25}$$

where κ is the convergence as defined in equation 2.19. Observational lines of sight where $\det \mathcal{A} = 0$ indicates infinite magnification, this is achieved when an image lies directly on the critical curve of the lens.

For magnification, we have three possible stationary solutions for types of non-critical images that lie on an arrival-time surface as defined

by the Fermat potential $\phi(x, y)$ (Frittelli et al., 2002).

$$\begin{pmatrix} Minima, \det \mathcal{A} > 0 \\ Saddlepoint, \det \mathcal{A} < 0 \\ Maxima, \det \mathcal{A} > 0 \end{pmatrix} \begin{cases} \text{if } \gamma < 1 - \kappa \leq 1, \mu \geq 1 \\ \text{if } (1-\kappa)^2 < \gamma^2 \\ \text{if } (1-\kappa)^2 > \gamma^2 \end{cases} \tag{2.26}$$

The parity of images is; positive at minima, negative at saddle points, positive at maxima. The parity of images tells us whether they are inverted or not when compared to the source. For example, if we have a positive and negative parity image, then both will be identical but the negative parity image will be inverted.

2.5.1 Caustics and critical lines

Caustics and critical lines are points within a lens that determine both the number of images and magnification of a background source.

A single background source (which we will define as 1 image assuming little to no lens gravitational effect) will appear either as 1, 3, or 5 images depending on the position inside the caustic curves. Caustics regions separate the number of images produced in the image plane; a source existing inside the tangential caustic will produce 5 images, between the tangential and radial caustic will produce 3 images, and outside the radial caustic will produce a single image. The critical curves in the image plane are the points at which two extra images merge together before slowly disappearing the further the source moves from the critical line. Therefore, a source passing through the tangential and then radial caustic will reduce from 5 to 3 images and have 2 merge at the tangential critical line into a highly magnified and bright image before disappearing, then when passing through the radial caustic will have the final two images merge again before a single background source image is left (Narayan &

Wallington, 1992), see figure 2.5.

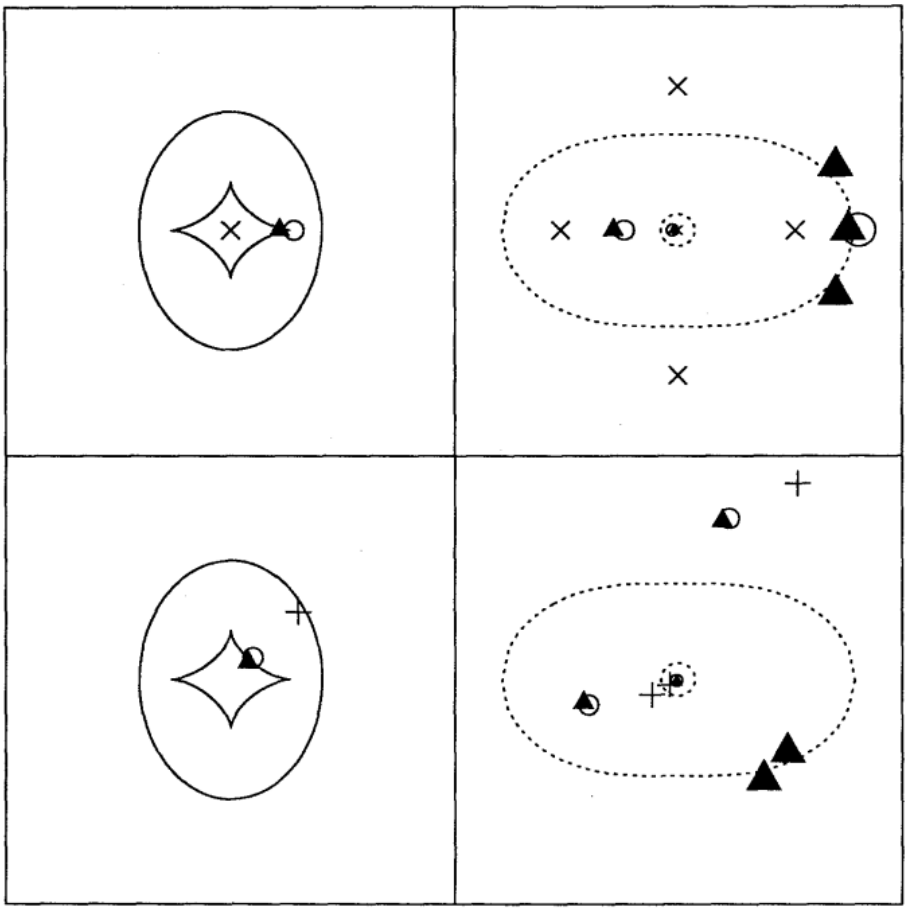

Figure 2.5: The left images show the caustics of the source plane where the inner 4 cusp solid line is the tangential caustic and the outer single cusp solid line is the radial caustic. The right images show the critical lines in the image plane where the inner dotted line is the radial critical line and the outer dotted line is the tangential critical line. Fig 2 Narayan & Wallington (1992)

The importance of caustics and critical lines is shown in figure 2.6. For maximum magnification and thus the greatest possible flux density from a background source we would want to have an observation such as in figure 2.6C. However, if we are more interested in the dark matter content of a foreground lensing galaxy, then we would want a configuration similar to figure 2.6A/B which offers multiple images and thus multiple lines of sight through a galaxy.

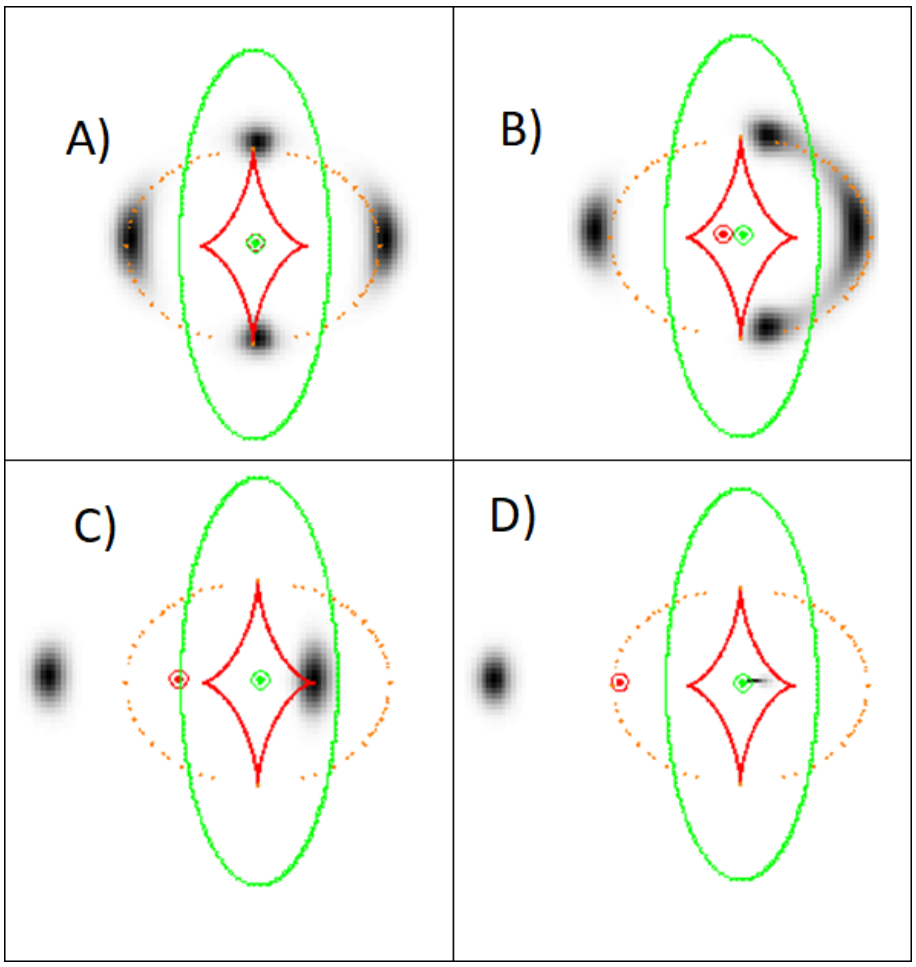

Figure 2.6: Model of gravitational lens caustics using Dr Neal Jackson's igloo software. A) shows a source lying in the middle of the tangential caustic where 4 images are present. B) now shows how three of the four images begin to merge as the source approaches the tangential caustic. C) the source lying on the tangential caustic where the image on the inside of the caustic approaches its maximum possible brightness. D) the source nearly on the radial caustic with one of our images barely still visible before eventually disappearing as the source moves onto and outside of the radial critical line.

2.6 Practical uses of lensing

2.6.1 Lensing galaxy information

Measuring mass distributions and dark matter content can be done by measuring time delays which gives us different arrivals times for each lensed image meaning light from images can lag behind by hundreds of days (Tsupko et al., 2020) and by measuring the magnitude of magnification dependent on the brightness and position of lensed images (Lima et al., 2010).

2.6.2 Observation of faint background sources

Observing faint background galaxies (or in this case a non-thermal radio quiet quasar which exists at the centre of some galaxies) and measuring their properties such as star formation rates, mass, radio and IR luminosity, and redshift is useful for understanding the mechanisms that drove early universe galaxy evolution Benson (2010); Ellis (2010); Mo et al. (2010); Caplar et al. (2018); Cochrane et al. (2021). In the case of RQQs, the increased resolution and brightness provided by the action of the lens allows us to measure the radio and possibly IR flux density which can use used to tell us how much solar mass is formed per year or how much energy an accretion disk around a central SMBH is generating which gives an indicator as to whether the RQQ is dominated by AGN or star formation processes.

2.6.3 Cosmology

The final application concerns the study of cosmology. Gravitational lensing is able to magnify background sources up to a factor up to 20 times (Zheng et al., 2012). The magnifications provided by gravitational lenses allows for a high resolution observations of faint high redshift galaxies which are used for the study of the early history of our Universe (Jackson, 2013).

Cosmological uses would be constraining the Hubble Constant as accurately as possible since using time delays from Gravitational Lenses yields absolute H_0 values so long as the redshifts of the lensing galaxy and lensed object are known; lensing also allows us to constrain dark matter and dark energy contents in the early universe (Refsdal, 1964; Suyu et al., 2012). Kayser & Refsdal (1983) shows that the two images from the quasar 0957+561 come in the form of two wave fronts each having different arrival times and therefore different lines of sight of the background source. The calculations for cosmological parameters

is based on the work of Refsdal (1966) who lay the foundations for cosmological calculations on the assumption of an accurate galaxy mass models and known source and lens redshift. For the galaxy mass models to be precisely accurate we need to know the exact mass which requires us to know the dark matter content of a galaxy with upwards of 80% of a galaxy's mass being from non-baryonic matter (dark matter) in the halo. The determination of halo dark matter mass can be calculated through the use of weak lensing by comparing model deflection angles with measured deflection angles (Massey et al., 2010). Weak lensing is observed when light rays travel far from the lensing mass resulting in slight angles of deflections and a $\sim$ 2% shear which raises SNR in our images but also causes the measured flux in images to increase (Massey et al., 2010; Blandford & Narayan, 1992; Kaiser & Squires, 1993). Recent studies by Bonvin et al. (2016) have shown that strong gravitational lensing can be used to measure the Hubble constant to 3.8% accuracy of H_0 under a flat ΛCDM (cold dark matter) model of the universe.

A database of all the currently known gravitational lensed quasars can be found on the Cambridge lensed quasar Database (Cambridge, 2021) which lists the 220 currently known lensed quasars with links to data from multiple different catalogues.

3 Radio Interferometry

This chapter has key equations and knowledge required when successfully observing with an interferometer as has been presented in van Cittert (1934); Zernike (1938); Crane & Napier (1989); Taylor (1999); Jackson (2008); Thompson et al. (2017). The interferometer used for all primary data collection in this thesis is the VLA (Very Large Array) (VLA, 1972).

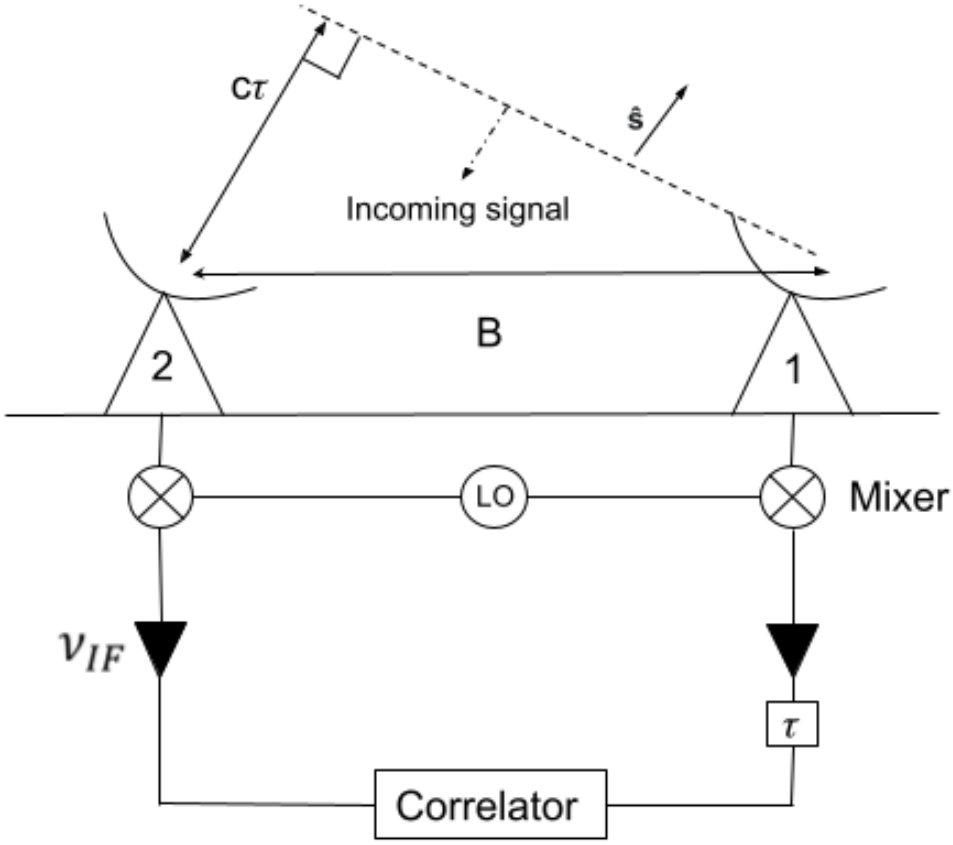

Figure 3.1: Two element radio interferometer with signals first being mixed with a local oscillator giving ν_{IF}, array 1 then has a time delay τ applied to the mixed signal to compensate for the path difference between the arrays $c\tau$, and a correlator combines all the signals of the arrays.

Interferometry is the combination of multiple telescopes to form a large array. Interferometry mimics a full single dish, with a diameter equivalent to the maximum baseline length in the array allowing for larger than normal angular resolution though the sizes of the individual telescopes remains the same. It is important for us to build interferometers as fully steerable dishes become impossible past a dish

diameter (baseline) of ~ 100m as the weight of the dish becomes too much to support. Some examples of well known interferometers are the Very Large Array (VLA) located in New Mexico which consists of 27 apertures each with 25m diameters and a maximum baseline length of 36km (VLA, 1972), and LOFAR which is a series of telescopes setup in multiple European countries with a maximum East-West baseline of 21km and a total collecting area across all arrays of the interferometer of approximately 1-square km (van Haarlem et al., 2013).

For us to correctly analyse high redshift galaxies for properties such as star formation rates or agn activity, we need high angular resolution. For example, to observe structure on 10-100 parsec scales at $z = 0.5$ we need angular resolutions of 1.5-15mas (milli-arcseconds); conventional telescopes do not offer such high resolution and so to achieve high resolution so we must use interferometers (Fanti et al., 1986; Paraficz et al., 2018).

This chapter will be used to summarise the physics of Radio Interferometry as is presented in Anderson (1920); Thompson (1992); Taylor (1999); Briggs et al. (1999).

3.1 The Two Element Interferometer

The two element interferometer combines two telescopes that observe a complex convolution of the sky with the main beam with an added time delay for when observing away from the zenith quantified by τ which needs to be accounted for before a central correlator combines the signals. If an artificial time delay is not added then the signal received by each telescope becomes out of phase and destructively interferes, see time delay subsection. Signals from a single radio telescope do not have to add time delays or correlate signals between apertures because the total signal is only dependent on the single aperture.

The synthesised beam (or the angular resolution) of an interferometer

can be calculated with

$$\theta_b = \frac{\lambda}{b}, \tag{3.1}$$

where b is the maximum baseline between apertures and λ is the observing wavelength. For example, the VLA in A configuration (36km baseline) observing in C band (6GHz central observing frequency) has an angular resolution of

$$\theta_b = \frac{0.05}{36,000} = 1.39 \times 10^{-6}\text{radians} = 0.286''. \tag{3.2}$$

3.2 Time delay

Because an interferometry array has distance between apertures $|B|$ we must take into consideration the time delay of the geometry of observation as shown in figure 3.1 where a time delay τ is shown for the left telescope. To compensate for time delays we artificially add delays to different elements of the array with zero point to a particular element. Time delays are very small and as such require high precision to correctly add or takeaway from our signals otherwise we run the risk of our signals being out of phase which can lead to incoherent images. If we use the VLA for example, with a maximum baseline length of 36km in configuration A, we get a time delay of $\tau = \frac{36\times10^3}{3\times10^8} = 120\mu s$ between the two furthest apertures.

3.3 Response function of an Interferometer

We can take the electric field gathered by the first telescope to be E and that of the second will be $Ee^{ik\mathbf{B}\cdot\mathbf{s}}$ because of a phase delay, $\mathbf{B}\cdot\mathbf{s}$, between apertures where k is the wave number. In a multiplying interferometer we can combine the signals together by multiplying the signals in a

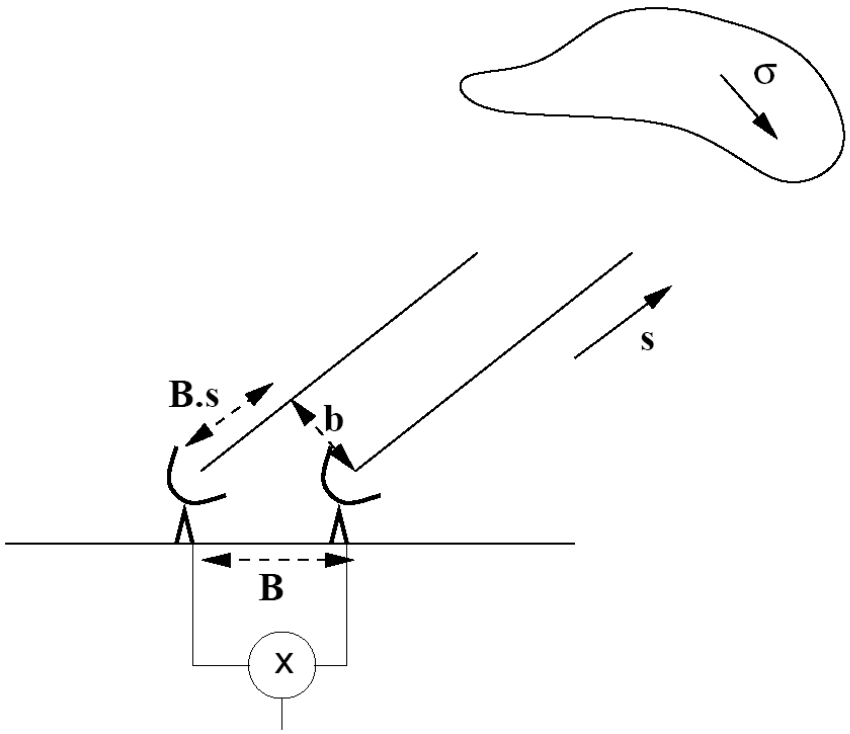

Figure 3.2: Basic 2 element interferometer diagram with baseline **B** and unit vector **s** observing a source described by vector σ which observed as projected baseline of **b**. Diagram from (Jackson, 2008)

correlator and then integrate the fringe patterns over the source we get the response function of our interferometer as originally derived by Van Cittert and Frits Zernike in what is known as the van Cittert-Zernike theorem (van Cittert, 1934; Zernike, 1938; Thompson et al., 2017), see Equation 3.3.

$$R = e^{ik\mathbf{B}\cdot\mathbf{s}} \int I(\boldsymbol{\sigma}) e^{ik\mathbf{b}\cdot\boldsymbol{\sigma}} d\boldsymbol{\sigma}, \tag{3.3}$$

where R is the response function of the interferometer, **B** is the baseline length, $\boldsymbol{\sigma}$ describes the position on the source, **b** is the projected baseline as viewed by the source, **s** is the unit vector in the direction of the source being observed, k is the wave number, and $I(\boldsymbol{\sigma})$ is the intensity for a particular point of the source. The first exponential term is the complex fringe projection in the direction of the source and the second exponential term is the Fourier transform of the source structure (Crane & Napier, 1989; Jackson, 2008).

3.4 u-v plane

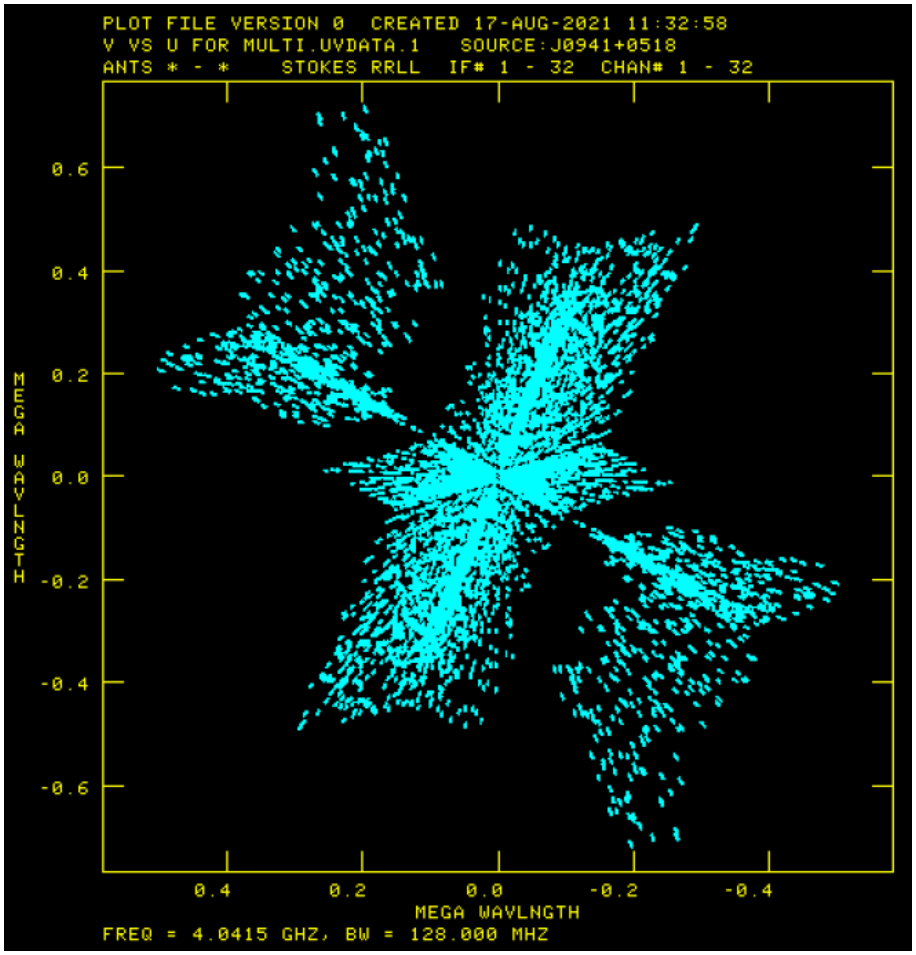

Figure 3.3: The total UV coverage as displayed by AIPS for J0941+0518.

The u-v(-w) plane (also known as the Fourier plane) is a 2-D plane of the spatial frequencies where the smallest spatial frequencies are near the centre and the largest are further out. The ellipses formed in the uv plane as the Earth rotates are the measurements of the spatial frequency of the source at that point in the plane by each baseline where the units of uv are wavelengths. The uv plane is the sampling plane for sky brightness where each baseline corresponds to a single visibility which acts as a point of measurement. For us to have more complete coverage of the sky we must let our baselines trace out the u-v plane so that we can measure more of the spatial frequencies of the source. For an example of uv coverage for the observations in this thesis sample, see Figure 3.3.

We can only measure one fourier component in a particular orientation at once with a single baseline meaning we need to build up a

plane of projected baselines to observe the full source structure. This is known as our sampling function which is used to sample the uv-plane for certain spatial frequencies.

To convert between the baseline vector and uv(w) coordinates we use

$$\begin{pmatrix} u \\ v \\ w \end{pmatrix} = \frac{1}{\lambda} \begin{pmatrix} \sin h & \cos h & 0 \\ -\sin\delta\cos h & \sin\delta\sin h & \cos\delta \\ \cos\delta\cos h & -\cos\delta\sin h & \sin\delta \end{pmatrix} \begin{pmatrix} \Delta X \\ \Delta Y \\ \Delta Z \end{pmatrix}, \quad (3.4)$$

where $u = \frac{1}{\lambda}(\Delta X \sin h + \Delta Y \cos h)$ and $v = \frac{1}{\lambda}(-\Delta X \sin\delta\cos h + \Delta Y \sin\delta \sin h + \Delta Z \cos\delta)$, h is the hour angle and δ is the declination of the source (Segransan, 2003).

3.5 Telescope Calibration

Phase and flux calibration is a requirement before observing target sources to ensure the signal measured is correct. A list of VLA calibrators can be found from Moorsel (2021).

3.5.1 Instrumental delay

An additional electronic time delay must be accounted for equivalent to the geometrical delay between each baseline before signals are correlated otherwise we risk our fringe patterns being lost due to destructive interference (Anderson, 1920). The corrected phase delay

$$\Delta\phi = 2\pi\nu(\tau_g - \tau_r), \quad (3.5)$$

depends on both the geometrical, τ_g, and instrumental, τ_r, delay (Hessels, 2013). Equation 3.5 is the phase difference between the ends

of our band $\Delta\nu$, τ_g is the geometrical delay between signals, τ_r is the instrumental delay caused by physical pieces of equipment processing electronic signals. We want to measure the phase difference to avoid our visibilities being washed out from our signal and by doing so preserves the correlation of the signal between each array in the interferometeter; this is known as fringe stopping (Thompson, 1999).

3.5.2 Atmospheric opacity

The
atmosphere that our source flux must penetrate is constantly changing depending on the source position relative to the observer therefore requiring the source to penetrate different depth of atmosphere which is described by $\tau_a \sec z$, where τ_a is the opacity of the atmosphere and z is the angle of the source from the zenith of the observer. Water vapour present in clouds and air must be accounted for due to their contribution to the atmospheric opacity. The source strength, S, as influenced by atmospheric opacity decreases by $Se^{-\tau_a \sec z}$ and additional noise introduced by the atmosphere to the system $T_{atm}\left(1 - e^{-\tau_a \sec z}\right)$ though the effects of opacity reduction to signal amplitude can be ignored at low frequencies in this case 6GHz (Wang, 2017; Thompson et al., 2017).

To correctly account for opacity, we observe a calibrator source periodically close to the target source due to a time dependent phase shift in the atmosphere which is important as a observing frequencies of a few GHz

At higher frequencies where water vapour becomes a relevant component of opacity (Wang, 2017) we require very stable system and antenna gain which could cause confusion as we sweep through the sky. Instead, we can use tipping curves whereby total antenna power gain is continuously measured from zenith to horizon. With this, the atmospheric opacity can be approximated by

$$\tau_a = \alpha_0 + \alpha_1 P_v, \tag{3.6}$$

where α_0 and α_1 depend on frequency and P_v is the water vapour pressure in millibars.

3.6 Limitations

Collecting power - Although interferometers can be perceived as large as a single dish with diameter equivalent to the maximum baseline, the collecting power of interferometers is not equivalent to a single dish with a theoretical diameter equal to the maximum baseline of an interferometer. Thus, it is important for our interferometer to trace out across the u-v plane to cover as much of the uv image plane as possible to account for gaps in our coverage.

Primary beam - The primary beam of an interferometer is limited by the size of the smallest dish in the array meaning that our field of view (FOV)

$$FOV \sim \frac{\lambda}{D}, \tag{3.7}$$

where FOV is in radians, λ is the observing wavelength, and D is the effective dish diameter, is the same as a single dish telescope with dish diameter $D_{eff} = D \times \eta$ where η is the efficiency factor. A limited primary beam also decreases survey speeds across the sky hence delaying observations of patches of sky.

Bandwidth smearing - Assuming a finite bandwidth, fringes become smeared the further our signal is from the centre of the FOV. Larger bandwidths have a greater reduction effect on the FOV according to

$$FOV = \frac{\lambda}{\Delta\lambda}\frac{\lambda}{D}, \tag{3.8}$$

where $\Delta\lambda$ is the bandwidth. The solution to bandwidth smearing is to split the bandwidth into many channels and correlate them separately, this however increases the amount of computation time required by a factor N where N is the number of channels.

Integration time per data point - We must be considerate of integration time per sample due to the FOV being directly tied to the integration time

$$FOV = \frac{\lambda}{b}\frac{86400}{2\pi\tau}, \tag{3.9}$$

where τ is the integration time per sample and b is the maximum baseline length. The maximum integration time per sample for the VLA observations before smearing becomes an issue is ~ 9.5s for a primary beam FOV of 495 arcseconds, λ is 5cm, and maximum baseline of 36km. However, the penalty for having small integration times and a large FOV is a large data volume which requires more computer power and time to process with a scaling factor N such that a 10 times smaller integration time will increase the computer processing time by 10.

Telescope sensitivity - The sensitivity, S, is the RMS noise of the array and hence the faintest object that can be detected, however, the faintest detection is usually taken to be a few standard deviations of this value for absolute certainty of a detection. Sensitivity, Wm^{-2}, for each polarisation is measured by

$$\Delta S(Wm^{-2}) = \frac{\sqrt{2}kT_{sys}}{\sqrt{\tau\Delta v}A_e\eta_a\sqrt{n_b}}, \tag{3.10}$$

where k is the Boltzmann constant, T_{sys} is the total system temperature of the interferometer, τ is the integration time, Δv is the bandwidth, A_e is the effective collecting area, η_a is the efficiency, and n_b is the number of baselines; derivation by (Crane & Napier, 1989). The number of baselines in our array is calculated by

$$n_b = \frac{N(N-1)}{2}, \tag{3.11}$$

where N is the number of telescopes in our array. For the VLA with 27 antennas, the total number of baselines is $n_b = \frac{27(27-1)}{2} = 351$ and estimating a system temperature of 30K and telescope efficiency of 70% with the total integration time on source, see results section, being 20 minutes the theoretical sensitivity is

$$\Delta S(\mathrm{Wm^{-2}}) = \frac{\sqrt{2} \times 1.38 \times 10^{-23} \times 30}{\sqrt{20 \times 60 \times 4\mathrm{GHZ} \times \pi \times (\frac{25}{2})^2 \times 0.7\sqrt{351}}}, \tag{3.12}$$

where $\Delta S(\mathrm{Wm^{-2}})$ = 4.15$\times 10^{-32}$Wm^{-2} = 4.15μJy.

3.7 Deconvolution and CLEAN

To CLEAN an image we must use the convolution theorem to separate the dirty map (DM) and dirty beam (DB) from the correlation function which at which point we use the DM along with a cleaning beam to subtract source flux density from the DM. The DM is the sky brightness distribution combined with the dirty beam and noise. Information about CLEAN and the role convolution plays in CLEAN is taken from Hogbom (1974).

Convolution The convolution theorem states that the convolution of two functions is the same as the multiplication in fourier space

$$f * g \overset{FT}{\rightarrow} F \times G, \tag{3.13}$$

where $\overset{FT}{\rightarrow}$ indicates a forward fourier transform, f and g are normal functions and F and G and the forward fourier transforms of f and g. As seen in equation 3.13, where we can convolve two function we can multiply them together in the fourier plane to get the same result.

To retrieve the DM and DB we must perform the inverse fourier transforms

$$DM \overset{FT}{\leftarrow} W \cdot p \tag{3.14}$$

$$DB \overset{FT}{\leftarrow} p, \tag{3.15}$$

where p is the weight as a function of u and v $p(u, v)$ and W is the correlation function.

CLEAN During CLEAN we subtract the DB from the DM by selecting the source flux density according to the maximum flux density of the DM I_0 where we then remove scaled versions of the DB which are coincident with the maximum flux density point in the DM. We repeat this process over N iterations until all the source flux density has been removed and the DM maximum value I_0 drops to a level no longer significant in the map thus leaving us with a residual map consisting of only noise.

4 Methodology

This section will discuss the observations and calibration of data as well as discuss the types of data used in SED (Spectral Energy Distribution) models with a brief discussion about the FIRC (Far infrared-correlation).

4.1 Observations

The data within this thesis was obtained using the VLA interferometer, New Mexico, which can have telescopes in one of four configurations. The configurations A, B, C, and D (and also BnA for surveys) are four distinct arrangements of the 27 telescopes, see table 4.1 (NRAO, 2021).

Configuration	Max baseline (km)	Max Ang resolution" 6GHz
A	36.4	0.283
B	11.1	0.929
C	3.4	3.033
D	1.03	10.013

Table 4.1: VLA configurations with a central observing frequency of 6GHz assuming a system temperature of 30K, integration time of 20 minutes, 4GHz bandwidth and 70% aperture efficiency. Calculated resolution values from Equation 3.1. Configuration information available at NRAO (2021).

Each source was observed in C band (6GHz) with a 4GHz bandwidth for approximately 20 minutes with a further 10 minutes on the phase calibrator source. The bandwidth was split into 32 spectral windows each with 32 channels where each channel is 4,000kHz and the spectral window has a total bandwidth of 128MHz. All 27 array elements were operational and the telescope elements were a mix of configuration A and B due to covid-19 leaving technical staff unable to fully re-arrange the telescopes into configuration A. Figure 4.1 shows only the North arm fully extended, the South-West arm only has two antennas extended

fully (ea26 and ea03) with ea13 partially extended whilst the rest still remain in their configuration B positions, and the South-East arm is still in configuration B, see figure 4.2 for A configuration. The mixed configuration hindered the uv coverage of each observation and the angular resolution with the maximum baseline during observation being 25481m giving an angular resolution of $\theta_b = 0.40''$ which is $\sim$18% worse than with maximum baseline length 36km in full configuration A.

A total of 12 out of 22 observed sources were detected in the radio at or above 3σ where σ is approximately 4.0μJy when using a dual polarised setup with natural weighting. Natural weighting was chosen to ensure a low RMS noise level as 9 of the 12 sources have combined image flux densities <100μJy with 5 of 12 sources having image components with 4σ which is barely above the RMS noise level. Uniform weighting would allow for sharper images which would be useful for smaller scale observations of the RQQs but for the analysis in this thesis this wasn't required. All sources observed met the conditions;

- Identified as double lensed quasars according to those listed by Cambridge (2021)
- Have declinations between +25 and -20 degrees for potential follow up ALMA, e-MERLIN, and VLBI observations
- Identified as Radio Quiet i.e. <10mJy at L-band (1-2GHz)
- Not already studied or proposed with the VLA

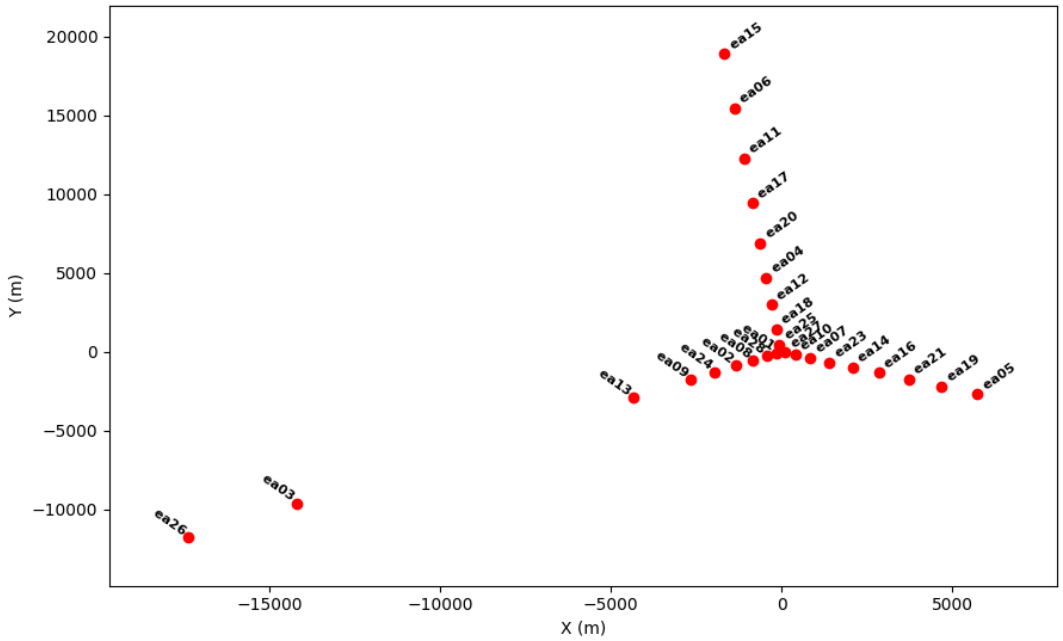

Figure 4.1: Positions of the VLA apertures during the time of observation of my sample whilst in partial configuration B→A.

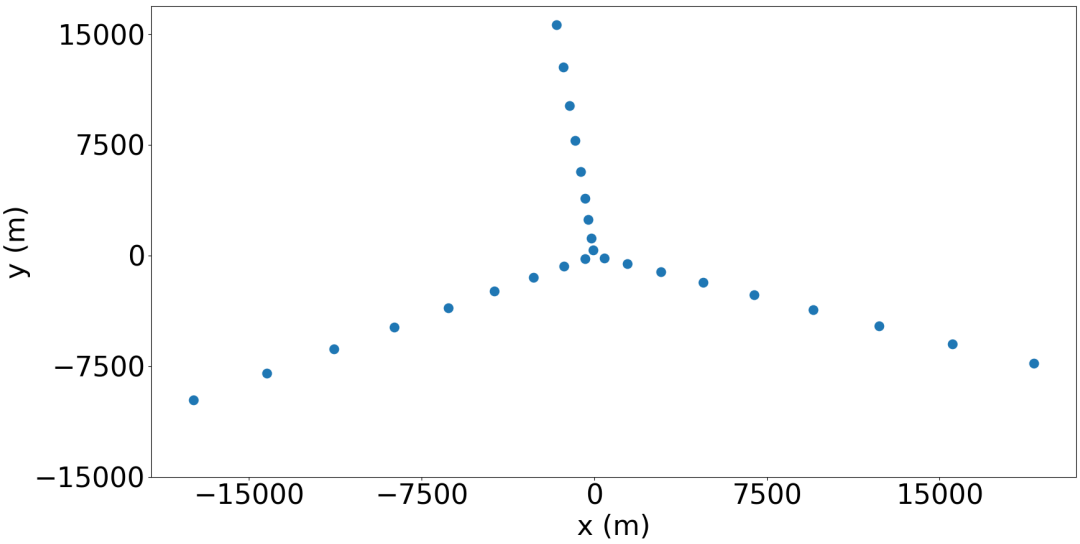

Figure 4.2: Positions of the VLA apertures as they would appear from above in configuration A.

4.2 Calibration

Observational calibration

We use bright point-line sources, with well known positions that are close to our observing source, as our gain calibrators (Moorsel, 2021) where the atmospheric phase rotation is similar between the source and calibrator. Gain calibrators are ideally chosen to be sources with SNR (Signal to Noise Ratio) much greater than 1. Any calibrator within 15 degrees (max) of our

target is ideal but calibrators closer to the source are much better due to the difference in phase through the atmosphere being considerably less if the angle at which we swap between the calibrator and target source is smaller. However if we do not have a strong calibrator within reasonable distance to our target, then we can use a more distant strong calibrator, and a closer dimmer calibrator (Browne et al., 1998).

4.3 VLA pipeline

The recipe reducer pipeline method was used which has pre-determined variables for different types of data, one of which is VLA data. More information is available from the official VLA pipeline procedure which is also the source for all figures used in this subsection (CASA, 2021).

Stage 1 - Importing data The raw VLa data comes in a raw measurement set (MS) file which contains all the information of the observation including sources, times, beam sizes, and observer (in this case Dr Neal Jackson requested the observations). More information can be accessed by loading a visibility (ie the .MS file) into the task ”listobs” which when run will output all the main observing data into the CASA console.

The visibility files contained either one or two target sources with each having their own phase calibrator but shared flux density calibrator. The structure of each observation block was to observe the flux density calibrator for 4 scans over approximately 12.5 minutes. The target sources and phase calibrators were then observed over 10 scans which covered an observing time of 30 minutes with 10 minutes being for the phase calibrator across 5 scans and 20 minutes for the source on the other 5 scans. An example observing time block can be seen in table 7.2

Stage 2 - Hanning smoothing The hanning smoothing task removes what is known as the Gibbs Phenomenon (Thompson, 1992) which is when there is strong RFI or maser lines thus Hanning smoothing removes the extra flux density where it has spilled over into adjacent spectral

windows. This task is performed by applying a triangle kernal across the RFI which reduces the ringing effect but also reduces the spectral resolution by a factor of 2. Hanning smoothing therefore removes all amplitude spikes which is associated with bad data.

Stage 3 - Deterministic flagging Deterministic flagging reads from a log at time of observation which tracks when specific antenna are not on source, when an antenna is positioning itself, or removing channel edges from each spectral window which generally have poor SNRs and phase. It is important to keep track of this information so we do not include signal data from when a telescope sweeps through the sky and to remove the poor phase data from the band edges.

Stage 4 - Calibrator models The VLA uses known bright quasar models to calibrate the flux density of the observation to ensure the flux density scale is set correctly. The flux density calibrators used in this thesis are 3C48, 3C138, 3C147, and 3C286 which have flux density 4.42, 3.39, 6.45, and 6.39Jy respectively. The 2016 standard flux density calibrator values at 6000MHz (C band - same central observing frequency of observations in this thesis) and a list of all calibrator sources are available at Moorsel (2021).

Stage 5 - Priorcals Priorcals creates a table of data from the flux density calibrator including the gain-elevation dependencies and atmospheric opacity corrections which are non-linear throughout the observation. Priorcals also records weather details such as air humidity and wind speed.

Stage 6 - Test calibrations The bandpass solutions must be determined from bright and flat spectrum sources so that later in the pipeline any bad RFI data can be identified and flagged. The phase and gain solutions are calculated which is important so that frequency dependent errors do not propagate into the positional offsets of spectral features which may mimick the doppler motions.

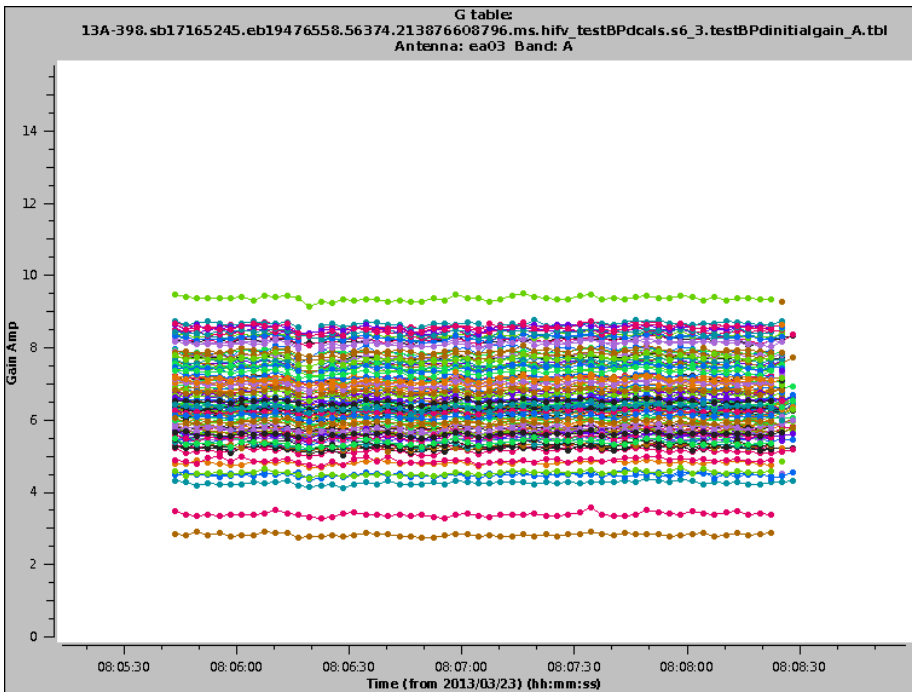

Figure 4.3: A good example of antenna ea03 which has good solutions across all spectral windows which is demonstrated by the relatively flat profile gain amp over time.

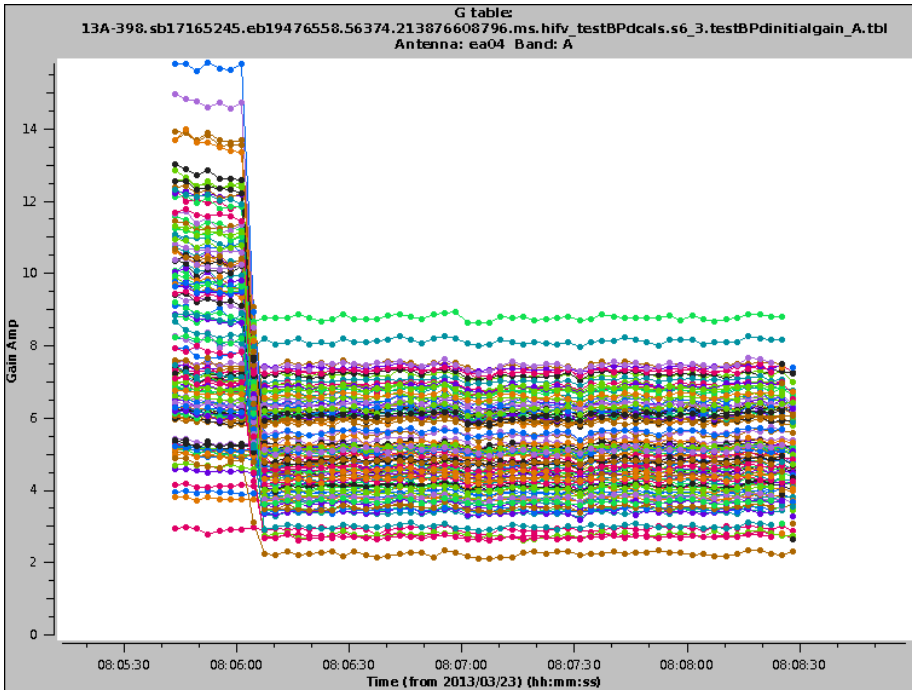

Figure 4.4: Antenna ae04 in this example has a similar flat profile except for the beginning of observation whereby there's a large spike which should be flagged.

Flagging Bad data

The transfer of data involves a conversion from electronic to optical signal before it's once again passed through an optical fibre link. However, if the deformatter timing is misaligned then large amplitude and phase slopes

can be added to the data similar in shape to a |sin| wave. The solution is searching for signal deviations across the bandpass over 15% and then flagging those spectral windows, if more than 4 spectral windows are identified with a 15% deviation then the entire band will be flagged.

Figure 4.3 and figure 4.4 show examples of no flagging and some flagging being required.

Stage 7,8,9, and 10 - rflag and Bpass calibrations

Stage 7 - rflag

The task flagdata has a sub-task called ”rflag” which searches for signals based on an automatic threshold algorithm that searches for relatively bright RFI.The purpose of this task is to ensure only good signals are kept for when bandpass calibrations are rerun later on. At this stage, rflag is only run on the bandpass calibrator.

Stage 8 - Semi-final calibrations

From the previous stage, the most present bad data has been flagged with rflag and so we return to stage 6 to recalculate bandpass and delay solutions.

Stage 9 - rflag repeated

Rflag is run a second time to remove weaker RFI from the new solutions after stage 7 removed the bright RFI.

Stage 10 - semi-final calibrations

Stage 6 is repeated a 3rd time now that most of the bad RFI has been removed.

Stage 11 - ”Solint” and test gain ”Solint” represents the times for the visibility integration time which is the observing time on the target source and the calibrator scan time which is the time on the gain calibrator. The shortest ”solint” time refers to the maximum gain calibrator scan time

and the longest ”solint” time refers to the maximum visibility integration time.

Phase solutions

The time intervals calculated from ”solint” are used for the the gain and phase solutions for each antenna, polarisation and spectral window for the target sources. Ideally, phase solutions will be close to zero, see figure 4.6, unlike the phase in figure 4.5 and will instead have phase close to zero such that further phase calibration solutions will also be close to zero.

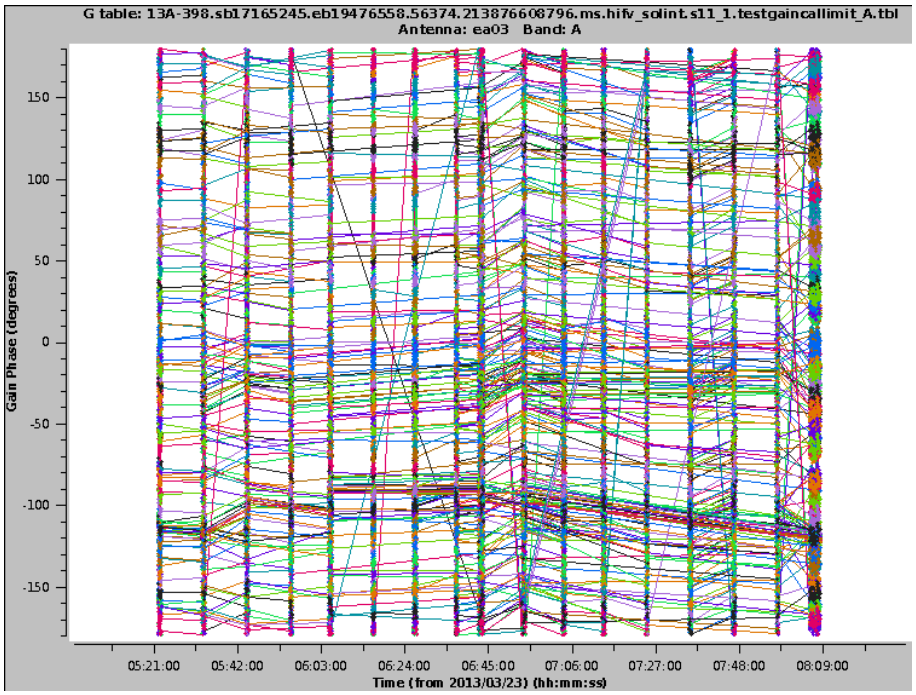

Figure 4.5: An example of initial antenna ea03 which has a very crowded gain phase vs time plot but also has very steady values where each spectral window has relatively little variation.

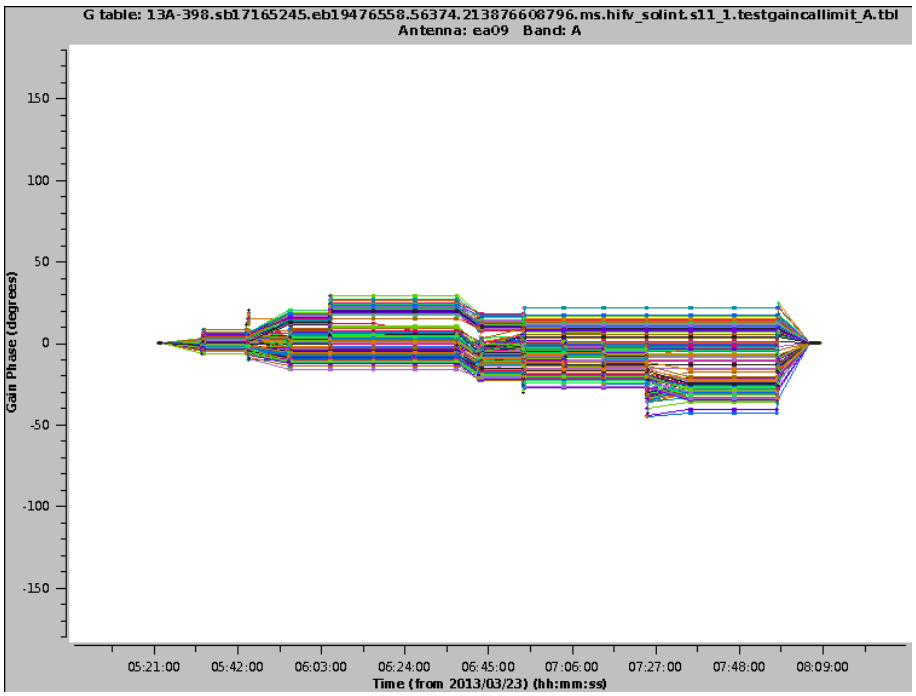

Figure 4.6: An example of antenna ea09 shows a close to ideal case of all spectral windows having flat phase vs time with all solutions lying close to zero.

Stage 12 - Gain table Flux densities from a flux calibrator are now bootstrapped to the complex amplitude and phase calibrator via a polynomial function fitted to a secondary calibrator and then the task setjy is run on the flux calibrators. Setjy will cycle through all spectral windows and channels for the flux calibrator and set a flux density based on a model which defaults to that used by Perley-Butler 2017 (nrao, 2021). The majority of calibrators are compact radio AGN (Conway et al., 1963; Doherty et al., 1968) which are used due to their large flux density.

Stage 13 - Final calibration table Solutions for the calibrator are then examined by looking at the gain amplitude vs time, gain amplitude vs frequency, and gain amplitude vs time figures which ideally should all have flat profiles with no spikes at all.

Stage 14 - Apply calibrations With a final solution table as verified in stage 13, we can apply our calibrations to the dataset with task ”applycal” which adds the solutions to a calibrated data column in our MS file. The applied calibrations maintain all data flags and also failed calibration solutions whereby failed calibrations will eventually be flagged.

Stage 15 - Targetflag Once the calibration tables are applied with ”applycal”, the sub-task ”rflag” is ran once more on all sources in the data set to remove any RFI and outliers from the data that the calibration table did not remove.

Stage 16 - Reweighing visibilities Due to the nature of observations having variable conditions such as opacity, elevation, and temperature, we must account for the weighting on the noise from these changes. The task ”statwt” increases the SNR ratio of images which is also affected by spikes in the RFI and spectral lines. Re-weighting can potentially raise the SNR enough such that source flux density is lost in the radio maps when we later run the TCLEAN task due to the SNR potentially being at or above the flux density of our target source.

Stage 17 - VLA plot summary Plots of the final calibrated data are made for diagnostic use where amplitude vs frequency plots for each target can be used to determine the presence of RFI which can then either be manually removed or require a second pipeline run if the calibration sources still have poor RFI and phase.

Stage 18 - Images to be calculated Calibrators have all spectral windows combined such that diagnostic images can be made; the images are then saved in the same directory as the MS file. The list information such as source name, spectral windows included in the creation of the image, and number of channels.

Pre-Stage 19 Before cleaning the target sources, the calibrators are checked to ensure the flux densities are correct. For example, J0137+3309 (3C48) has a flux density of ~ 4.42Jy and so a successful flux calibration will give a measured flux density close to this (VLA, 2016). See figure 4.7 for a good flux calibration.

Stage 19 - TCLEAN TCLEAN is based off the CLEAN algorithm. TCLEAN works by identifying the brightest pixel of flux density in an image and then removes a region around it from the dirty map and adds the

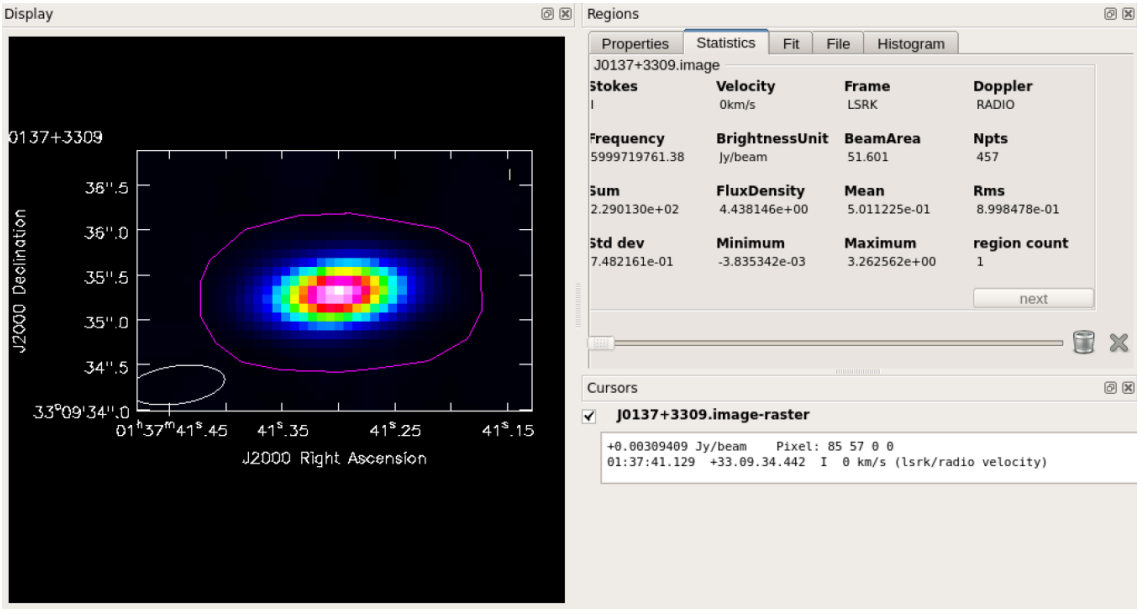

Figure 4.7: The measured flux density of flux calibrator J0137+3309 is 4.44 Jy which matches with the correct value confirming the flux calibration is successful. (Note, the region made is very likely not ideal and more or less flux could be included belonging to J0137+3309).

removed flux density to a PSF (point spread function) over a number of iterations N specified by the user. A minimum flux density level is also given as an input which allows the algorithm to stop when the brightest pixel reaches the input flux density or the number of iterations N is reached. Assuming the total input interactions are completed then the algorithm should be ran again until the minimum flux density is met. The products of TCLEAN are the residual map which is the source flux density subtracted away from the dirty map, a model of the source, a point spread function and primary beam file, and the deconvolved image on a background of rms noise (CASAdocs, 2021).

From the image we are able to record the flux density of the source by using the selector tool with the task ”viewer”. When recording the flux density it’s important to select all flux density that is associated with the source and not just the most bright source structure we can see on the map. For example see Figure 4.8 and 4.9.

The RMS noise of the background must also be measured to collected the error influence on the image flux densities.

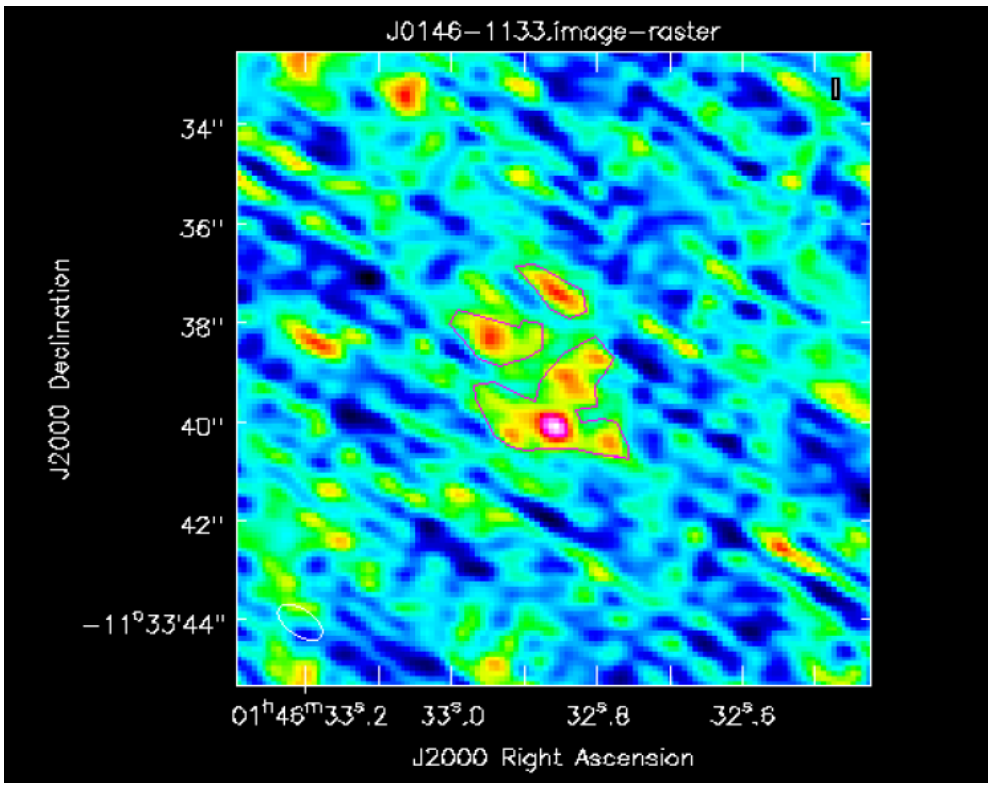

Figure 4.8: Here the lens J0146-1133 has regions making sure to include as much of the flux density as is reasonable to belong to just the images.

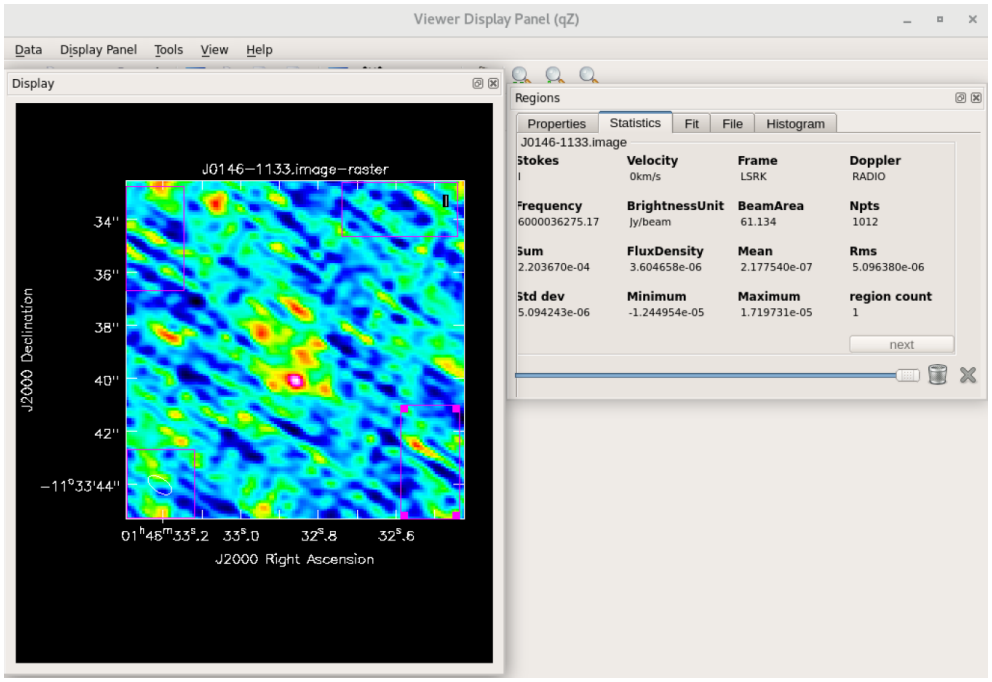

Figure 4.9: Multiple regions are drawn on the background away from the source as to avoid potential flux density contamination and then the RMS flux density is collected for each region and divided by the number of regions to find an averaged value. In instance of the bottom right rectangle as highlighted, the RMS flux density has a value of approximately 5.1μ Jy which is close to the theoretical rms noise of the VLA at 6Ghz, 4GHz bandwidth, natural weighting, and 20 minute on source time. For this J0146-1133 the average rms noise is approximately 4.43μJy

4.4 Data

It's important to gather as much available information as possible in the MIR/FIR regime as possible for use in calculations of SFR and Q_{IR} so that we can determine whether a RQQ has dominated radio emission due to star formation or not. The emission mechanisms of RQQs, and by extension RLQs, has long been debated with many arguing for and against bimodility with a single dominate radio emission mechanism to separate RQQs and RLQs. By extension, the same debate is currently undergoing with recent work from Hartley et al. (2021) providing evidence that the FIR-correlation is not a perfect indicator of emission mechanism in all cases (see results section for further discussion). Thus, the data collected for this thesis is part of an on going discussion as to the emission mechanisms of radio quiet quasars.

4.4.1 VLA data

The VLA radio data is not relevant to the SED but was plotted anyway for reference as to where the spectral index would change from the thermal dust bump in the IR regime to radio regime where the thermal dust bump corresponds to the cold dust emission rather than the optical-ultra violet associated with an accretion disk. The VLA radio data will be used in the results section when plotting sources on the FIR-correlation which will be used for theorising an emission mechanism for each source.

The data contained within this thesis is half of the total with that being shared with Dr Shruti Badole as part of a larger collaboration. 62 sources were proposed for the collaboration and 55 were given observation time. This thesis contains 22 of the 55 sources given observation time with 12/22 having lensed RQQ image radio detections >3σ ($\sim 10\mu Jy$).

4.4.2 Herschel SPIRE data

From Stacey et al. (2018) some data at 250, 350, and 500μm for four of the sources detected with the VLA were collected. Sensitivity of Herschel-SPIRE is 5.8, 6.3, 6.8mJy at 250, 350, and 500μm respectively (Griffin et al., 2010). Stacey et al. (2018) used the data from the Herschel SPIRE observations to derive a FIR flux density integrated between 40-120μm.

4.4.3 Herschel PACS data

A search for Herschal-PACS, which has imaging bands at 70,100,160 μm, was undertaken. However, none of the sources appeared in any available archived field observations which left upper limits unusable for the SEDs (Pilbratt et al., 2010).

4.4.4 AKARI data

The AKARI/IRC FIR survey was an all-sky survey covering >99% of the sky operating between 9μm and 200μm for which the 65,90, 140, and 160μm bands were most relevant for deriving FIR flux density (Doi et al., 2015). Unfortunately, no sources had detections with AKARI but since the entire sky was surveyed upper limits 22, 6.8, 70, 270mJy at 65, 90, 140, and 160μm respectively were applied to the SEDs (Kawada et al., 2007).

4.4.5 IRAS data

IRAS was an IR survey of >95% of the sky operating between 12 and 100μm whereby two bands were in the FIR, those being 60μm and 100μm (Neugebauer et al., 1984). Because the survey was virtually full sky the upper limits values of the IRAS telescope were collected since many of the sample sources had not been detected but had

been observed. Upper limits for 60 and 100μm are 85mJy and 300mJy respectively (IRa, 1988; Joint Iras Science, 1994).

4.5 SED

Code used for all data analysis was a collaboration between the author and Dr Shruti Badole.

All FIR flux density gathered was integrated from the SED model between the rest-frame 40-120μm which is defined as the FIR-regime by Helou et al. (1988). A modified blackbody radiation equation which accounts for emissivity index was used when plotting the model

$$S_\nu = A\frac{\nu^{3+\beta}}{e^{\frac{h\nu}{kT}}-1}, \tag{4.1}$$

where ν is the frequency of observation in Hz, β is the emissivity index, T is the temperature in Kelvin, A is a proportionality constant to be found, h is the Planck constant, and k is the Boltzmann constant.

Data was plotted in the rest-frame of the SED by multiplying the observing wavelengths by a factor $\frac{1}{1+z}$. The model depends on 3 variables, β, T, and A which is always left free as it is a proportionality constant. Therefore, 4 versions of the model was run with either; 1) all parameters (β and T) free, 2) β fixed, 3) T fixed, and 4) β and T fixed where fixing β and is at a value of 1.5 and 38K respectively (Stacey et al., 2018). A spectral index, β, 0 to 2 indicates a thermal source of radio radiation as is the case in the FIR regime whereas a spectral index -0.5 to -1.5 indicates a non-thermal origin of radio emission such as synchrotron radiation. The SED model for each source used fits the data whilst also not enclosing any upper limits (therefore making the model non-physical).

For sources with a flux density > 100μJy, the radio band was split in two at 5GHz and 7GHz so that a spectral index could be measured using the model

$$S_v = A\nu^{\alpha}, \tag{4.2}$$

which returns optimised parameters for the spectral index α.

4.5.1 FIR derivation from model

The model variables were calculated using the python package, scipy, which is a mathematical packaged run alongside numpy. When optimising the variables scipy.optimize was used which tries to minimise (or maximise) the variables for the blackbody model function, i.e. in this case the modified blackbody function, over a number of iterations after which it returns the best fit variables (Numpy, 2021; Scipy, 2021).

Since 11/12 of the sources had only upper limits or mostly upper limits a model fit had to lie below any upper limit data as to ensure the maximum FIR was not non-physical, this was done by applying a penalty function to the least-square model fit. The penalty function checked if any upper limits lay within the model and if so created new data points of the original upper limits with 2% smaller flux density before recalculating parameters and checking again if any upper limits were within the model fit, the reduction of peak was done in continuous 2% intervals until no original upper limits were within the model fit, the newly created points with 2% reduced flux intervals were then removed leaving only the model, the data points, and the original upper limit data points. For sources with less than 4 data points a emissivity index β of 1.5 is assumed to satisfy *dof = data points - free parameters*, where the condition $dof > 0$ (Degrees of freedom) has to be satisfied. For sources with only upper limit data both an emissivity index of 1.5 and temperature of 38K is assumed (Stacey et al., 2018).

Helou et al. (1988) gives the FIR luminosity regime as that which lies

between $40 - 120\mu$m such that we can calculate the FIR luminosity as

$$L_{\text{FIR}} = \frac{4\pi D_L^2}{1+z} \int_{40\mu\text{m}}^{120\mu\text{m}} S_{\nu,\text{rest}} d\nu, \tag{4.3}$$

where D_L is the luminosity distance, in Mpc, calculated under the assumption of a flat ΛCDM cosmology model with Hubble constant $H_0 = 67.8$kms^{-1}Mpc^{-1}, matter density $\Omega_M = 0.31$, and ratio of energy density and critical density $\Omega_\Lambda = 0.69$ (Planck Collaboration et al., 2016).

4.6 Radio-Infrared correlation function

The radio-infrared correlation is an empirical correlation between the radio and FIR luminosities whose physical origin is likely to be star formation (de Jong et al., 1985; Helou et al., 1988; Sauvage & Thuan, 1992; Roussel et al., 2001; Bell, 2003). The origin of the IR comes from the heating of dust from stellar populations in H_{II} regions through non-ionising UV radiation which excites the electrons in the interstellar medium (ISM) raising them to a higher state before they lose energy by re-emitting photons in the IR regime (8-1000μm). The origin of the radio emission is from stars going supernova whereby their remnants accelerate electrons producing synchrotron radiation emission as they pass through the interstellar magnetic field losing energy via Compton scattering and also from thermal free-free emission from the thermal heating of electrons in H_{II} regions. We can define Q_{IR} as the ratio of the IR and radio luminosity. Therefore if we have an object with a radio excess then the Q_{IR} indicates that there is not much UV excitation of the ISM through solar heating and as such it indicates either synchrotron dominated radio emission about the AGN or large stellar populations going supernova causing synchrotron radiation through the expulsion of electrons through the ISM (Acosta-Pulido et al., 2015). The ratio of rest-frame IR luminosity and 1.4GHz luminosity is measured by

$$Q_{IR} = \log_{10}\left(\frac{L_{\mathrm{IR}}}{3.75 \times 10^{12} L_{1.4\mathrm{GHz}}}\right), \tag{4.4}$$

where

$$L_{1.4\mathrm{GHz}} = \frac{4\pi D_L^2 S_{1.4\mathrm{GHz}}}{(1+z)^{1+\alpha}}, \tag{4.5}$$

where D_L is the luminosity distance, $S_{1.4\mathrm{GHz}}$ is the flux density at 1.4GHz, and α is the emissivity index (for future calculations $\alpha = -0.7$).

The IR luminosity is the summation of flux density in the rest-frame between $8-1000\mu$m and is derived from the FIR luminosity with a colour correction of 1.91 such that $L_{IR} = 1.91 L_{FIR}$ (Dale et al., 2001). Ivison et al. (2010) found a value of Q_{IR} =2.40$\pm$0.24 which will be used as the reference value for the quasar dataset in the FIR-correlation sub-section although ambiguity of the FIR-correlation is discussed in the results section.

4.7 Star formation rate

To calculate the star formation in solar masses per year we use

$$SFR(\dot{\mathrm{M}}_* \mathrm{yr}^{-1}) = \frac{\mathrm{L}_{\mathrm{IR}}}{5.8 \times 10^9}, \tag{4.6}$$

where L_{IR} has units of solar mass per year, $\mathrm{M}_* \mathrm{yr}^{-1}$, which is valid assuming a Salpeter initial mass function (IMF) (Kennicutt, 1998; Salpeter, 1955).

5 Results & Discussion

This section will discuss the radio detections from the VLA; the SEDs corresponding to each source with any FIR/MIR data gathered; and finally the FIR-correlation and the implications of the data as it appears on the correlation. The radio overlays with a visually obvious offset had the centre radio component coordinates checked against Gaia observation coordinates to confirm astrometric error from Pan-STARRS (Chambers et al., 2016; Gaia Collaboration et al., 2018).

5.1 VLA Detections

This subsection will briefly summarise the detection of each source with key information such as the 6GHz flux density and any abnormalities in the image. The brightest of the two images, in C band, will always be referred to as image A. All radio-optical overlays, see figure 7.3, show contours at 10, 15, 20, 30, 40, 60, 80, 100, 120, 140, and 160μJy where 10μJy (2.5σ) is the absolute minimum required flux density before structure of the source in the radio is shown separate from the background RMS noise map and 160μJy is the approximate flux density of the brightest image in the dataset.

Some of the radio-optical overlays may also appear misaligned even after the radio and optical images were placed on the same astrometric frame due to Pan-STARRS having an astrometric error of approximately 130mas (Milani et al., 2012; Denneau et al., 2013). The approximate offset error in the radio-optical overlay maps is 40mas RA and 100mas declination which is within reasonable astrometric error of Pan-STARRS r band optical images.

J0011-0845 was discovered by Lemon et al. (2018a). Both images A and B were detected and had measured radio flux density of 18.19μJy and 16.92μJy respectively in CASA with a noise level of 5.22μJy. J0011-0845

is barely above the 3σ noise level required for detection but both radio images are clearly present in the radio-optical overlay. Gaia observation coordinates match precisely with the centre of the radio image centres (Gaia Collaboration et al., 2018).

J0146-1133 was discovered by Agnello et al. (2018b) and later confirmed by Lemon et al. (2018a). Both images A and B were detected with measured radio flux density of 68.22μJy and 34.43μJy respectively with a 4.43μJy rms noise level. Both images were split into multiple radio components requiring multiple regions to be drawn to account for each image's flux density. The multiple radio components for each image possibly indicates that there are multiple radio components in the source which have each been doubly imaged by the lens. Multiple radio components in each image indicates there may be extended radio emission in the source which is indicative of star formation. Gaia observation coordinates have confirmed that the centre of the brightest radio components match precisely with each image (Gaia Collaboration et al., 2018).

J0203+1612 was discovered by Lemon et al. (2019). Only a single image was detected and had a measured radio flux density of 73.11μJy with an rms noise level of 4.21μJy. The radio flux density likely corresponds to the lensing galaxy due to the astrometric error being 130mas which would not correct the offset enough. We would also expect the brighter lensed image to have the most radio emission unless there was some obscuring medium or optical flux variations and so the flux density measured must belong to the lensing galaxy. On inspection of the Gaia coordinates for J0203+1612 it is confirmed that the radio component belongs to the lensing galaxy (Gaia Collaboration et al., 2018).

DESJ0245-0556, first identified by Agnello et al. (2018c) and later confirmed by Lemon et al. (2020) was observed with the NIRC2 narrow camera in the K band. Both images were detected with radio flux density 31.37μJy and 18.10μJy; the fainter image is present in the radio map but

only has a $\sim 4\sigma$ and the map has an rms noise level of 5.13μJy. Agnello et al. (2018a) has presented DESJ0245-0556 as part of the DES multiplets which class of observations with contamination in the form of very faint galaxies or foreground stars but in this case the radio emission very likely comes from a faint galaxy. Coordinates from Gaia match perfectly with the centre of both radio images confirming the radio to belong as such (Gaia Collaboration et al., 2018).

J0246-1845 was discovered by Lemon et al. (2020), and also independently discovered by Krone-Martins et al. (2019), was observed via followup using the NIRC2 camera. Both images were detected with flux densites 52.81μJy and 21.45μJy with a measured rms noise level of 5.81μJy. The radio overlay offset with the Pan-STARRS optical has been confirmed to be due to astrometric error with a comparison of the radio coordinates with Gaia observational coordinates (Gaia Collaboration et al., 2018).

J0246-0825 was discovered by Inada et al. (2005). Both images are detected with flux densities 24.17μJy and 20.97μJy with an rms noise of 4.70μJy. The overlay image is a poor example of the radio and optical regions coinciding but this is likely attributed to the Pan-STARRS 60mas astrometric error and the low level $\sim 5\sigma$ detection.

SDSSJ0256+0153 was discovered by More et al. (2016). A single image was detected and has a radio flux density of 107.08μJy with an rms noise of 5.19μJy. On further investigation this radio emission is likely from the lensing galaxy as the radio contours coincide perfectly with the lensing galaxy coordinates (02:56:40.740, +01:53:29.12) and without huge optical flux variations it would be very unlikely that a radio detection for the fainter image would be the only detection in the map.

SDSSJ0806+2006 was discovered by Inada et al. (2006). A single image was detected with radio flux density 62.61μJy and has an rms background noise level of 4.4384μJy. It is possible the second image was detected but the radio map near the second image shows that

more RFI flagging and potentially a second run of the CASA pipeline is needed to confidently measure the flux density of the second image. Gaia coordinates confirm that the radio component matches with the optical image (Gaia Collaboration et al., 2018).

SDSSJ0818+0601 was discovered by both More et al. (2016) and Hutsemékers et al. (2020). Both images were detected and the measured radio flux density of both images is 167.12μJy and 22.33μJy with rms noise of 4.63μJy.

ULASJ0820+0812 was discovered by Jackson et al. (2009) in the MUSCLES survey. A single image was detected with a radio flux density of 71.33μJy and rms noise 6.13μJy which is large compared to a theoretical noise level of 4.4μJy. The map shows clear distortion from sidelobes from another source outside of the map as evidenced by the two streaks across the map this appears to have left ULASJ0820+0812 unaffected and thus the streaks are likely to be radio emission from the an external galaxy. Increasing the map size may decrease the noise level by ensuring the sidelobes causing the streaks is correctly cleaned this would likely decrease the high noise level issue.

J0941+0518 was discovered by Lemon et al. (2018b) and Williams et al. (2018). Both images were detected with a large image separation the flux density of images A and B is 119.34μJy and 61.09μJy respectively with an rms noise of 4.54μJy. Both images are far above the detection limit and the radio images match Gaia coordinates precisely confirming images are coincident with the lensed images (Gaia Collaboration et al., 2018).

SDSSJ0946+1835 was discovered by McGreer et al. (2010) using the SPIcam imager on the ARC 3.5m telescope later observations by Rusu et al. (2016) and More et al. (2016) revealed it to be a QSO. A single image was detected which is coincident with the i-band Pan-STARRS optical overlay, see figure 7.3, and had a measured radio flux density of 51.65μJy with rms noise 4.34μJy.

SDSSJ1128+2402 was discovered by Inada et al. (2014). Both images are likely detected confirmed from the the overlay and from the radio map which shows both the bright and faint optical source having clear radio detections coinciding but due to the small separation angle it is difficult to measure the flux density for the fainter image. Thus, under the assumption that both images were detected, the total radio flux density was measured to be 133.98μJy with an rms background noise of 4.34μJy. Running the casa task imfit returns a $\sim 20\mu Jy$ error in the crossover flux of the two images.

SDSSJ1131+1915 was discovered by Kayo et al. (2010). Only one image was detected with a radio flux density of 39.81μJy and 4.37μJy rms noise.

Source conclusions

Of the 14 radio detections two have originated from the lensing galaxy which gives the total dataset size as 12 sources with lensed RQQ image 6GHz radio detections. 50% of the sources have one image detection and 50% have two image detections. Two sources (J0203+1612 and SDSSJ0256+0153) were dropped from the list of detections (14$\rightarrow$12) since the radio detections belonged to the lensing galaxy. Therefore, from the 12 sources, all had their positions confirmed via the Pan-STARRS optical VLA radio contour overlays and with exact precision from Gaia. The noise level of all sources was roughly that expected ($\sim$4.2 to 5.0μ Jy) with only SDSSJ0820+0812 having a large noise level of 6.1μJy which upon searching for larger optical maps reveals multiple nearby galaxies from SDSS which are likely the cause of the contaminated streaks in the radio map and thus the result of the high noise level (Abolfathi et al., 2018), see figure 5.1.

Figure 5.1: Nearby galaxies approximately 12” away from the double image lens J0820+0812. Coordinates are RA and Declination degrees (Abolfathi et al., 2018).

5.2 Spectral Energy Distribution - SED

The SEDs are composed of any data available from Stacey et al. (2018) who observed four sources in this sample using Herschel-SPIRE using all three bands, SDSSJ0246-0825, SDSSJ0806+2006, SDSSJ0820+0812, and SDSS1131+1915. AKARI and IRAS upper limits (both of which were >99% sky surveys but with large rms noises, see subsection 4.4, meant my sources were not detected), and the VLA 6GHz radio data (though the radio data had no influence over the model fit). The model fit of the MIR/FIR data was created using equation 4.1 over an extended range of wavelengths 10μm to $10^4\mu$m. The other 8 sources are non-detections so a best fit was determined from fixing β and T at 1.5 and 38K respectively. For sources with both β and T fixed the FIR flux density calculated only varied as a function of the redshift z and the proportionality constant A see Equation 4.3 and 4.1 respectively.

For sources SDSSJ1128+2402, SDSSJ0806+2006, and J0941+0518, the radio band was split in two with the central frequencies at 5GHz and

7GHz each with a 2GHz bandwidth. Splitting the band in two was done by splitting the 32 spectral windows into two halves from 1-16 and 17-32. Splitting the spectral windows also halves the total bandwidth which raises the rms noise by a factor $\sqrt{2}$ (see equation 3.10). The radio band was only split for sources with a reasonable level of flux >100μJy and the spectral index was only measured for sources with with both the 5GHz and 7GHz radio maps measuring a 10σ detection. For sources that met these conditions a model was fit through the two radio data points to measure the spectral index of the radio emission which will be used later to compare the emission mechanism on the FIR-correlation with respect to what emission mechanism the spectral index indicates. The model used for spectral index was based on the relation $S_v \propto \nu^{\alpha}$ which can become an equality by adding a proportionality constant

$$S_v = A\nu^{\alpha}, \tag{5.1}$$

where S_v is the flux density, ν is the frequency, α is the spectral index, and A is a proportionality constant to be found.

The integrated FIR flux density for each source was then calculated from the best fit SED model using equation 4.1 over the FIR regime range 40-120μm. The derived FIR flux density was then inserted into equation 4.3 where the unmagnified luminosity was calculated. Both Q_{IR} and SFR, equation 4.4 and 4.6, were then calculated by converting the FIR luminosity to an IR luminosity with $L_{IR} = 1.91 \times L_{FIR}$. The calculated values from this dataset can be found in Table 5.1.

Though 8 sources have models with fixed β and T, a source having a detection either in the radio or FIR allows for an upper limit for the unknown flux density, SFR, and Q_{IR} which helps to constrain a possible radio emission mechanism in the RQQs by looking at the maximum Q_{IR} possible. For example, a source that is already above the FIR-correlation with a FIR upper limit implies the source emission mechanism is likely to be from AGN activity due to future FIR detections only taking the source

RQQ	β	T (K)	logμ $L_{FIR}(L_\odot)$	logμ SFR($M_\odot yr^{-1}$)	Q_{IR}	α
J0011-0845[b]	- -	38*	<12.81	<3.33	<2.93	N/A
J0146-1133[b]	- -	38*	<12.38	<2.90	<2.21	N/A
DESJ0245-0556[b]	- -	38*	<12.54	<3.06	<2.62	N/A
SDSSJ0246-0825[a]	- -	36.6	$12.62^{+0.04}_{-0.05}$	$3.14^{+0.05}_{-0.03}$	3.078	N/A
J0246-1845[b]	- -	38*	<13.07	<3.59	<2.77	N/A
SDSSJ0806+2006[a]	1.75	38*	$12.26^{+0.04}_{-0.05}$	$2.77^{+0.05}_{-0.04}$	2.24	N/A
SDSSJ0818+0601[b]	- -	38*	<13.51	<4.03	<2.57	-1.020$\pm$0.392
ULASJ0820+0812[a]	- -	35	$12.60^{+0.04}_{-0.05}$	$3.12^{+0.04}_{-0.04}$	2.17	N/A
J0941+0518[b]	- -	58	<12.54	<3.06	<2.06	-0.113$\pm$0.158
SDSSJ0946+1835[b]	- -	38*	<12.94	<3.46	<1.81	N/A
SDSSJ1128+2402[b]	- -	38*	<12.57	<3.09	<2.17	-0.726$\pm$0.200
SDSSJ1131+1915[b]	- -	22	<12.34	<2.86	<2.14	N/A

Table 5.1: Sources in dataset with a combination of detected FIR and Radio flux density[a] and no detected FIR flux density[b]. All but one source have $\beta = 1.5$ due to none of them having the minimum of four data points to maintain $dof > 1$ to plot for emissivity index and 10 sources have a fixed temperature of T=38K. SDSSJ0806+2006 has $\beta = 1.75$ to ensure no upper limits exist inside the model. FIR luminosity and SFR is uncorrected for magnification as indicated by μ. The flux calibrator error was taken as 10% for where at least one detection from Herschel-SPIRE was present. All errors shown are 1σ errors.

further from the correlation by determining a smaller FIR flux density. The minimum star formation rate in the sample is $\sim 588 \mathrm{M}_\odot \mathrm{yr}^{-1}$ and the maximum is $\sim 11,000 \mathrm{M}_\odot \mathrm{yr}^{-1}$ but the upper limits clearly imply these star formation rates are lower than calculated. The star formation rate, especially on the lower side for sources such as SDSSJ0806+2006 and SDSSJ1131+1915 already have star formation rates close to that which would be expected from AGN outflows (see subsection 1.3.1) therefore giving an AGN outflow luminosity of $L_{\mathrm{AGN}} \sim 10^{46} ergs^{-1}$.

5.3 Errors

5.3.1 radio FIR luminosity error

8/12 sources in this sample have a fixed temperature of 38K due to lack of any FIR data and so an upper limit of the flux was calculated and J0941+0518 has a fixed temperature of 58K because of the large redshift $z = 4.799$. A 10% calibrator error on the flux density was assumed combined with the rms noise level of the radio maps giving a flux error $\sigma_{S_\nu} = \sqrt{\sigma_{rms}^2 + (0.1 \times S_\nu)^2}$, where σ_{rms} is the radio map error and S_ν is the measured flux density. The error on luminosity distance and redshift was taken to be zero in the calculation of both the radio and FIR luminosity therefore only depending on the flux density resulting in small errors.

Star formation rate depends solely on $L_{IR} = 1.91 L_{\text{FIR}}$ meaning L_{IR} has the same error as the FIR luminosity.

5.3.2 Spectral index error

Errors for the spectral index were calculated from the percentage error on the split radio band

$$\sigma_\alpha = \sqrt{\frac{(\%S_{\text{5GHz}} + \%S_{\text{7GHz}})}{k}}, \tag{5.2}$$

where $\%S_{\text{5GHz}}$ and $\%S_{\text{7GHz}}$ are the percentage errors of the RMS map flux to the total measured flux in each band, and $k = ln\frac{\nu_{\text{5GHz}}}{\nu_{\text{7GHz}}}$.

5.3.3 Error improvements

It is obvious that MCMC (Markov chain Monte Carlo, see van Ravenzwaaij et al. (2016) for an introduction review to MCMC) could have been used to derive β or temperature for the three sources that had detected data

points available which would have given both more accurate derived parameters and slightly better errors other than those already presented. A Gaussian distribution of temperatures using the modified blackbody model (equation 4.1) would allow for better estimates of the error to be calculated as a range of temperatures and β would prove more statistically significant that the upper limit parameter values used in this thesis. MCMC or a Gaussian distribution could also be used for the radio spectral index calculations although this approach would benefit greatly from more radio data points which could be collected.

5.4 Far Infrared Correlation

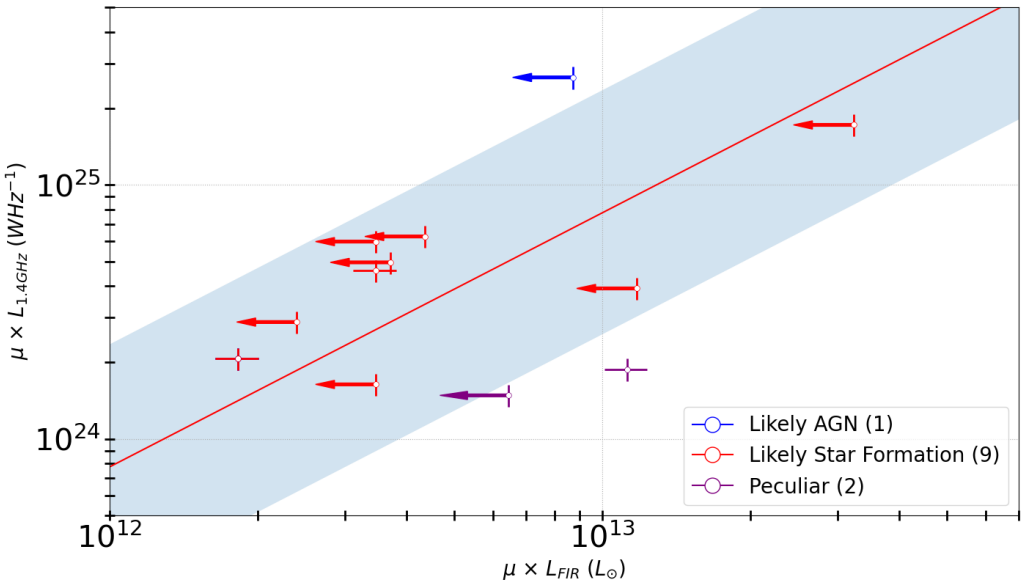

Figure 5.2: FIR-correlation plotted with a central red line $Q_{IR} = 2.40$ and a broad blue region displaying an error of 2σ where σ=0.24. Sources with blue arrows represent likely AGN sources of the radio emission with Q_{IR}<1.92, sources with red arrows and symbols represent star formation as the likely radio emission mechanism in the regime 1.92<Q_{IR}<2.88, and sources with purple arrows and symbols have Q_{IR}>2.88 which represents a strange position on the FIR-correlation which should not be possible.

FIR limits

Only 3 out of the 12 sources in the sample, shown in figure 5.2, have any FIR detection data available from which all came from Herschel-SPIRE therefore making it is hard to determine exactly where the other

9 sources belong on the FIR-correlation due to the imposed upper limits. The three sources, J0820+0812, SDSSJ0806+2006, and SDSSJ0246-0825 have FIR detections. The 7 sources within the blue FIR-correlation 2σ error strip, which is used to identify sources where radio emission from star formation is dominant, with FIR upper limits (as indicated by arrows) are likely star formation dominated in the radio as confirmed by the radio errors. However, the FIR limits indicate that four of the sources with $Q_{IR} < 2.40$ (above the red line) may exist outside of the 2σ strip which would source the dominant radio emission from an AGN. The three sources below the red Q_{IR} line are less likely to exist above the correlation but there is still a possibility if the measured FIR luminosity is measured to be incredibly small. SDSSJ0946+1835 is the only source with a $Q_{IR} < 1.92$ and has such has been classified as likely AGN as the source of the dominant amount of radio emission although within 3σ is classifed as radio dominated in by star formation. The statistical likelihood however that at 3σ SDSSJ0946+1835 is star formation dominated in the radio drops to ~ 0.3% assuming a normal distribution.

Thus, for the 12 sources in the dataset, 9 sources are identified as having the majority of radio emission from star formation, 1 source identified as likely AGN as the dominant radio source, and 2 sources being classified as peculiar though likely exist within the Q_{IR} strip or above as is evident their limits and from figure 5.2 within 3σ these 2 peculiar RQQ would be classified as star forming dominated. It would be ideal for FIR data to be collected for all sources in the sample with possible time on telescopes such as the JWST (James-Webb Space Telescope, 2021 launch) which operates at wavelengths up to 28.5μm which although not FIR can offer more data near the FIR regime providing better estimates for β and T for more accurate flux density calculations.

Peculiar sources

The peculiar sources given in figure 5.2 signify an unexplained lack of radio luminosity on the FIR-correlation or an excess of FIR emission.

However, if the condition for star formation is increased to 3σ such that Q_{IR} =1.68 to 3.12 then all peculiar sources would be identified as star forming which more reasonably explains the emission mechanism due to a FIR flux excess which is likely explained by dust obscuring the radio emission (Maddox et al., 2017).

5.5 FIR-correlation inaccuracy for RQQs?

For sources with large radio flux density values of >50μJy (ensuring image detections at a $\sim$ 10σ level) it would prove insightful to combine this work's radio results with different radio observational bands to measure a spectral index. It has been shown that an object's position in the L_{FIR} : L_{rad}, where L_{FIR} is the FIR luminosity and L_{rad} is the radio luminosity, with respect to the FIR-correlation (fig 5.2) should not be taken as the sole evidence for star formation dominated radio emission in RQQs as was shown for HS0810+2554 which suggests that AGN can operate as the dominant emission mechanism even with flux densities as low as 880nJy (Hartley et al., 2019).

The radio spectral index, α, tells us what physical process is emitting the radio radiation. A spectral index of α =-0.5 to -1.5 is expected for synchrotron radiation where relativistically accelerated electrons release energy through the constant acceleration of angular motion around a magnetic field (Peterson, 1997; Bradt, 2008). A spectral index of α =-0.1 is expected for free-free emission where electrons in ionised gas are scattered due to high kinetic energy where at low frequencies the ionised gas acts like a blackbody which is where the optical depth of the emitting region becomes τ $>>$ 1 and thus the spectral index becomes dependent on the opacity (Bradt, 2008; Burke & Graham-Smith, 2009). For spectral indexes α =0 to 2.0 star formation is the dominant source of radio emission due to the thermal heating of gas from stars (Bradt, 2008; Liddle & Loveday, 2009; Kellermann & Owen, 1988). The radio emission of PG1115+080 was measured, as inferred from the FIRC,

to be star formation dominated however the measurement of spectral index, $\alpha = -0.65 \pm 0.38$, indicates the actual dominant source of radio emission is from small scale AGN activity (Hartley et al., 2021). The disagreement between the FIR-correlation and spectral index gave Hartley et al. (2021) reason for calculating the maximum possible radio emission from star formation which showed a 1-10% total contribution meaning the other 90-99% must come from a dusty AGN torus hence confirming the measurement of the radio spectral index gave the correct radio emission mechanism in PG1115+080 (Chiba et al., 2005). From Hartley et al. (2021), the question must be raised as to how many sources in this sample are actually star forming despite lying on Q_{IR} = $2.40 \pm$ 0.24. It has been shown multiple times (Hartley et al., 2019, 2021) that the actual dominant radio emission mechanism of some sources lying in the FIRC is from AGN synchrotron radiation. Usually the assumption is that RQQs lying within the FIRC are star forming and thus have the dominant amount of radio radiation generated by star formation synchrotron radiation but spectral index measurements and VLBI obvservations have shown this to not always be the case. To confirm this discrepancy, the three brightest sources in the sample had their frequency band split in two for a measurement of the radio spectral index which was used to compare the implied radio emission as compared to that from the FIRC.

SDSSJ0818+0812 has a measured Q_{IR} of 2.57 which puts this RQQ comfortably inside the FIR correlation which allows us to assume star formation is the dominant radio emission mechanism. However, the FIR upper limit indicates this source may actually exist to the left of the correlation because of a radio excess and as such could possibly be dominated by AGN radio emission if the FIR flux is measured to be low enough. The measured spectral index of α =-1.02± 0.392 supports this hypothesis as the radio spectral index provides evidence for AGN synchrotron radiation. A similar case for **SDSSJ1128+2402** is present in the disagreement between a Q_{IR} of 2.17 and a measured radio spectral index of α =-0.726± 0.200 which again indicates this RQQ likely has

synchrotron radiation as the dominant emission mechanism providing evidence of potential flaws in the FIR-correlation which states that all objects within in the FIR-correlation must be star forming which has been shown to not be true (Hartley et al., 2021).

For both **SDSSJ1128+2402** and **SDSSJ0818+0812**, it would be worth collecting a larger range of radio flux densities at different observation bands to confirm the spectral index. Obtaining more FIR observation data to populate the SEDs would also allow for model fits with free β and T which would also remove the upper limit FIR flux measurement providing sources with more confident placements on the FIR-correlation. Assuming the conclusions obtained in this thesis for these two sources are true then it would be interesting to observe the small scale structure about the RQQ core using VLBI to confirm whether a similar radio flux density obtained for this thesis with the VLA is measured on the scale of a few parsecs to confirm the AGN synchrotron activity. AGN synchrotron emission can also be deduced from a measurement of the brightness temperature where starburst activity correlates to $\sim 10^{4-5}$K (Condon et al., 1991; Condon, 1992; Muxlow et al., 1994) and thus any source where $T_B > 10^5$K is very likely producing the radio emission directly from sub-pc AGN jets (Hartley et al., 2019). Observation of sub-pc AGN jets would be required for the observations of AGN jets.

The measurement of the central RQQ engine could possibly highlight a difference in the flux density from the AGN synchrotron component and the total RQQ flux density which would provide clear evidence for the coexistence of two different emission mechanisms fuelling the same RQQ (that being AGN and star formation). RQQ **J0941+0518** should also have follow up observations over a range of different radio frequencies as the source is within error of having a spectral index indicative of star formation, thermal free-free and potentially synchrotron as an upper limit. More observations of J0941+0518 would provide more accurate measurements and smaller errors which could provide good reason for follow up observations with VLBI. With a confirmation of disagreement

between the FIR-correlation and radio spectral index measurements across multiple sources the model of jetted and non-jetted RQQ Padovani (2017) could be proved to either be wrong or the theory could be adapted to incorporate the cohabitation of the two emission mechanisms (AGN synchrotron and star formation).

See table 5.2 for a complete list of the likely dominant radio emission mechanism for each detected source in the sample.

RQQ	Q_{IR}	SI (α)	Radio Emission Mechanism
J0011-0845	<2.93	N/A	FIR limit - likely SF
J0146-1133	<2.21	N/A	FIR limit - likely SF
DESJ0245-0556	<2.62	N/A	FIR limit - likely SF
SDSSJ0246-0825	3.08	N/A	likely SF
J0246-1845	<2.77	N/A	FIR limit - likely SF
SDSSJ0806+2006	2.24	N/A	likely SF
SDSSJ0818+0601	<2.57	-1.02$\pm$0.4	FIRC SF. SI AGN synchrotron.
ULASJ0820+0812	2.17	N/A	likely SF
J0941+0518	<2.06	-0.11$\pm$0.16	FIRC SF. SI AGN free-free emission.
SDSSJ0946+1835	<1.81	N/A	FIR limit - likely AGN
SDSSJ1128+2402	<2.17	-0.73$\pm$0.20	FIRC SF. SI AGN synchrotron.
SDSSJ1131+1915	<2.14	N/A	FIR limit - SF

Table 5.2: Star formation (SF). The calculated Q_{IR} of each source in the sample and the SI (spectral index) for sources where the band was split. The likely dominant emission mechanism from the FIRC is presented paired with the likely dominant emission mechanism from the spectral index. Sources with interesting results (i.e. conflicting emission mechanisms) have been discussed earlier in the results section. The likely emission mechanisms are based on the jetted and non-jetting model by Padovani (2017) but as discussed this is not always definitive. The sources with conflicting radio emission mechanisms may have a possible combination of the two mechanisms. Sources in the SI column with ”N/A” did not have their spectral index calculated due to the flux density not being $> 10\sigma$ detections upon splitting for 5 and 7GHz.

6 Conclusions

This thesis has presented the C band VLA radio observations of 22 doubly lensed RQQs with the aim to investigate the dominant radio emission mechanism of each detected RQQ by measuring the Q_{IR} and then designating a radio emission mechanism. The Q_{IR} is a strip of confidence for galaxies whereby we assume galaxies that lie within the region $Q_{IR} = 2.40 \pm 0.24$ are dominated in the radio band by star formation processes whereas those above the confidence strip are dominated by radio synchrotron from AGN jets. This thesis also presents only half the total sample of doubly lensed RQQs as part of a collaboration with Dr Shruti Badole with which we have a combined dataset making for the largest investigation of the radio emission mechanism in doubly lensed RQQs ever performed. The mechanisms for AGN dominated radio emission is where $Q_{IR} < 1.92$ and star formation dominated radio emission for $2.88 > Q_{IR} > 1.92$ where $Q_{IR} = 2.40 \pm 0.24$ Ivison et al. (2010). Out of the 22 RQQ observations 12 sources have a radio detection at $> 4\sigma_{rms}$. For these 12 sources, FIR data was available for four with one source only having full Herschel-SPIRE upper limits. Both AKARI and IRAS MIR/FIR upper limit data was available to help constrain a maximum FIR flux. The 12 radio detections are confirmed to be from the background RQQs with confirmation from both the radio-optical Pan-STARRS1 overlays and coordinate comparisons with Gaia (Chambers et al., 2016; Gaia Collaboration et al., 2018)

The arrangement of the VLA telescopes was non-ideal for the sub-arcsecond observations of the RQQ lensed images (figure 4.1) and there was a lack of MIR/FIR data available with 9 sources having FIR upper limits. From the 12 sources in the sample only ULASJ0820+0812, SDDSJ0806+2006, and J0246-0825 have both Herschel-SPIRE rest-frame FIR and VLA C band radio detections with the rest of the sample either having FIR upper limit data from AKARI and IRAS (IRa, 1988; Kawada et al., 2007). Using the limits as a guide, 9 sources are within the 2σ scatter

region around $Q_{IR} = 2.40 \pm 0.24$ to assume dominant star formation as the main source of radio emission whereas one sources exists above the 2σ region hinting heavily at a central AGN engine powered mechanism as the main source of their radio emission. Two sources had a Q_{IR} >2σ error above $Q_{IR} = 2.40 \pm 0.24$ which shows a measure of excess FIR flux compared to the radio compared to sources lying within the correlation. From the sample, assuming all FIR excess sources lie within Q_{IR} and therefore have star formation dominated radio emission, 11/12 of the RQQs in this sample have likely star formation as their dominant radio emission mechanism and 1 source likely has a central synchrotron AGN engine as the main radio emission mechanism. Therefore, from the FIRC the 12 lensed RQQs have had a determined dominant radio emission mechanism up to a 2σ confidence level from the $Q_{IR} = 2.40$ according to the FIR limits and radio detections. The source J0941+0518 is above the 2σ scatter region around the Q_{IR} (see figure 5.2) which is worth having a VLBI follow up observation to confirm the likely small scale thermal free-free emission as indicated by the radio spectral index measurement of $\alpha = -0.11$. It would also be worth observing the three sources (see figure 5.2) that have a disagreement of dominant radio emission mechanism according to the Q_{IR} and radio spectral index. Hartley et al. (2021) has cautioned that sources that lie on the FIRC, which is consistent with star formation, is to be taken with a pinch of salt as radio spectral index calculations by Hartley et al. (2021) and those calculated in this thesis have shown emissivity of the radio can be inconsistent with the expected spectral index values for sources that lie within the FIRC. Sources with inconsistencies should have follow up observations with VLBI to confirm there is indeed something wrong with the FIRC in relation to radio quiet quasars or a bimodal model is outdated and should be scrapped for a model that incorporates a varying mixture of emission mechanisms.

References

Abolfathi B., et al., 2018, The Fourteenth Data Release of the Sloan Digital Sky Survey: First Spectroscopic Data from the Extended Baryon Oscillation Spectroscopic Survey and from the Second Phase of the Apache Point Observatory Galactic Evolution Experiment. Vol. 235, (arXiv:1707.09322), doi:10.3847/1538-4365/aa9e8a

Acosta-Pulido J. A., et al., 2015, The Spanish Square Kilometre Array White Book. (arXiv:1506.03474)

Agnello A., Grillo C., Jones T., Treu T., Bonamigo M., Suyu S. H., 2018a, MNRAS, 474, 3391

Agnello A., et al., 2018b, Quasar lenses and pairs in the VST-ATLAS and Gaia. Vol. 475, (arXiv:1711.07492), doi:10.1093/mnras/stx3226

Agnello A., et al., 2018c, DES meets Gaia: discovery of strongly lensed quasars from a multiplet search. Vol. 479, (arXiv:1711.03971), doi:10.1093/mnras/sty1419

Alsing P. M., 1998, The optical-mechanical analogy for stationary metrics in general relativity. Vol. 66, doi:10.1119/1.18957,

Anderson J. A., 1920, The Michelson Interferometer Method for Measuring Close Double Stars. Vol. 32, doi:10.1086/122929,

Antonucci R., 1993, Unified models for active galactic nuclei and quasars.. Vol. 31, doi:10.1146/annurev.aa.31.090193.002353,

Antonucci R. R. J., Miller J. S., 1985, Spectropolarimetry and the nature of NGC 1068.. Vol. 297, doi:10.1086/163559,

Armitage P. J., Natarajan P., 2002, Accretion during the Merger of Supermassive Black Holes. Vol. 567, (arXiv:astro-ph/0201318), doi:10.1086/339770

Atek H., et al., 2015, NEW CONSTRAINTS ON THE FAINT END OF THE UV LUMINOSITY FUNCTION ATz 7-8 USING THE GRAVITATIONAL LENSING OF THE HUBBLE FRONTIER FIELDS CLUSTER A2744. Vol. 800, American Astronomical Society, doi:10.1088/0004-637x/800/1/18, http://dx.doi.org/10.1088/0004-637X/800/1/18

Badole S., Jackson N., Hartley P., Sluse D., Stacey H., Vives-Arias H., 2020, VLA and ALMA observations of the lensed radio-quiet quasar SDSS J0924+0219: a molecular structure in a 3 μJy radio source. Vol. 496,

Oxford University Press (OUP), doi:10.1093/mnras/staa1488, http://dx.doi.org/10.1093/mnras/staa1488

Bandara K., Crampton D., Simard L., 2009, A RELATIONSHIP BETWEEN SUPERMASSIVE BLACK HOLE MASS AND THE TOTAL GRAVITATIONAL MASS OF THE HOST GALAXY. Vol. 704, American Astronomical Society, doi:10.1088/0004-637x/704/2/1135, http://dx.doi.org/10.1088/0004-637X/704/2/1135

Barkana R., Loeb A., 2000, High-Redshift Galaxies: Their Predicted Size and Surface Brightness Distributions and Their Gravitational Lensing Probability. Vol. 531, American Astronomical Society, doi:10.1086/308503, https://doi.org/10.1086/308503

Bartelmann M., 2010, Gravitational lensing. Vol. 27, IOP Publishing, doi:10.1088/0264-9381/27/23/233001, http://dx.doi.org/10.1088/0264-9381/27/23/233001

Begelman M. C., Blandford R. D., Rees M. J., , Theory of extragalactic radio sources, doi:10.1103/RevModPhys.56.255. , https://www.osti.gov/biblio/6663580

Begelman M. C., Volonteri M., Rees M. J., 2006, Formation of supermassive black holes by direct collapse in pre-galactic haloes. Vol. 370, (https://academic.oup.com/mnras/article-pdf/370/1/289/3406434/mnras0370-0289.pdf), doi:10.1111/j.1365-2966.2006.10467.x, https://doi.org/10.1111/j.1365-2966.2006.10467.x

Bell E. F., 2003, Estimating Star Formation Rates from Infrared and Radio Luminosities: The Origin of the Radio-Infrared Correlation. Vol. 586, (arXiv:astro-ph/0212121), doi:10.1086/367829

Benson A. J., 2010, Galaxy formation theory. Vol. 495, Elsevier BV, doi:10.1016/j.physrep.2010.06.001, http://dx.doi.org/10.1016/j.physrep.2010.06.001

Blandford R. D., Narayan R., 1992, Cosmological applications of gravitational lensing.. Vol. 30, doi:10.1146/annurev.astro.30.1.311,

Blundell K. M., Beasley A. J., 1998, The central engines of radio-quiet quasars. Vol. 299, Oxford University Press (OUP), doi:10.1046/j.1365-8711.1998.01752.x, http://dx.doi.org/10.1046/j.1365-8711.1998.01752.x

Blundell K. M., Kuncic Z., 2007, On the Origin of Radio Core Emission in Radio-quiet Quasars. Vol. 668, American Astronomical Society, doi:10.1086/522695, http://dx.doi.org/10.1086/522695

Bonvin V., et al., 2016, H0LiCOW – V. New COSMOGRAIL time delays of HE 0435−1223: H0 to 3.8percent precision from strong lensing in a flat ΛCDM model. Vol. 465, (https://academic.oup.com/mnras/article-pdf/465/4/4914/10254866/stw3006.pdf), doi:10.1093/mnras/stw3006, https://doi.org/10.1093/mnras/stw3006

Bradt H., 2008, Astrophysics Processes

Briggs D. S., Schwab F. R., Sramek R. A., 1999, in Taylor G. B., Carilli C. L., Perley R. A., eds, Astronomical Society of the Pacific Conference Series Vol. 180, Synthesis Imaging in Radio Astronomy II. p. 127

Browne I. W. A., Wilkinson P. N., Patnaik A. R., Wrobel J. M., 1998, Interferometer phase calibration sources - II. The region 0 deg<=delta_B1950<=+20 deg. Vol. 293, doi:10.1046/j.1365-8711.1998.01072.x,

Burbidge G. R., Burbidge E. M., Sandage A. R., 1963, Evidence for the Occurrence of Violent Events in the Nuclei of Galaxies. Vol. 35, doi:10.1103/RevModPhys.35.947,

Burke B. F., Graham-Smith F., 2009, An Introduction to Radio Astronomy

CASA 2021, CASA6.1.2 VLA pipeline, https://casaguides.nrao.edu/index.php?title=VLA_CASA_Pipeline-CASA6.1.2

CASAdocs 2021, TCLEAN, https://casadocs.readthedocs.io/en/stable/api/tt/casatasks.imaging.tclean.html#description

Cambridge d., 2021, Lensed RQQs, https://research.ast.cam.ac.uk/lensedquasars/

Caplar N., Lilly S. J., Trakhtenbrot B., 2018, AGN Evolution from the Galaxy Evolution Viewpoint. II.. Vol. 867, American Astronomical Society, doi:10.3847/1538-4357/aae691, https://doi.org/10.3847/1538-4357/aae691

Chambers K. C., et al., 2016, The Pan-STARRS1 Surveys. (arXiv:1612.05560)

Chen B., Kantowski R., Dai X., 2015, A SIMPLE GRAVITATIONAL LENS MODEL FOR COSMIC VOIDS. Vol. 804, American Astronomical Society, doi:10.1088/0004-637x/804/2/130, http://dx.doi.org/10.1088/0004-637X/804/2/130

Chiba M., Minezaki T., Kashikawa N., Kataza H., Inoue K. T., 2005, Subaru Mid-Infrared Imaging of the Quadruple Lenses PG 1115+080 and B1422+231: Limits on Substructure Lensing. Vol. 627, (arXiv:astro-ph/0503487), doi:10.1086/430403

Chwolson O., 1924, Über eine mögliche Form fiktiver Doppelsterne. Vol. 221, doi:10.1002/asna.19242212003,

Cochrane R. K., et al., 2021, Resolving a dusty, star-forming SHiZELS galaxy at z = 2.2 with HST, ALMA, and SINFONI on kiloparsec scales. Vol. 503, (https://academic.oup.com/mnras/article-pdf/503/2/2622/36742667/stab467.pdf), doi:10.1093/mnras/stab467, https://doi.org/10.1093/mnras/stab467

Combes F., 2017, AGN Feedback and Its Quenching Efficiency. Vol. 4, doi:10.3389/fspas.2017.00010, , https://www.frontiersin.org/article/10.3389/fspas.2017.00010

Condon J. J., 1992, Radio emission from normal galaxies.. Vol. 30, doi:10.1146/annurev.aa.30.090192.003043,

Condon J. J., Huang Z. P., Yin Q. F., Thuan T. X., 1991, Compact Starbursts in Ultraluminous Infrared Galaxies. Vol. 378, doi:10.1086/170407,

Conway R. G., Kellermann K. I., Long R. J., 1963, The radio frequency spectra of discrete radio sources. Vol. 125, doi:10.1093/mnras/125.3.261,

Crane P. C., Napier P. J., 1989, in Perley R. A., Schwab F. R., Bridle A. H., eds, Astronomical Society of the Pacific Conference Series Vol. 6, Synthesis Imaging in Radio Astronomy. p. 139

Croton D. J., et al., 2006, The many lives of active galactic nuclei: cooling flows, black holes and the luminosities and colours of galaxies. Vol. 365, (arXiv:astro-ph/0508046), doi:10.1111/j.1365-2966.2005.09675.x

Dale D. A., Helou G., Contursi A., Silbermann N. A., Kolhatkar S., 2001, The Infrared Spectral Energy Distribution of Normal Star-forming Galaxies. Vol. 549, doi:10.1086/319077,

Denneau L., et al., 2013, The Pan-STARRS Moving Object Processing System. Vol. 125, IOP Publishing, doi:10.1086/670337, https://doi.org/10.1086/670337

Di Matteo T., Springel V., Hernquist L., 2005, Energy input from quasars regulates the growth and activity of black holes and their host galaxies. Vol. 433, (arXiv:astro-ph/0502199), doi:10.1038/nature03335

Doherty L. H., MacLeod J. M., Purton C. R., 1968, Flux Densities of Radio Sources at a Wavelength of 2.8 cm.. Vol. 73

Doi Y., et al., 2015, The AKARI far-infrared all-sky survey maps. Vol. 67, (https://academic.oup.com/pasj/article-pdf/67/3/50/11276030/psv022.pdf), doi:10.1093/pasj/psv022, https://doi.org/10.1093/pasj/psv022

Einstein A., 1919, Relativity : the Special the General Theory, 100th anniversary edition. edn. Princeton University Press, Princeton

Einstein A., 1936, Lens-Like Action of a Star by the Deviation of Light in the Gravitational Field. Vol. 84, doi:10.1126/science.84.2188.506,

Ellis R., 2010, Gravitational lensing: A unique probe of dark matter and dark energy. Vol. 368, doi:10.1098/rsta.2009.0209,

Fabian A. C., Celotti A., Erlund M. C., 2006, Radiative pressure feedback by a quasar in a galactic bulge. Vol. 373, (arXiv:astro-ph/0608425), doi:10.1111/j.1745-3933.2006.00234.x

Fan J. H., Peng Q. S., Tao J., Qian B. C., Shen Z. Q., Liu Y., 2009, in Wang W., Yang Z., Luo Z., Chen Z., eds, Astronomical Society of the Pacific Conference Series Vol. 408, The Starburst-AGN Connection. p. 306

Fanti C., Fanti R., de Ruiter H. R., Parma P., 1986, VLA observations of low luminosity radio galaxies. III. The A-array observations. Vol. 65

Frittelli S., Kling T., Newman E., 2002, Fermat potentials for nonperturbative gravitational lensing. Vol. 65, doi:10.1103/PhysRevD.65.123007,

Gaia Collaboration et al., 2018, Gaia Data Release 2. Summary of the contents and survey properties. Vol. 616, (arXiv:1804.09365), doi:10.1051/0004-6361/201833051

Gallimore J. F., Baum S. A., O'Dea C. P., 1996, The Subarcsecond Radio Structure in NGC 1068. II. Implications for the Central Engine and Unifying Schemes. Vol. 464, doi:10.1086/177311,

Gallimore J. F., Baum S. A., O'Dea C. P., 2004, The Parsec-Scale Radio Structure of NGC 1068 and the Nature of the Nuclear Radio Source. Vol. 613, American Astronomical Society, doi:10.1086/423167, http://dx.doi.org/10.1086/423167

Goldschmidt P., Kukula M. J., Miller L., Dunlop J. S., 1999, A Comparison of the Optical Properties of Radio-loud and Radio-quiet Quasars. Vol. 511, American Astronomical Society, doi:10.1086/306699, https://doi.org/10.1086/306699

Greenstein J. L., Schmidt M., 1964, The Quasi-Stellar Radio Sources 3C 48 and 3C 273.. Vol. 140, doi:10.1086/147889,

Griffin M. J., et al., 2010, The Herschel-SPIRE instrument and its in-flight performance. Vol. 518, (arXiv:1005.5123), doi:10.1051/0004-6361/201014519

Guedel M., Benz A. O., 1993, X-Ray/Microwave Relation of Different Types of Active Stars. Vol. 405, doi:10.1086/186766,

Hartley P., Jackson N., Sluse D., Stacey H. R., Vives-Arias H., 2019, Strong lensing reveals jets in a sub-microJy radio-quiet quasar. Vol. 485, (arXiv:1901.05791), doi:10.1093/mnras/stz510

Hartley P., Jackson N., Badole S., McKean J. P., Sluse D., Vives-Arias H., 2021, Using strong lensing to understand the microJy radio emission in two radio quiet quasars at redshift 1.7. (arXiv:2109.10720)

Heckman T. M., Best P. N., 2014, The Coevolution of Galaxies and Supermassive Black Holes: Insights from Surveys of the Contemporary Universe. Vol. 52, Annual Reviews, doi:10.1146/annurev-astro-081913-035722, http://dx.doi.org/10.1146/annurev-astro-081913-035722

Heckman T. M., Kauffmann G., 2006, The host galaxies of AGN in the Sloan Digital Sky Survey. Vol. 50, doi:10.1016/j.newar.2006.06.022,

Helou G., Khan I. R., Malek L., Boehmer L., 1988, IRAS Observations of Galaxies in the Virgo Cluster Area. Vol. 68, doi:10.1086/191285,

Hessels J., 2013, The Techniques of Radio Interferometry I: Basics

Hogbom J. A., 1974, Aperture Synthesis with a Non-Regular Distribution of Interferometer Baselines. Vol. 15

Hogg D. W., 1999, Distance measures in cosmology. (arXiv:astro-ph/9905116)

Hopkins P. F., Hernquist L., Cox T. J., Kereš D., 2008, A Cosmological Framework for the Co-Evolution of Quasars, Supermassive Black Holes, and Elliptical Galaxies. I. Galaxy Mergers and Quasar Activity. Vol. 175, (arXiv:0706.1243), doi:10.1086/524362

Hutsemékers D., Sluse D., Kumar P., 2020, Spatially separated continuum sources revealed by microlensing in the gravitationally lensed broad absorption line quasar SDSS J081830.46+060138.0. Vol. 633, (arXiv:1912.04336), doi:10.1051/0004-6361/201936973

1988, Infrared Astronomical Satellite (IRAS) Catalogs and Atlases.Volume 1: Explanatory Supplement. Vol. 1

Inada N., et al., 2005, SDSS J024634.11-082536.2: A New Gravitationally Lensed Quasar from the Sloan Digital Sky Survey. Vol. 130, (arXiv:astro-ph/0506631), doi:10.1086/432930

Inada N., et al., 2006, SDSS J0806+2006 and SDSS J1353+1138: Two New Gravitationally Lensed Quasars from the Sloan Digital Sky Survey. Vol. 131, (arXiv:astro-ph/0512239), doi:10.1086/500591

Inada N., et al., 2010, The Sloan Digital Sky Survey Quasar Lens Search. IV. Statistical Lens Sample from the Fifth Data Release. Vol. 140, (arXiv:1005.5570), doi:10.1088/0004-6256/140/2/403

Inada N., Oguri M., Rusu C. E., Kayo I., Morokuma T., 2014, Discovery of Four Doubly Imaged Quasar Lenses from the Sloan Digital Sky Survey. Vol. 147, (arXiv:1401.2274), doi:10.1088/0004-6256/147/6/153

Ivison R. J., et al., 2010, Herschel and SCUBA-2 imaging and spectroscopy of a bright, lensed submillimetre galaxy at z = 2.3. Vol. 518, (arXiv:1005.1071), doi:10.1051/0004-6361/201014548

Jackson N., 2008, Principles of Interferometry. p. 193

Jackson N., 2013, Bulletin of the Astronomical Society of India

Jackson N., 2015, Living Reviews in Relativity

Jackson N., Ofek E. O., Oguri M., 2009, A new gravitational lens from the MUSCLES survey: ULASJ082016.1+081216. Vol. 398, (arXiv:0906.2647), doi:10.1111/j.1365-2966.2009.15198.x

Jaki S. L., 1978, Johann Georg von Soldner and the gravitational bending of light, with an English translation of his essay on it published in 1801. Vol. 8, doi:10.1007/bf00715064,

Jiang L., Fan X., Ivezić Ž., Richards G. T., Schneider D. P., Strauss M. A., Kelly B. C., 2007, The Radio-Loud Fraction of Quasars is a Strong Function of Redshift and Optical Luminosity. Vol. 656, American Astronomical Society, doi:10.1086/510831, https://doi.org/10.1086/510831

Joint Iras Science W. G., 1994, VizieR Online Data Catalog: IRAS catalogue of Point Sources, Version 2.0 (IPAC 1986)

Jones C., Stern C., Falco E., Forman W., David L., Shapiro I., Fabian A. C., 1993, Discovery of a New Component in the Gravitationally Lensed Quasar 0957+561. Vol. 410, doi:10.1086/172720,

Jovanović P., Popović L. Č., 2009, X-ray Emission From Accretion Disks of AGN: Signatures of Supermassive Black Holes. (arXiv:0903.0978)

Kaiser N., Squires G., 1993, Mapping the Dark Matter with Weak Gravitational Lensing. Vol. 404, doi:10.1086/172297,

Kalfountzou E., Jarvis M. J., Bonfield D. G., Hardcastle M. J., 2012, Star formation in high-redshift quasars: excess [O ii] emission in the radio-loud population. Vol. 427, (https://academic.oup.com/mnras/article-pdf/427/3/2401/3852432/427-3-2401.pdf), doi:10.1111/j.1365-2966.2012.22093.x, https://doi.org/10.1111/j.1365-2966.2012.22093.x

Kawada M., et al., 2007, The Far-Infrared Surveyor (FIS) for AKARI*. Vol. 59, (https://academic.oup.com/pasj/article-pdf/59/sp2/S389/17451342/pasj59-S389.pdf), doi:10.1093/pasj/59.sp2.S389, https://doi.org/10.1093/pasj/59.sp2.S389

Kayo I., Inada N., Oguri M., Morokuma T., Hall P. B., Kochanek C. S., Schneider D. P., 2010, Eight New Quasar Lenses from the Sloan Digital Sky Survey Quasar Lens Search. Vol. 139, (arXiv:0912.1462), doi:10.1088/0004-6256/139/4/1614

Kayser R., Refsdal S., 1983, The difference in light travel time between gravitational lens images. I. Generalization of the wavefront method to arbitrary deflectors and inhomogeneous universes.. Vol. 128

Kellermann K. I., 2013, The discovery of quasars. Vol. 41, (arXiv:1304.3627)

Kellermann K. I., Owen F. N., 1988, Radio galaxies and quasars.. pp 563–602

Kellermann K. I., Thompson A. R., 1988, The Very-Long-Baseline Array. Vol. 258, doi:10.1038/scientificamerican0188-54,

Kellermann K. I., Sramek R., Schmidt M., Shaffer D. B., Green R., 1989, VLA Observations of Objects in the Palomar Bright Quasar Survey. Vol. 98, doi:10.1086/115207,

Kellermann K. I., Condon J. J., Kimball A. E., Perley R. A., Ivezić Ž., 2016, Radio-loud and Radio-quiet QSOs. Vol. 831, (arXiv:1608.04586), doi:10.3847/0004-637X/831/2/168

Kennicutt Robert C. J., 1998, The Global Schmidt Law in Star-forming Galaxies. Vol. 498, (arXiv:astro-ph/9712213), doi:10.1086/305588

Kochanek C. S., 2004, in 33rd Advanced Saas Fee Course on Gravitational Lensing: Strong, Weak, and Micro. (arXiv:astro-ph/0407232)

Kochanek C. S., Keeton C. R., McLeod B. A., 2001, The Importance of Einstein Rings. Vol. 547, (arXiv:astro-ph/0006116), doi:10.1086/318350

Krone-Martins A., et al., 2019, Gaia GraL: Gaia DR2 Gravitational Lens Systems. V. Doubly-imaged QSOs discovered from entropy and wavelets

Laor A., Behar E., 2008, On the origin of radio emission in radio-quiet quasars. Vol. 390, Oxford University Press (OUP), doi:10.1111/j.1365-2966.2008.13806.x, http://dx.doi.org/10.1111/j.1365-2966.2008.13806.x

Leipski C., Falcke H., Bennert N., Hüttemeister S., 2006, The radio structure of radio-quiet quasars. Vol. 455, EDP Sciences, doi:10.1051/0004-6361:20054311, http://dx.doi.org/10.1051/0004-6361:20054311

Lemon C. A., Auger M. W., McMahon R. G., Ostrovski F., 2018b, Gravitationally lensed quasars in Gaia - II. Discovery of 24 lensed quasars. Vol. 479, (arXiv:1803.07601), doi:10.1093/mnras/sty911

Lemon C. A., Auger M. W., McMahon R. G., Ostrovski F., 2018a, Gravitationally lensed quasars in Gaia – II. Discovery of 24 lensed quasars. Vol. 479, (https://academic.oup.com/mnras/article-pdf/479/4/5060/25716214/sty911.pdf), doi:10.1093/mnras/sty911, https://doi.org/10.1093/mnras/sty911

Lemon C. A., Auger M. W., McMahon R. G., 2019, Gravitationally lensed quasars in Gaia - III. 22 new lensed quasars from Gaia data release 2. Vol. 483, (arXiv:1810.04480), doi:10.1093/mnras/sty3366

Lemon C., et al., 2020, The STRong lensing Insights into the Dark Energy Survey (STRIDES) 2017/2018 follow-up campaign: discovery of 10 lensed quasars and 10 quasar pairs. Vol. 494, (arXiv:1912.09133), doi:10.1093/mnras/staa652

Liddle A., Loveday J., 2009, The Oxford Companion to Cosmology

Lima M., Jain B., Devlin M., 2010, Lensing magnification: implications for counts of submillimetre galaxies and SZ clusters. Vol. 406, Oxford University Press (OUP), doi:10.1111/j.1365-2966.2010.16884.x, http://dx.doi.org/10.1111/j.1365-2966.2010.16884.x

Lyke B. W., et al., 2020, The Sloan Digital Sky Survey Quasar Catalog: Sixteenth Data Release. Vol. 250, American Astronomical Society, doi:10.3847/1538-4365/aba623, http://dx.doi.org/10.3847/1538-4365/aba623

Lynden-Bell D., 1969, Galactic Nuclei as Collapsed Old Quasars. Vol. 223, doi:10.1038/223690a0,

Maddox N., et al., 2017, Far-infrared emission in luminous quasars accompanied by nuclear outflows. Vol. 470, (https://academic.oup.com/mnras/article-pdf/470/2/2314/18158376/stx1416.pdf), doi:10.1093/mnras/stx1416, https://doi.org/10.1093/mnras/stx1416

Magorrian J., et al., 1998, The Demography of Massive Dark Objects in Galaxy Centers. Vol. 115, (arXiv:astro-ph/9708072), doi:10.1086/300353

Massey R., Kitching T., Richard J., 2010, The dark matter of gravitational lensing. Vol. 73, (arXiv:1001.1739), doi:10.1088/0034-4885/73/8/086901

McGreer I. D., et al., 2010, SDSS J094604.90+183541.8: A Gravitationally Lensed Quasar at z = 4.8. Vol. 140, (arXiv:1002.3832), doi:10.1088/0004-6256/140/2/370

McKee C. F., Ostriker E. C., 2007, Theory of Star Formation. Vol. 45, (arXiv:0707.3514), doi:10.1146/annurev.astro.45.051806.110602

Milani A., Knezevic Z., Farnocchia D., Bernardi F., Jedicke R., Denneau L., PS1 Science Collaboration 2012, Identification of Known Objects in Solar System Surveys. Vol. 1667

Miller L., Peacock J. A., Mead A. R. G., 1990, The bimodal radio luminosity function of quasars.. Vol. 244

Mo H., van den Bosch F. C., White S., 2010, Galaxy Formation and Evolution

Moe M., Arav N., Bautista M. A., Korista K. T., 2009, Quasar Outflow Contribution to AGN Feedback: Observations of QSO SDSS J0838+2955. Vol. 706, (arXiv:0911.3332), doi:10.1088/0004-637X/706/1/525

Moorsel G. V., 2021, List of VLA Calibrators, https://science.nrao.edu/facilities/vla/observing/callist

More A., et al., 2016, The SDSS-III BOSS quasar lens survey: discovery of 13 gravitationally lensed quasars. Vol. 456, (arXiv:1509.07917), doi:10.1093/mnras/stv2813

Muxlow T. W. B., Pedlar A., Wilkinson P. N., Axon D. J., Sanders E. M., de Bruyn A. G., 1994, The structure of young supernova remnants in M82. Vol. 266, (https://academic.oup.com/mnras/article-pdf/266/2/455/3100070/mnras266-0455.pdf), doi:10.1093/mnras/266.2.455, https://doi.org/10.1093/mnras/266.2.455

NRAO 2021, VLA Configurations, https://science.nrao.edu/facilities/vla/docs/manuals/oss/performance/resolution

Nagamine K., Barai P., Proga D., 2012, in Chartas G., Hamann F., Leighly K. M., eds, Astronomical Society of the Pacific Conference Series Vol. 460, AGN Winds in Charleston. p. 245 (arXiv:1112.3525)

Narayan R., Bartelmann M., 1996, Lectures on Gravitational Lensing. (arXiv:astro-ph/9606001)

Narayan R., Wallington S., 1992, Introduction to basic concepts of gravitational lensing. Springer Berlin Heidelberg, Berlin, Heidelberg

Neugebauer G., et al., 1984, The Infrared Astronomical Satellite (IRAS) mission.. Vol. 278, doi:10.1086/184209,

Neupert W. M., 1968, Comparison of Solar X-Ray Line Emission with Microwave Emission during Flares. Vol. 153, doi:10.1086/180220,

Newton I., 1704, Opticks. Great minds series, Prometheus, Amherst, N.Y

Nims J., Quataert E., Faucher-Giguère C.-A., 2015, Observational signatures of galactic winds powered by active galactic nuclei. Vol. 447, Oxford University Press (OUP), doi:10.1093/mnras/stu2648, http://dx.doi.org/10.1093/mnras/stu2648

Numpy 2021, Python numpy package, https://numpy.org

Padovani P., 2017, On the two main classes of active galactic nuclei. Vol. 1, (arXiv:1707.08069), doi:10.1038/s41550-017-0194

Panessa F., Baldi R. D., Laor A., Padovani P., Behar E., McHardy I., 2019, The origin of radio emission from radio-quiet active galactic nuclei. Vol. 3, (arXiv:1902.05917), doi:10.1038/s41550-019-0765-4

Paraficz D., et al., 2018, ALMA view of RX J1131-1231: Sub-kpc CO (2-1) mapping of a molecular disk in a lensed star-forming quasar host galaxy. Vol. 613, (arXiv:1705.09931), doi:10.1051/0004-6361/201731250

Peebles P. J. E., 1993, Principles of Physical Cosmology

Peterson B. M., 1997, An Introduction to Active Galactic Nuclei

Pilbratt G. L., et al., 2010, Herschel Space Observatory. An ESA facility for far-infrared and submillimetre astronomy. Vol. 518, (arXiv:1005.5331), doi:10.1051/0004-6361/201014759

Planck Collaboration et al., 2016, Planck 2015 results. XIII. Cosmological parameters. Vol. 594, (arXiv:1502.01589), doi:10.1051/0004-6361/201525830

Rees M. J., 1978, Relativistic jets and beams in radio galaxies. Vol. 275, doi:10.1038/275516a0,

Rees M. J., 1984, Black Hole Models for Active Galactic Nuclei. Vol. 22, doi:10.1146/annurev.aa.22.090184.002351,

Refsdal S., 1964, MNRAS, 128, 307

Refsdal S., 1966, On the possibility of testing cosmological theories from the gravitational lens effect. Vol. 132, doi:10.1093/mnras/132.1.101,

Retana-Montenegro, E. Röttgering, H. J. A. 2017, Probing the radio loud/quiet AGN dichotomy with quasar clustering. Vol. 600, doi:10.1051/0004-6361/201526433, , https://doi.org/10.1051/0004-6361/201526433

Rhee G., 1991, An estimate of the Hubble constant from the gravitational lensing of quasar Q0957 561. Vol. 350, doi:10.1038/350211a0, , https://www.nature.com/articles/350211a0

Roberts D. H., Lehár J., Hewrtt J. N., Burke B. F., 1991, The Hubble constant from VLA measurement of the time delay in the double quasar 0957 561. Vol. 352, doi:10.1038/352043a0, , https://www.nature.com/articles/352043a0?proof=t

Roussel H., Sauvage M., Vigroux L., Bosma A., 2001, The relationship between star formation rates and mid-infrared emission in galactic disks. Vol. 372, (arXiv:astro-ph/0104088), doi:10.1051/0004-6361:20010498

Rusu C. E., et al., 2016, Subaru Telescope adaptive optics observations of gravitationally lensed quasars in the Sloan Digital Sky Survey. Vol. 458, (arXiv:1506.05147), doi:10.1093/mnras/stw092

Rusu C. E., et al., 2017, MNRAS, 467, 4220

Salpeter E. E., 1955, The Luminosity Function and Stellar Evolution.. Vol. 121, doi:10.1086/145971,

Sauer T., 2021, Soldner, Einstein, Gravitational Light Deflection and Factors of Two. Vol. 533, doi:10.1002/andp.202100203,

Sauvage M., Thuan T. X., 1992, On the Use of Far-Infrared Luminosity as a Star Formation Indicator in Galaxies. Vol. 396, doi:10.1086/186519,

Schild R. E., Thomson D. J., 1997, The Q0957+561 time Delay, quasar structure, and Microlensing, doi:10.1007/978-94-015-8941-3_7. , https://link.springer.com/chapter/10.1007/978-94-015-8941-3_7

Schmidt M., 1963, 3C 273 : A Star-Like Object with Large Red-Shift. Vol. 197, doi:10.1038/1971040a0,

Schneider P., Ehlers J., Falco E. E., 1992, Gravitational Lenses, doi:10.1007/978-3-662-03758-4.

Scipy 2021, Python scipy package, https://www.scipy.org

Segransan D., 2003, in Perrin G., Malbet F., eds, EAS Publications Series Vol. 6, EAS Publications Series. p. 69, doi:10.1051/eas:2003006

Seyfert C. K., 1935, Magnitudes of Bright Galaxies in the Coma-Virgo Group.. Vol. 403

Silk J., 2005, Ultraluminous starbursts from supermassive black hole-induced outflows. Vol. 364, (arXiv:astro-ph/0509149), doi:10.1111/j.1365-2966.2005.09672.x

Smith M. G., Wright A. E., 1980, A radio study of optically selected QSOs.. Vol. 191, doi:10.1093/mnras/191.4.871,

Somerville R. S., Hopkins P. F., Cox T. J., Robertson B. E., Hernquist L., 2008, A semi-analytic model for the co-evolution of galaxies, black holes and active galactic nuclei. Vol. 391, (arXiv:0808.1227), doi:10.1111/j.1365-2966.2008.13805.x

Springel V., Di Matteo T., Hernquist L., 2005, Modelling feedback from stars and black holes in galaxy mergers. Vol. 361, (arXiv:astro-ph/0411108), doi:10.1111/j.1365-2966.2005.09238.x

Stacey H. R., et al., 2018, Gravitational lensing reveals extreme dust-obscured star formation in quasar host galaxies. Vol. 476, Oxford University Press (OUP), doi:10.1093/mnras/sty458, http://dx.doi.org/10.1093/mnras/sty458

Strittmatter P. A., Hill P., Pauliny-Toth I. I. K., Steppe H., Witzel A., 1980, Radio observations of optically selected quasars. Vol. 88

Suyu S. H., et al., 2012, ApJ, 750

Taylor Carilli C. L. P. R. A., 1999, Synthesis Imaging in Radio Astronomy II

Thompson W. J., 1992, Fourier series and the Gibbs phenomenon. pp 425–429, doi:10.1119/1.16895

Thompson A. R., 1999, in Taylor G. B., Carilli C. L., Perley R. A., eds, Astronomical Society of the Pacific Conference Series Vol. 180, Synthesis Imaging in Radio Astronomy II. p. 11

Thompson A., Moran J., Swenson G., 2017, Van Cittert–Zernike Theorem, Spatial Coherence, and Scattering. pp 767–786, doi:10.1007/978-3-319-44431-4_15

Tonry J., Davis M., 1979, A survey of galaxy redshifts. I. Data reduction techniques.. Vol. 84, doi:10.1086/112569,

Tremonti C. A., Moustakas J., Diamond-Stanic A. M., 2007, The Discovery of 1000 km s^{-1} Outflows in Massive Poststarburst Galaxies at z=0.6. Vol. 663, (arXiv:0706.0527), doi:10.1086/520083

Tsupko O. Y., Bisnovatyi-Kogan G. S., Rogers A., Er X., 2020, An examination of geometrical and potential time delays in gravitational lensing. Vol. 37, IOP Publishing, doi:10.1088/1361-6382/abae86, http://dx.doi.org/10.1088/1361-6382/abae86

Ulvestad J. S., Antonucci R. R. J., Barvainis R., 2005, VLBA Imaging of Central Engines in Radio-Quiet Quasars. Vol. 621, American Astronomical Society, doi:10.1086/427426, https://doi.org/10.1086/427426

1972, New Mexico site selected for proposed radio astronomy facility. Vol. 53, doi:10.1029/EO053i005p00579,

2016, Calibrating flux density scale, https://science.nrao.edu/facilities/vla/docs/manuals/oss/performance/fdscale

Walsh D., Carswell R. F., Weymann R. J., 1979, Nature, 279, 381

Wambsganss J., 1998, Living Reviews in Relativity, 1, 12

Wandel A., 1999, in Gaskell C. M., Brandt W. N., Dietrich M., Dultzin-Hacyan D., Eracleous M., eds, Astronomical Society of the Pacific Conference Series Vol. 175, Structure and Kinematics of Quasar Broad Line Regions. p. 213 (arXiv:astro-ph/9808171)

Wang C.-Y., 2017, Essential radio astronomy, by James J. Condon and Scott M. Ransom. pp 278–279, doi:10.1080/00107514.2017.1312538

Weedman D. W., 1986, Quasar astronomy

Werner M. C., 2012, Gravitational lensing in the Kerr-Randers optical geometry. Vol. 44, Springer Science and Business Media LLC, doi:10.1007/s10714-012-1458-9, http://dx.doi.org/10.1007/s10714-012-1458-9

Williams P. R., et al., 2018, Discovery of three strongly lensed quasars in the Sloan Digital Sky Survey. Vol. 477, (arXiv:1706.01506), doi:10.1093/mnrasl/sly043

Yang J., et al., 2016, A Survey of Luminous High-redshift Quasars with SDSS and WISE. II. the Bright End of the Quasar Luminosity Function at z $\approx$ 5. Vol. 829, (arXiv:1607.04415), doi:10.3847/0004-637X/829/1/33

Young P., Gunn J. E., Kristian J., Oke J. B., Westphal J. A., 1980, The double quasar Q0957+561 A, B: a gravitational lens image formed by a galaxy at z=0.39.. Vol. 241, doi:10.1086/158365,

Yuan T.-T., Kewley L. J., Swinbank A. M., Richard J., 2012, THE A2667 GIANT ARC ATz= 1.03: EVIDENCE FOR LARGE-SCALE SHOCKS AT HIGH REDSHIFT. Vol. 759, doi:10.1088/0004-637x/759/1/66,

Zakamska N. L., et al., 2015, Star formation in quasar hosts and the origin of radio emission in radio-quiet quasars. Vol. 455, Oxford University Press (OUP), doi:10.1093/mnras/stv2571, http://dx.doi.org/10.1093/mnras/stv2571

Zernike F., 1938, The concept of degree of coherence and its application to optical problems. Vol. 5, doi:10.1016/S0031-8914(38)80203-2,

Zhao C., Blair D. G., 2017, First direct detection of gravitational waves . Vol. 4, (https://academic.oup.com/nsr/article-pdf/4/5/681/31566724/nwx089.pdf), doi:10.1093/nsr/nwx089, https://doi.org/10.1093/nsr/nwx089

Zheng W., et al., 2012, A magnified young galaxy from about 500 million years after the Big Bang. Vol. 489, doi:10.1038/nature11446, , www.nature.com/articles/nature11446

Zwicky F., 1937, Physical Review, 51, 290

de Jong T., Klein U., Wielebinski R., Wunderlich E., 1985, Radio continuum and far-infrared emission from spiral galaxies : a close correlation.. Vol. 147

nrao 2021, Casa setjy task, https://casa.nrao.edu/casadocs/latest/global-task-list/task_setjy/about

van Cittert P. H., 1934, Die Wahrscheinliche Schwingungsverteilung in Einer von Einer Lichtquelle Direkt Oder Mittels Einer Linse Beleuchteten Ebene. Vol. 1, doi:10.1016/S0031-8914(34)90026-4,

van Haarlem M. P., et al., 2013, LOFAR: The LOw-Frequency ARray. Vol. 556, (arXiv:1305.3550), doi:10.1051/0004-6361/201220873

van Ravenzwaaij D., Cassey P., Brown S., 2016, A simple introduction to Markov Chain Monte–Carlo sampling. Vol. 25, doi:10.3758/s13423-016-1015-8,

7 Appendix

Table 7.1: Summary of key observed properties of the radio detection lensed RQQ. Φ_E is the Einstein radius in arcseconds, Sep is the angular separation between images in arcseconds, and μ is the source magnification. J0820+0812, SDSSJ1128+2404, and SDSSJ1131+1915 latest information available from Rusu et al. (2017); Inada et al. (2010).

Source	Φ_E(")	z_{source}	z_{lens}	Sep.(")	μ	Discovery
J0011-0845	$0.96^{0.97}_{0.95}$	1.70	- -	1.92	$5.0^{5.3}_{4.5}$	(Lemon et al., 2018a)
J0146-1133	$0.83^{0.84}_{0.82}$	1.44	- -	- -	$3.9^{4.0}_{3.8}$	(Agnello et al., 2018b)
J0203+1612	$1.36^{1.40}_{1.34}$	2.18	0.488	2.73	$7.0^{7.8}_{6.5}$	(Lemon et al., 2019)
DESJ0245-0556	$0.90^{0.92}_{0.89}$	1.54	- -	- -	$3.15^{3.24}_{3.09}$	(Agnello et al., 2018c)
SDSSJ0246-0825	0.553	1.689	0.723	1.10	13.9	(Inada et al., 2005)
J0246-1845	$0.49^{0.50}_{0.48}$	1.86	- -	- -	$4.61^{4.78}_{4.50}$	(Lemon et al., 2020)
SDSSJ0256+0153	1.03	2.60	0.603	1.93	- -	(More et al., 2016)
SDSSJ0806+2006	0.68	1.54	0.573	1.41	4.63	(Inada et al., 2006)
SDSSJ0818+0601	- -	2.381	$\geq$1	1.10	- -	(More et al., 2016)
ULASJ0820+0812	- -	2.024	0.803	2.30	$5.35^{5.74}_{4.44}$	(Jackson et al., 2009)
J0941+0518	$2.72^{2.73}_{2.67}$	1.54	0.34	5.40	$5.2^{5.3}_{5.1}$	(Lemon et al., 2018b)
SDSSJ0946+1835	- -	4.799	0.388	3.10	$3.2^{3.22}_{3.16}$	(McGreer et al., 2010)
SDSSJ1128+2402	0.42	1.608	- -	0.75	6.0	(Inada et al., 2014)
SDSSJ1131+1915	$0.680^{0.686}_{0.674}$	2.915	0.3	1.46	$6.90^{6.59}_{8.3}$	(Kayo et al., 2010)

Table 7.2: An example observing block. Initial phase calibrators observations are calculated before moving to target source where there is a 2 second window between target and phase calibrator to ensure calibrations are not made irrelevant. Observation block made at the request of Dr Neal Jackson. Observation block from the 30th November 2020, total observation time was 5172 seconds, for VLA telescope configuration see 4.1. In this observation block the phase calibrator is shared between target sources because of the close proximity of both target sources.

Timerange (UTC)	scan	Field name	Classification
10:03:50.0-10:06:44.0	1	J0825+0309	Phase cal
10:06:46.0-10:07:14.0	2	J0825+0309	Phase cal
10:07:16.0-10:12:14.0	3	J0825+0309	Phase cal
10:12:16.0-10:14:14.0	4	J0825+0309	Phase cal
10:14:16.0-10:19:12.0	5	SDSSJ0818+0601	Target source
10:19:14.0-10:21:12.0	6	J0825+0309	Phase cal
10:21:14.0-10:26:12.0	7	SDSSJ0818+0601	Target source
10:26:14.0-10:28:12.0	8	J0825+0309	Phase cal
10:28:14.0-10:33:10.0	9	SDSSJ0818+0601	Target source
10:33:12.0-10:35:10.0	10	J0825+0309	Phase cal
10:35:12.0-10:40:10.0	11	SDSSJ0818+0601	Target source
10:40:12.0-10:42:10.0	12	J0825+0309	Phase cal
10:42:12.0-10:47:08.0	13	SDSSJ0818+0601	Target source
10:47:10.0-10:49:08.0	14	J0825+0309	Phase cal
10:49:10.0-10:51:08.0	15	J0825+0309	Phase cal
10:51:10.0-10:56:06.0	16	ULASJ0820+0812	Target source
10:56:08.0-10:58:06.0	17	J0825+0309	Phase cal
10:58:08.0-11:03:06.0	18	ULASJ0820+0812	Target source
11:03:08.0-11:05:06.0	19	J0825+0309	Phase cal
11:05:08.0-11:10:04.0	20	ULASJ0820+0812	Target source
11:10:06.0-11:12:04.0	21	J0825+0309	Phase cal
11:12:06.0-11:17:04.0	22	ULASJ0820+0812	Target source
11:17:06.0-11:19:04.0	23	J0825+0309	Phase cal
11:19:04.0-11:24:02.0	24	ULASJ0820+0812	Target source
11:24:04.0-11:26:02.0	25	J0825+0309	Phase cal
11:26:04.0-11:30:02.0	26	J0521+1638	flux density cal

Figure 7.1: Source SEDs with either a radio or FIR detection/limit. FIR flux was calculated between 40 and 120μm and in the case of full IR/FIR limits a FIR flux upper limit was calculated.

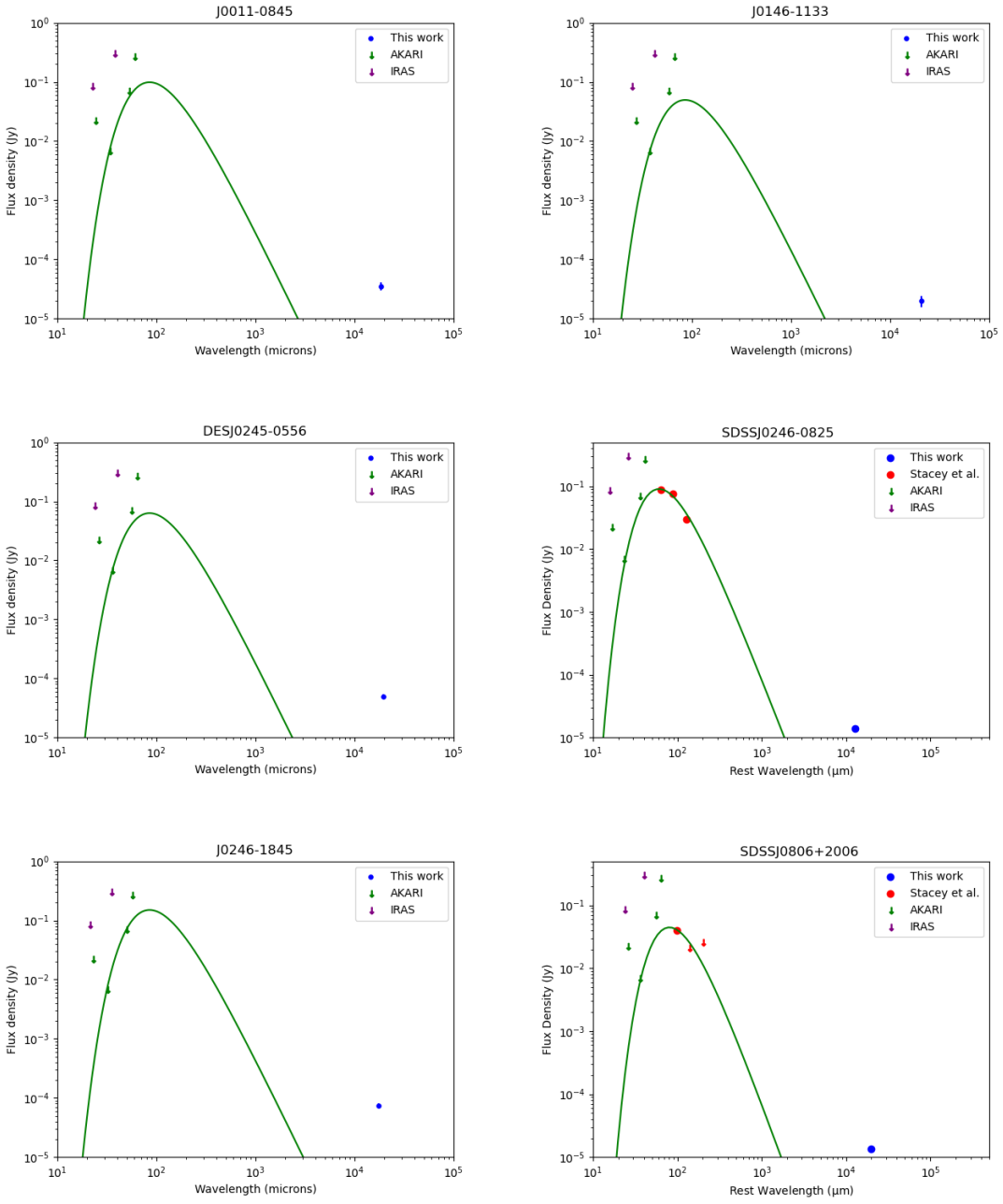

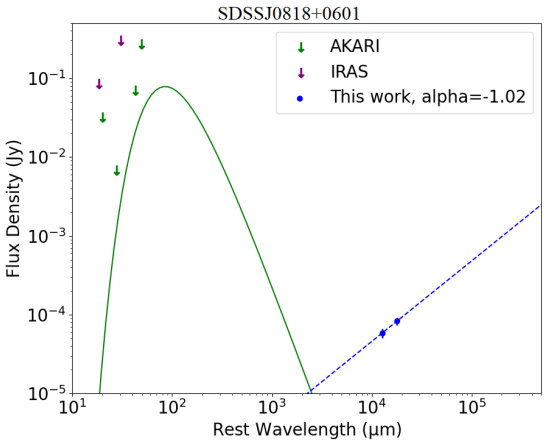
SDSSJ0818+0601
AKARI
IRAS
This work, alpha=-1.02
Flux Density (Jy)
Rest Wavelength (μm)

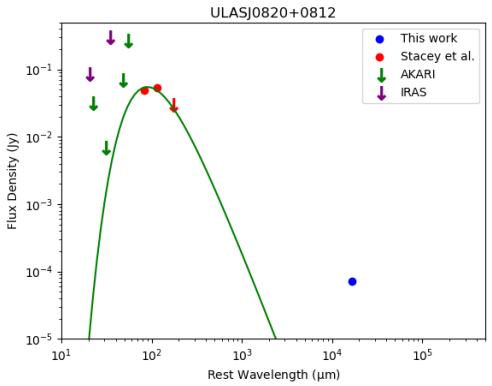
ULASJ0820+0812
This work
Stacey et al.
AKARI
IRAS
Flux Density (Jy)
Rest Wavelength (μm)

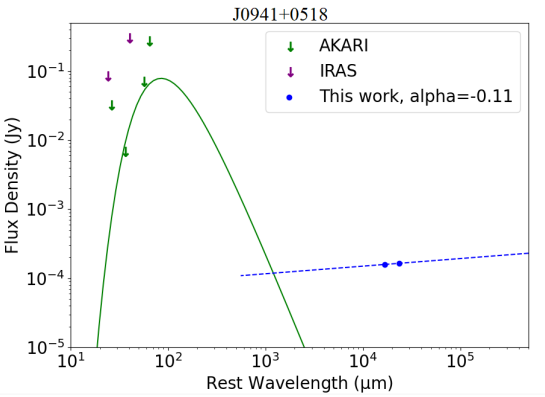
J0941+0518
AKARI
IRAS
This work, alpha=-0.11
Flux Density (Jy)
Rest Wavelength (μm)

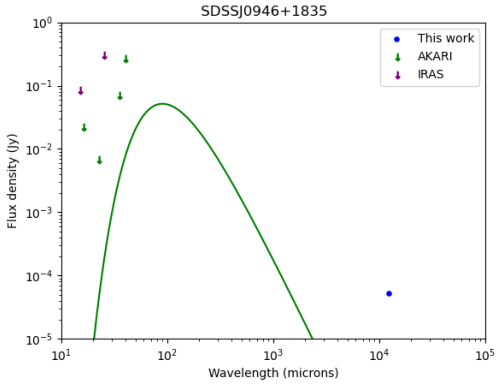
SDSSJ0946+1835
This work
AKARI
IRAS
Flux density (Jy)
Wavelength (microns)

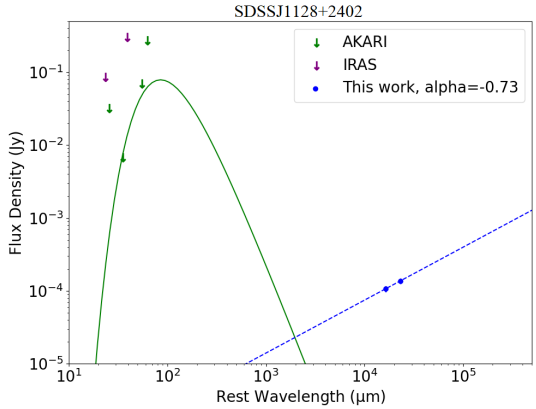
SDSSJ1128+2402
AKARI
IRAS
This work, alpha=-0.73
Flux Density (Jy)
Rest Wavelength (μm)

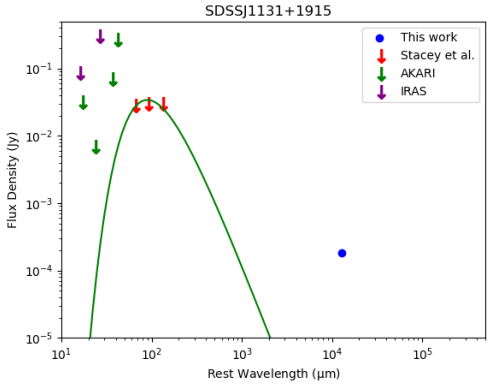
SDSSJ1131+1915
This work
Stacey et al.
AKARI
IRAS
Flux Density (Jy)
Rest Wavelength (μm)

Figure 7.2: 6GHz VLA radio maps with imsize = [128] and cell = [’0.1arcsec’]. Images used natural weighting during CLEAN and niter = 300.

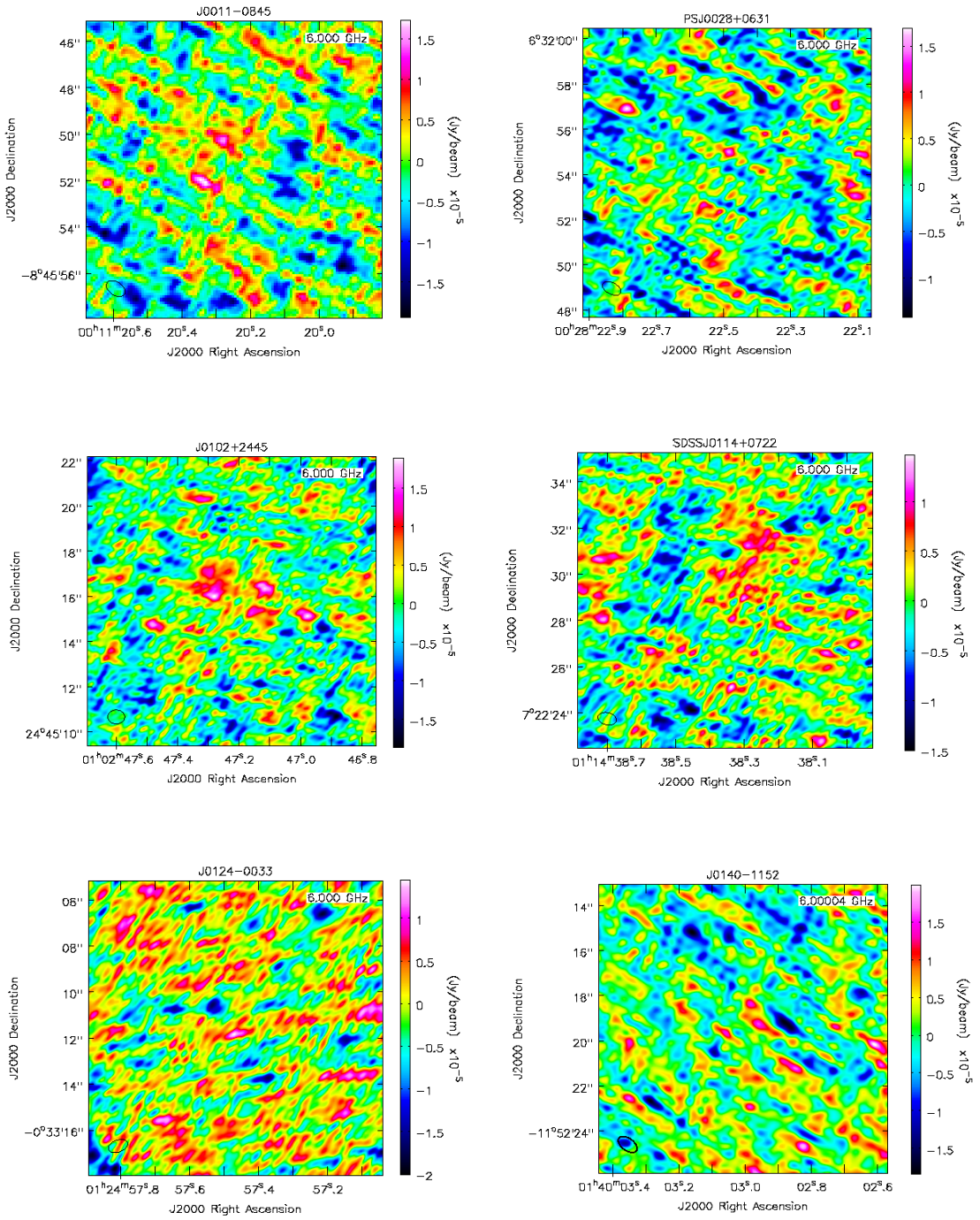

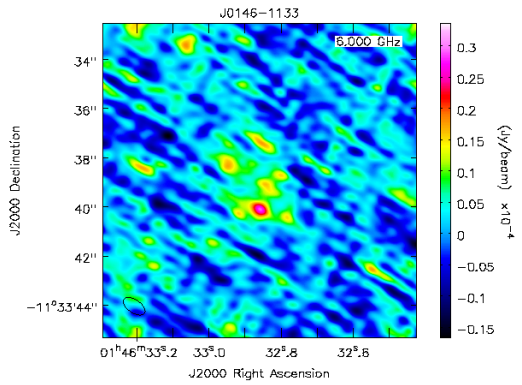
J0146−1133
6.000 GHz
J2000 Declination
34''
36''
38''
40''
42''
−11°33'44''
01h46m33s.2
33s.0
32s.8
32s.6
J2000 Right Ascension
0.3
0.25
0.2
0.15
0.1
0.05
0
−0.05
−0.1
−0.15
(Jy/beam) ×10−4

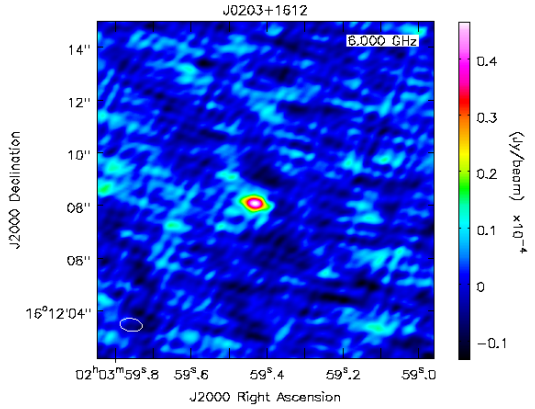
J0203+1612
6.000 GHz
J2000 Declination
14''
12''
10''
08''
06''
16°12'04''
02h03m59s.8
59s.6
59s.4
59s.2
59s.0
J2000 Right Ascension
0.4
0.3
0.2
0.1
0
−0.1
(Jy/beam) ×10−4

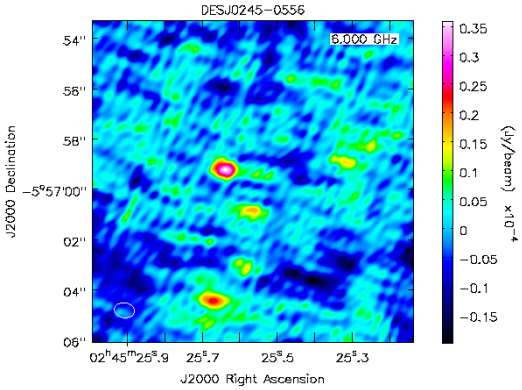
DESJ0245−0556
6.000 GHz
J2000 Declination
54''
56''
58''
−5°57'00''
02''
04''
06''
02h45m25s.9
25s.7
25s.5
25s.3
J2000 Right Ascension
0.35
0.3
0.25
0.2
0.15
0.1
0.05
0
−0.05
−0.1
−0.15
(Jy/beam) ×10−4

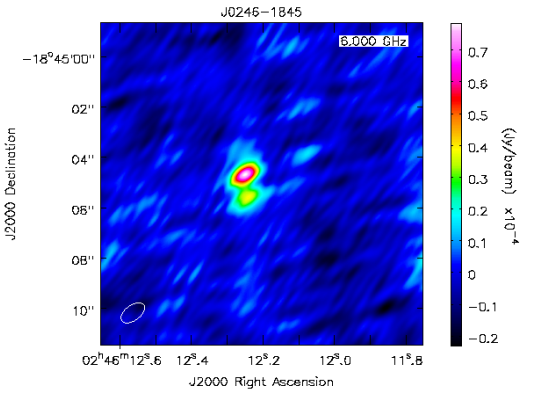
J0246−1845
6.000 GHz
J2000 Declination
−18°45'00''
02''
04''
06''
08''
10''
02h46m12s.6
12s.4
12s.2
12s.0
11s.8
J2000 Right Ascension
0.7
0.6
0.5
0.4
0.3
0.2
0.1
0
−0.1
−0.2
(Jy/beam) ×10−4

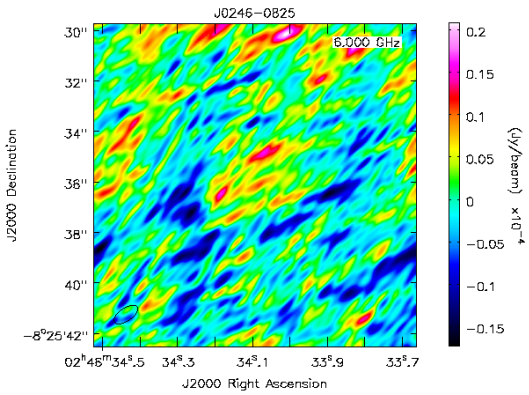
J0246−0825
6.000 GHz
J2000 Declination
30''
32''
34''
36''
38''
40''
−8°25'42''
02h46m34s.5
34s.3
34s.1
33s.9
33s.7
J2000 Right Ascension
0.2
0.15
0.1
0.05
0
−0.05
−0.1
−0.15
(Jy/beam) ×10−4

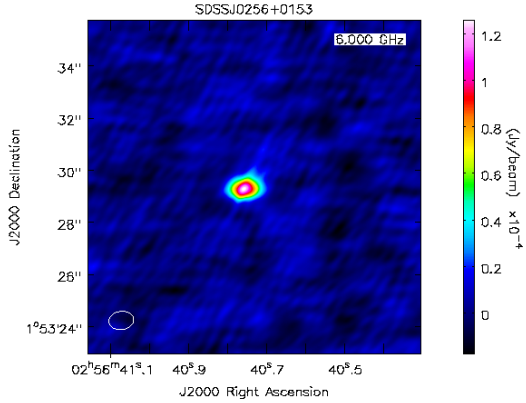
SDSSJ0256+0153
6.000 GHz
J2000 Declination
34''
32''
30''
28''
26''
1°53'24''
02h56m41s.1
40s.9
40s.7
40s.5
J2000 Right Ascension
1.2
1
0.8
0.6
0.4
0.2
0
(Jy/beam) ×10−4

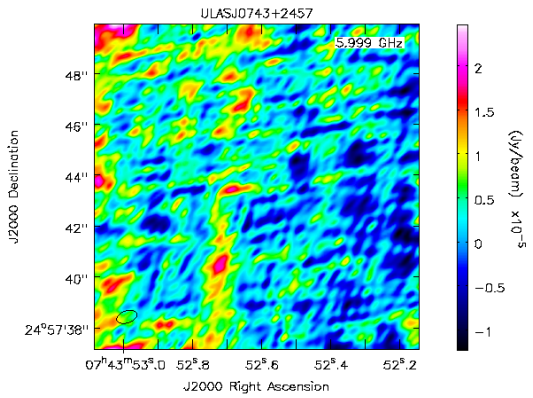
ULASJ0743+2457
5.999 GHz
J2000 Declination
J2000 Right Ascension
(Jy/beam) x10⁻⁵

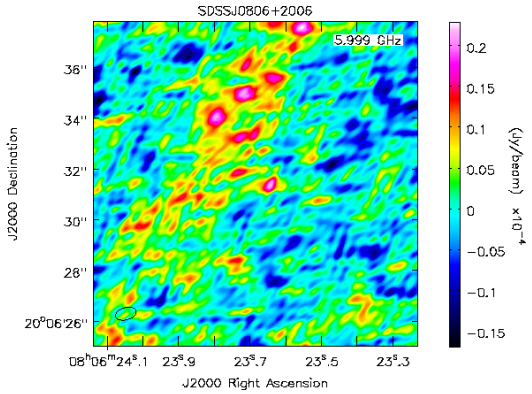
SDSSJ0806+2006
5.999 GHz
J2000 Declination
J2000 Right Ascension
(Jy/beam) x10⁻⁴

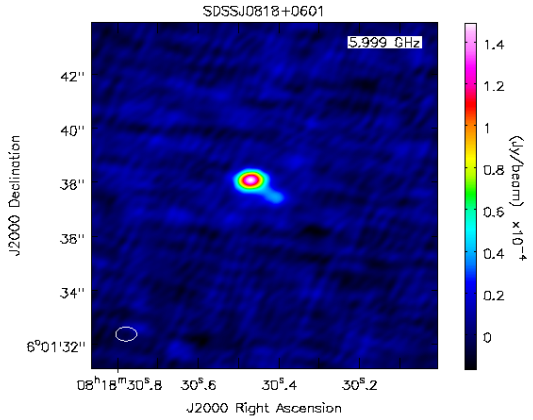
SDSSJ0818+0601
5.999 GHz
J2000 Declination
J2000 Right Ascension
(Jy/beam) x10⁻⁴

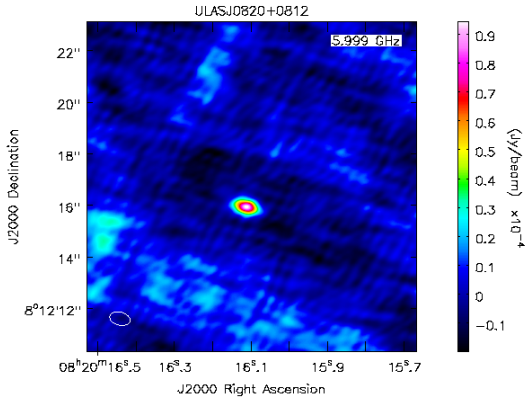
ULASJ0820+0812
5.999 GHz
J2000 Declination
J2000 Right Ascension
(Jy/beam) x10⁻⁴

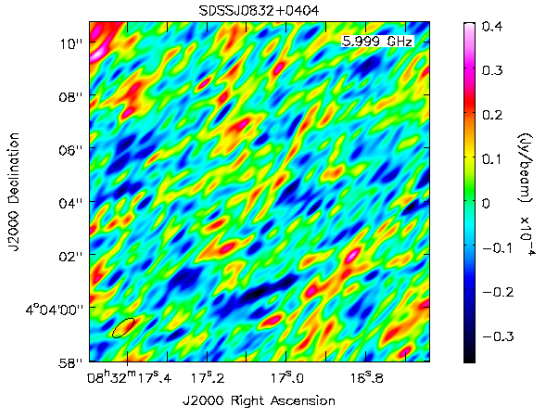
SDSSJ0832+0404
5.999 GHz
J2000 Declination
J2000 Right Ascension
(Jy/beam) x10⁻⁴

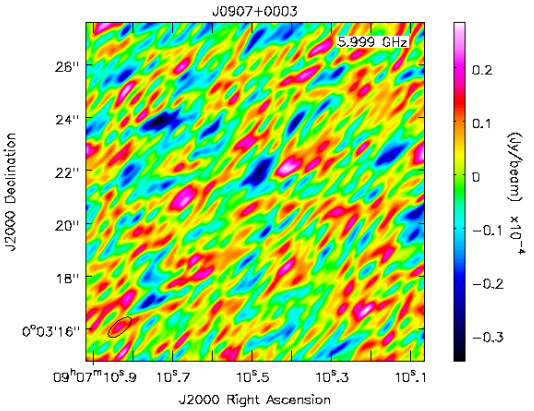
J0907+0003
5.999 GHz
J2000 Declination
J2000 Right Ascension
(Jy/beam) x10⁻⁴

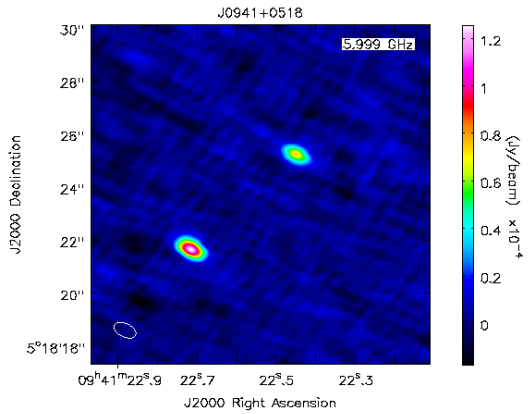
J0941+0518
5.999 GHz
J2000 Declination
J2000 Right Ascension
(Jy/beam) ×10⁻⁴

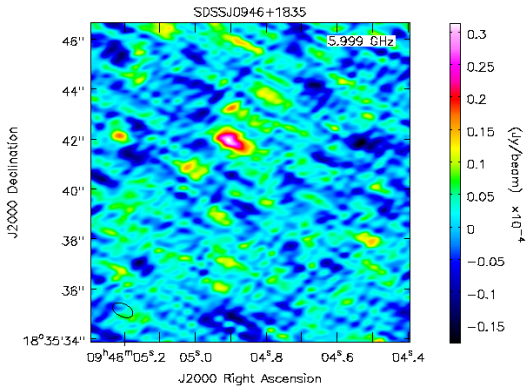
SDSSJ0946+1835
5.999 GHz
J2000 Declination
J2000 Right Ascension
(Jy/beam) ×10⁻⁴

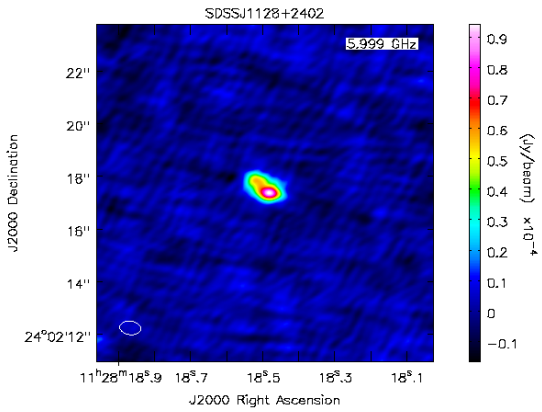
SDSSJ1128+2402
5.999 GHz
J2000 Declination
J2000 Right Ascension
(Jy/beam) ×10⁻⁴

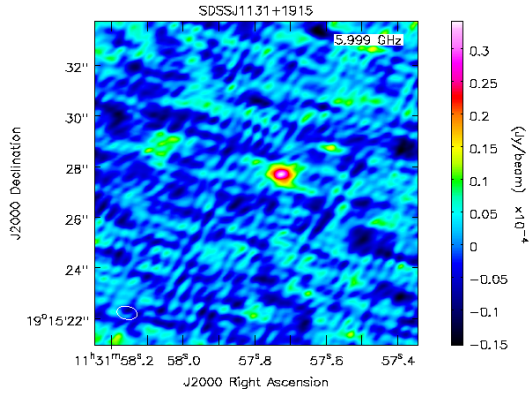
SDSSJ1131+1915
5.999 GHz
J2000 Declination
J2000 Right Ascension
(Jy/beam) ×10⁻⁴

Figure 7.3: The, 6GHz, radio contours plotted with Python package aplpy at 10, 20, 30, 40, 50, 60, 80, 100, 120, 140, and 160 μJy overlaying Pan-STARRS r band optical images with image size 128x128 pixels and cell size 0.1 arcseconds. SDSSJ0945+1835, SDSSJ0256+0153, and J0203+1612 use the i band Pan-STARRS optical image because the optical image corresponding to image A was not visible in r band.

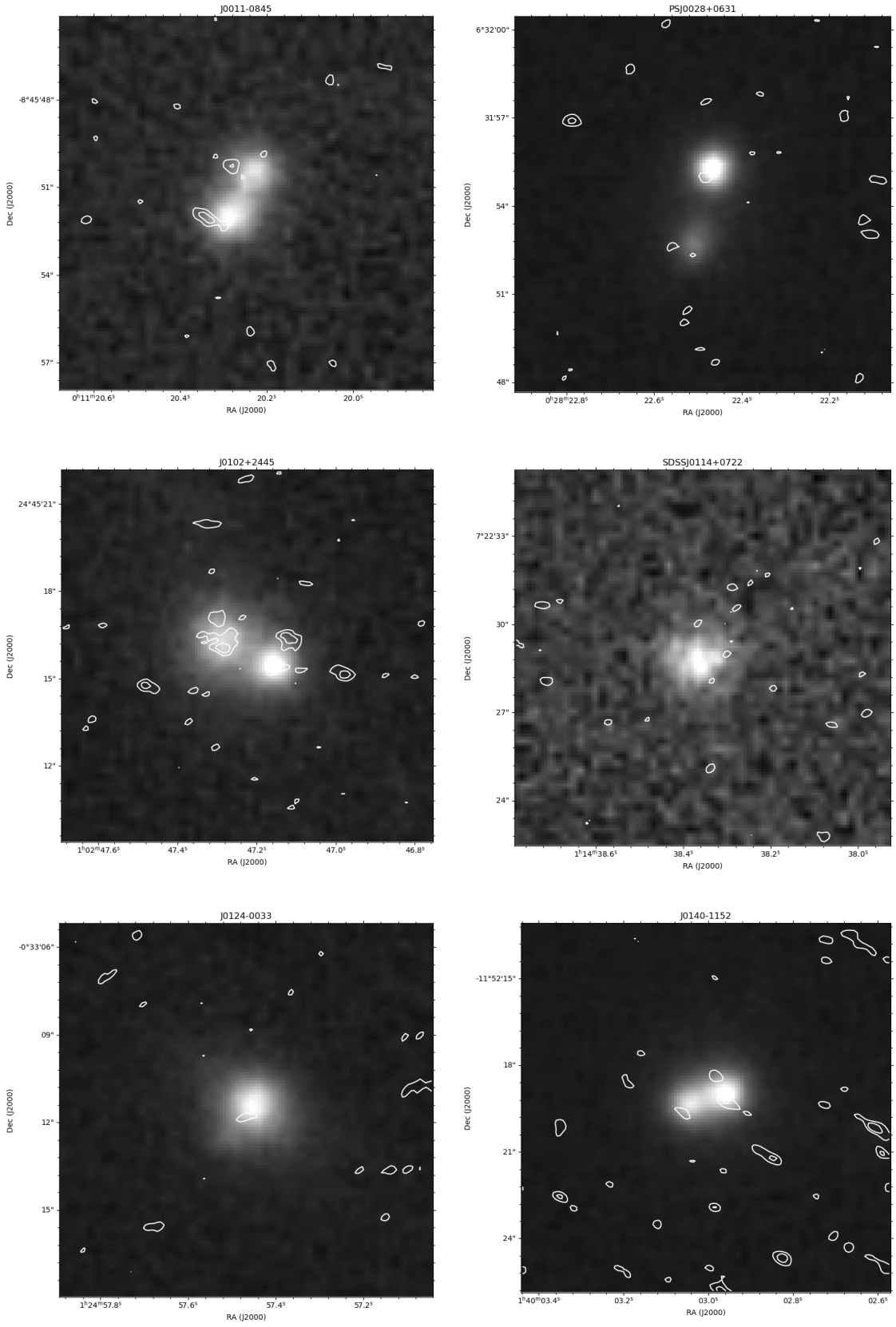

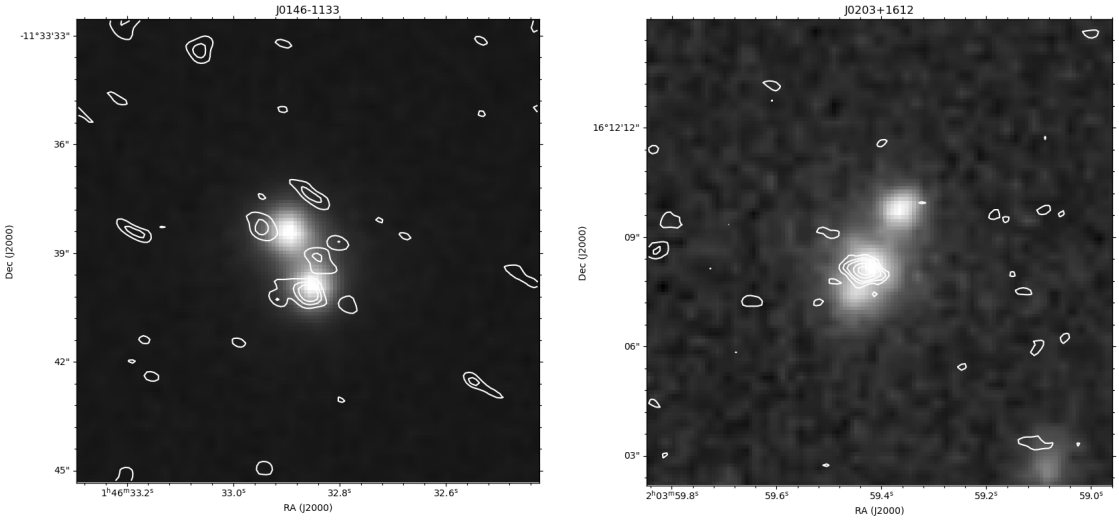
J0146-1133
-11°33'33"
36"
39"
42"
45"
Dec (J2000)
1h46m33.2s
33.0s
32.8s
32.6s
RA (J2000)

J0203+1612
16°12'12"
09"
06"
03"
Dec (J2000)
2h03m59.8s
59.6s
59.4s
59.2s
59.0s
RA (J2000)

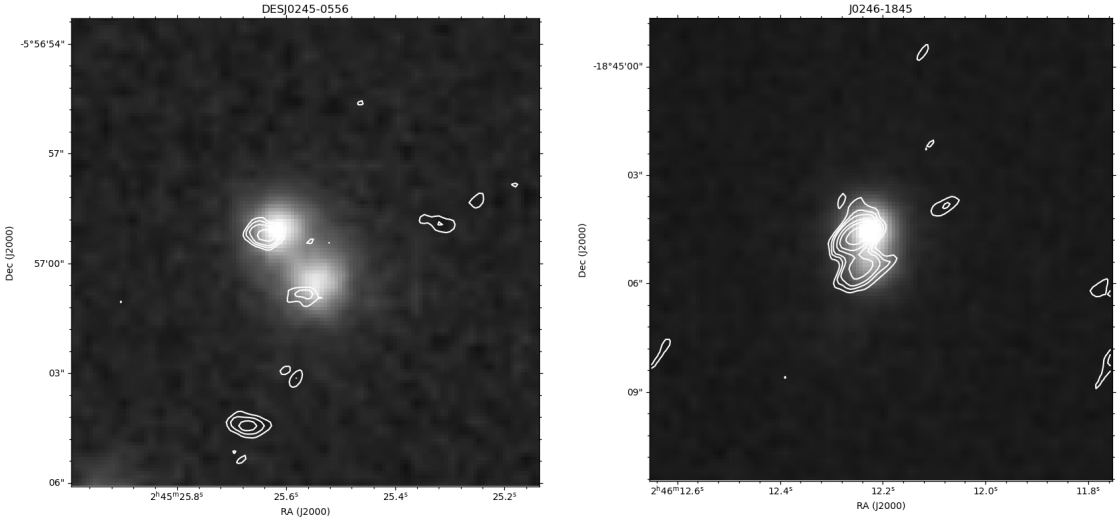
DESJ0245-0556
-5°56'54"
57"
57'00"
03"
06"
Dec (J2000)
2h45m25.8s
25.6s
25.4s
25.2s
RA (J2000)

J0246-1845
-18°45'00"
03"
06"
09"
Dec (J2000)
2h46m12.6s
12.4s
12.2s
12.0s
11.8s
RA (J2000)

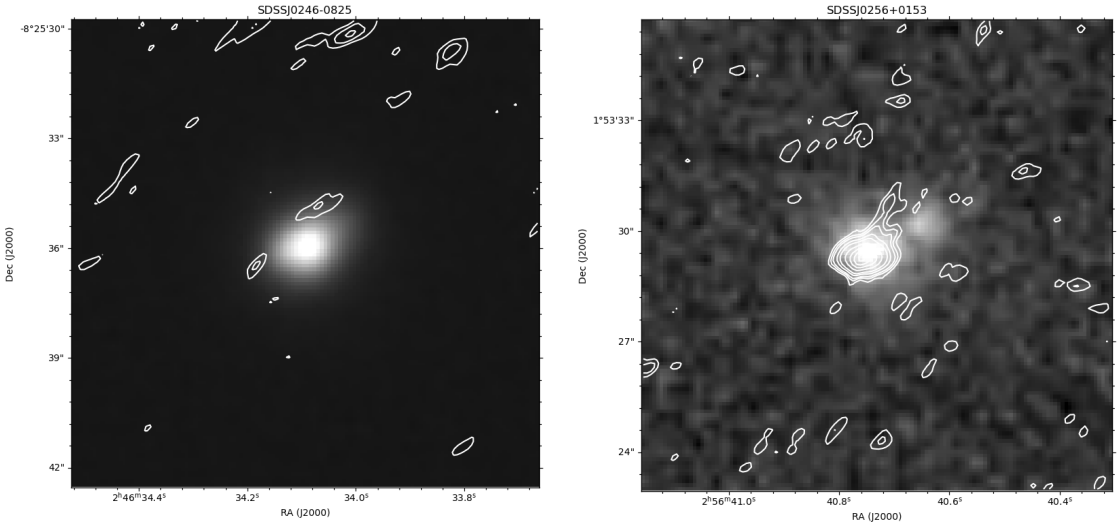
SDSSJ0246-0825
-8°25'30"
33"
36"
39"
42"
Dec (J2000)
2h46m34.4s
34.2s
34.0s
33.8s
RA (J2000)

SDSSJ0256+0153
1°53'33"
30"
27"
24"
Dec (J2000)
2h56m41.0s
40.8s
40.6s
40.4s
RA (J2000)

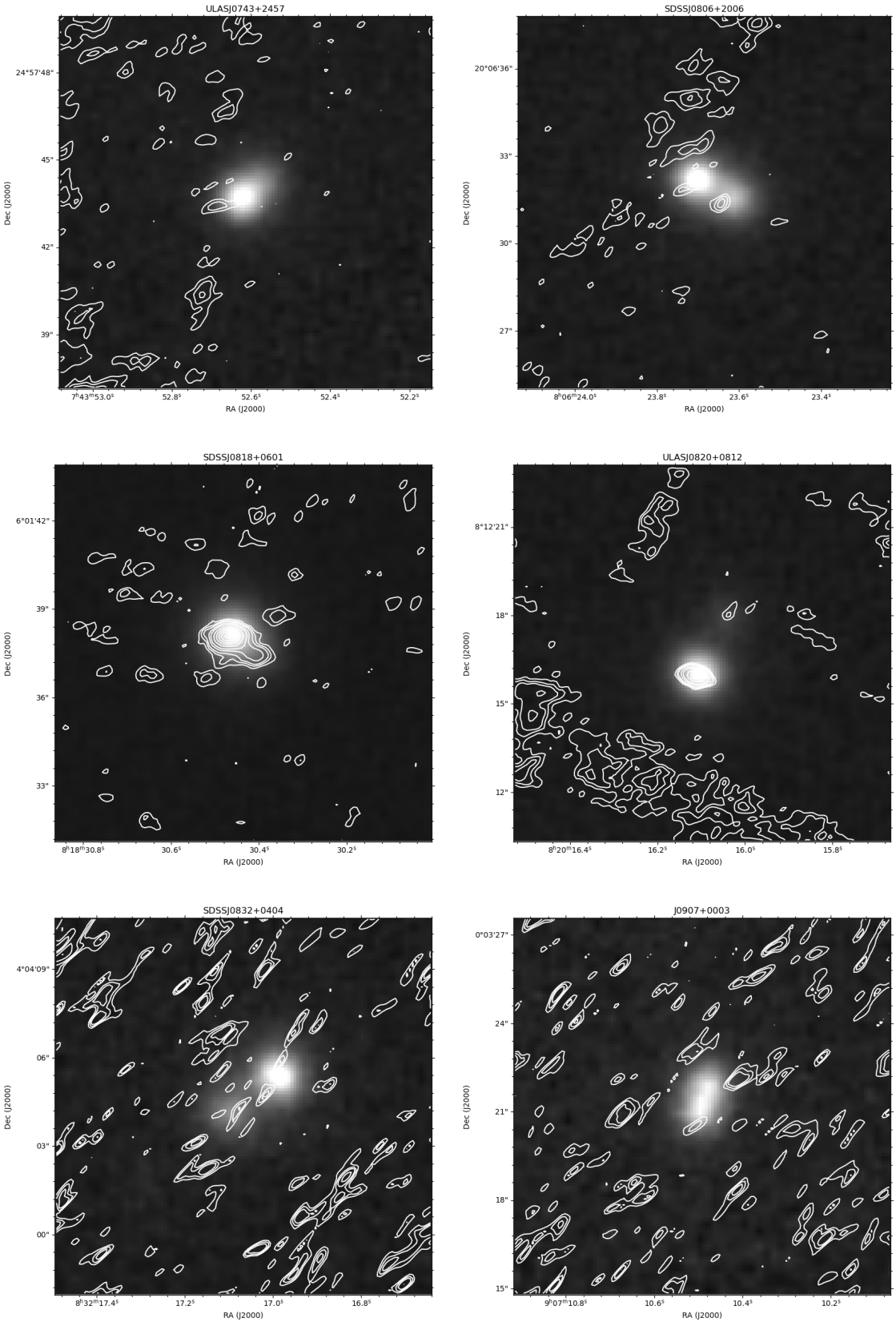
ULASJ0743+2457
24°57'48"
45"
42"
39"
Dec (J2000)
7h43m53.0s
52.8s
52.6s
52.4s
52.2s
RA (J2000)
SDSSJ0806+2006
20°06'36"
33"
30"
27"
Dec (J2000)
8h06m24.0s
23.8s
23.6s
23.4s
RA (J2000)
SDSSJ0818+0601
6°01'42"
39"
36"
33"
Dec (J2000)
8h18m30.8s
30.6s
30.4s
30.2s
RA (J2000)
ULASJ0820+0812
8°12'21"
18"
15"
12"
Dec (J2000)
8h20m16.4s
16.2s
16.0s
15.8s
RA (J2000)
SDSSJ0832+0404
4°04'09"
06"
03"
00"
Dec (J2000)
8h32m17.4s
17.2s
17.0s
16.8s
RA (J2000)
J0907+0003
0°03'27"
24"
21"
18"
15"
Dec (J2000)
9h07m10.8s
10.6s
10.4s
10.2s
RA (J2000)

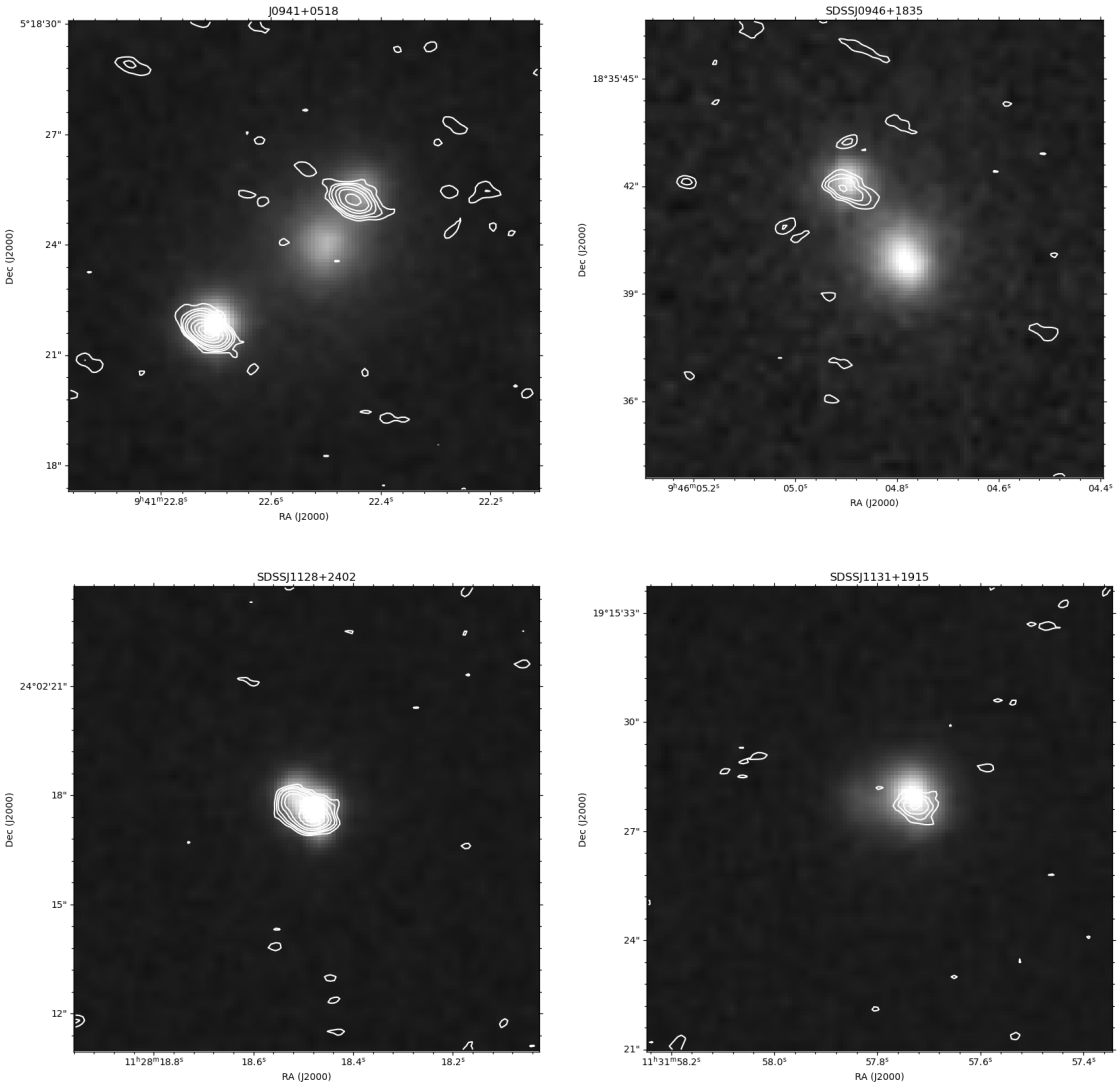
J0941+0518
5°18'30"
27"
24"
21"
18"
Dec (J2000)
9h41m22.8s
22.6s
22.4s
22.2s
RA (J2000)
SDSSJ0946+1835
18°35'45"
42"
39"
36"
Dec (J2000)
9h46m05.2s
05.0s
04.8s
04.6s
04.4s
RA (J2000)
SDSSJ1128+2402
24°02'21"
18"
15"
12"
Dec (J2000)
11h28m18.8s
18.6s
18.4s
18.2s
RA (J2000)
SDSSJ1131+1915
19°15'33"
30"
27"
24"
21"
Dec (J2000)
11h31m58.2s
58.0s
57.8s
57.6s
57.4s
RA (J2000)